DTIC FILE COPY

Naval Research Laboratory
Washington, DC 20375-5000

AD-A220 768

Advanced Concepts Theory Annual Report 1989

Final Report

Radiation Hydrodynamics Branch
Plasma Physics Division

DTIC
ELECTE
APR 2 3 1990
S
D
D

March 29, 1990

04 20 231

REPORT DOCUMENTATION PAGE

Public reporting burden for this collection of information is estimated to average 1 hour per response, including the time for reviewing instructions, searching existing data sources, gathering and maintaining the data needed, and completing and reviewing the collection of information. Send comments regarding this burden estimate or any other aspect of this collection of information, including suggestions for reducing this burden, to Washington Headquarters Services, Directorate for Information Operations and Reports, 1215 Jefferson Davis Highway, Suite 1204, Arlington, VA 22202-4302, and to the Office of Management and Budget, Paperwork Reduction Project (0704-0188), Washington, DC 20503.

1. AGENCY USE ONLY (Leave blank)	2. REPORT DATE 1990 March 29	3. REPORT TYPE AND DATES COVERED Final

4. TITLE AND SUBTITLE

Advanced Concepts Theory Annual Report 1989

5. FUNDING NUMBERS

6. AUTHOR(S)

Radiation Hydrodynamics Branch
Plasma Physics Division

PE - 62715H
WU - DNA880-191

7. PERFORMING ORGANIZATION NAME(S) AND ADDRESS(ES)

Naval Research Laboratory
Washington, DC 20375-5000

8. PERFORMING ORGANIZATION REPORT NUMBER

NRL Memorandum
Report 6612

9. SPONSORING/MONITORING AGENCY NAME(S) AND ADDRESS(ES)

Defense Nuclear Agency
Alexandria, Virginia 22310

Defense Nuclear Agency
6801 Telegraph Road
Alexandria, Virginia 22310

10. SPONSORING/MONITORING AGENCY REPORT NUMBER

11. SUPPLEMENTARY NOTES

This research was sponsored by the Defense Nuclear Agency under Subtask RL RA/Advanced Technology Development, Work Unit Code and Title, 00079, Advanced Technology Development, MIPR No. 89-565.

12a. DISTRIBUTION/AVAILABILITY STATEMENT

Approved for public release; distribution unlimited.

12b. DISTRIBUTION CODE

13. ABSTRACT (Maximum 200 words)

This report details the work of the Radiation Hydrodynamics Branch conducted in FY 89 with respect to several critical problems concerning the design of z-pinch implosions and the optimization of their radiative output. Separate sections describe progress in the analysis of z-pinch experiments, the development of atomic, electron, plasma and MHD dynamical models to describe z-pinch implosions, and the analysis of atomic number scaling of z-pinch K-shell emission.

14. SUBJECT TERMS

Z-pinch physics
Radiation MHD
Atomic data scaling
Non-LTE dynamics

15. NUMBER OF PAGES 174

16. PRICE CODE

17. SECURITY CLASSIFICATION OF REPORT	18. SECURITY CLASSIFICATION OF THIS PAGE	19. SECURITY CLASSIFICATION OF ABSTRACT	20. LIMITATION OF ABSTRACT
UNCLASSIFIED	UNCLASSIFIED	UNCLASSIFIED	UL

NSN 7540-01-280-5500

CONTENTS

Accesion For		
NTIS CRA&I		☒
DTIC TAB		☐
U announced		☐
Justification		
By		
Distribution /		
Availability Codes		
Dist	Avail and / or Special	
A-1		

EXECUTIVE PROGRAM SUMMARY

A major accomplishment of this year's NRL Plasma Radiation Source (PRS) Theory Program was a demonstration of how long-term theoretical support allows sparse and diverse experimental results to be organized, interpreted, and understood. As a result, guidance that will lead to improved simulation fidelity was given this year for the design of pulsed power machines as plasma radiation sources (PRS). To accomplish this, a large series of pre-planned wire array aluminum hydrodynamics calculations were carried out and the results were extensively analyzed. This analysis provided a set of minimum requirements for pulse power machine design. It predicted aluminum K-shell yield behavior as a function of array mass and current, led to predictions of how a given K-shell yield scales with atomic number, and stimulated a new series of PRS experiments that were designed and carried out at Physics International Inc. using aluminum wire arrays. These experiments will be analyzed in the coming year. Preliminary analysis indicates that the calculations had indeed predicted minimum aluminum K-shell yields, and it led to the observation that at least one other important x-ray energy conversion mechanism is at work in the PRS plasma. One such mechanism has received some preliminary phenomenological attention and will be described later in this final report. A data base needed to analyze PRS aluminum plasmas for their temperature, density, and K-shell mass participation was also completed. It will allow a two pronged analysis of the PI PRS data to be carried out and quantities such as anomalous resistivity and other anomalous plasma properties to be unambiguously inferred from the data.

Other important NRL theoretical efforts continued this year. They fall into five program categories:

I.   Program Technical Guidance and Data Analysis

o Detailed K-shell emission atomic number scaling laws were developed for kinetic energy to x-ray conversion and are being evaluated using nickel array implosion calculations.

o Maxwell Laboratory aluminum array implosion data were analyzed and trends in plasma temperature, density, and mass participation were determined.

o The approach to equilibrium in a reflex switch was analyzed. The predicted and the observed voltage and current waveforms were found to be in good agreement so there is hope that some basis for understanding reflex switch operation has been established.

II. Atomic Data Acquisition

o A complete set of atomic data was calculated for F to Ne dielectronic recombinations in four different elements. This data was found to be scalable. Consequently it will be used to produce reliable DR data for Ar through Kr ions, and it will lead to reliable satellite line spectral diagnostics.

o A complete collision strength data base for calculating Fe and Se L-shell collisional excitations was calculated. Preliminary analysis suggests that this data should be scalable. This means we will get 20 data sets for the price of 3.

o Procedures for calculating and scaling radiative decay rates in the L-shell were also developed.

III. Radiative Collapse

o Conventional MHD descriptions of an imploding aluminum (or low Z) array using present-day pulse power voltage waveforms generally lead to a radiative collapse in contradistinction to the experimental situation. A careful, phenomenological analysis of PI aluminum experiments was carried out to demonstrate that a short circuit in the diode and anomalous resistivity in the plasma will move the calculated x-ray emission in the direction of experiment and eventually produce fair agreement.

IV. PRS Optimization

o The problem of determining machine coupling efficiency to future PRS loads was addressed in three separate ways:

o The way a diode short circuit affects machine coupling in an argon puff gas implosion is currently being investigated.

o The bleeding of current away from the main body of plasma by a plasma corona was investigated, and the theory of this corona was critiqued. In general, we need to evaluate the degree of machine PRS decoupling produced by runaway electrons, and the existence of a corona may be a relevant aspect of this problem, since, it was determined this year that, our present-day MHD is not in accord with existing experimental data on runaway electron production.

o The coupling efficiency of a transmission line to screwpinch and z-pinch PRS loads was calculated and found to be acceptably large.

V. New PRS Approaches

o By imploding onto and compressing a magnetic field in a screwpinch array implosion, one can, in principle, control implosion stability in the laboratory. An ideal MHD screwpinch model was developed this year and benchmarked successfully against self-similar analytical MHD flows. Once magnetized transport and magnetic field diffusion are added to the model, it will be used to carry out detailed calculations of the stability of presently achievable magnetic shear profiles.

o Ring plasma stagnation dynamics between an argon plasma and an iron wall were calculated. They confirmed that the stagnation of a high velocity ring-puff plasma on a planar solid density target will generate a high density plasma that can efficiently emit multi-keV radiation.

o A 2-d MHD model of a copper x-pinch was developed to investigate the dynamical evolution of the pinch and to predict the variation in radiated energy as a function of the mass per unit length. This pinch is of special interest because it produces a point source of x-rays.

A more detailed description of the above work can be found in Sections I through V of this report, which correspond directly with the 5 program categories listed above. Further details have already been given in a number of papers that were written this year for publication.

As a result of the work that was, and is being, carried out in the NRL Theory Program this year, a number of challenging new ideas have emerged for (1) making machine upgrades to increase K-shell output on existing PRS pulse-power machines, (2) carrying out new experiments with more efficient load designs, (3) improving our understanding of present-day machines, and (4) exploring the possibility of achieving radiative collapses. For example, it is anticipated that a proper upgrade of the Phoenix PRS machine at NSWC should produce kilojoules of nickel K-shell radiation. Other new developments in the status of the PRS program can be summarized as follows:

o We now have the capability to learn a great deal about PRS loads using time resolved experimental diagnostics. We also have the tools to analyze these experiments and clearly delineate anomalous heating and mass participation effects. These diagnostics and tools need to be exercised.

o A systematic new theoretical interpretation can now be given to a wide range of experimental results on array implosions. However, a large data base of such results needs to be obtained to learn more of the phenomenology of anomalous heating. This development is of special significance since, in the past, PRS experiments conducted on a given machine by varying load parameters and materials have been notoriously difficult to interpret and misleading when it comes to optimizing PRS design.

o Because it is important to build a data base of experimental results from as many different PRS machines as is possible, it is important that the decade machine be designed to have a PRS research capability, preferably with options for variable diode and current design (and not just variable load options).

o We now have a credible and growing theoretical capability to predict mass and current scalings for imploding different atomic number PRS array designs. However, it must be tested, benchmarked, and improved both experimentally and theoretically. A PRS capability on the decade machine would aid and abet this process.

o Most importantly, the scaling work that was done this year has made it clear that pulse power machines and/or their diodes must be designed for the specific yield and spectrum (or element) requirements desired. If done, the AGT simulation fidelity goals of DNA can be met rather than approximated.

o Finally, a sound and viable theoretical foundation has been built to treat problems in radiative hydrodynamics and plasma radiation source development. It needs continued long term support to be brought to full fruition in order to (1) help set the parameters for new machine design, (2) aid in the development of new PRS concepts, (3) provide the tools necessary to carry out data analysis and interpretation and (4) promote the design and evaluation of new experiments and new improved loads.

ADVANCED CONCEPTS THEORY ANNUAL REPORT 1990

I. Program Technical Guidance and Data Analysis

The analysis of the scaling of K-shell emission in aluminum with mass and kinetic-energy-per-ion was completed. In this work we investigated a special physical situation in which the conversion of implosion kinetic energy into K-shell emission at stagnation could be studied unambiguously. Some of this work was communicated to the z-pinch community at the Laguna meeting (April 26, 2989) and at the Colorado Springs Simulation Fidelity Workshop (September 19 - 23, 1989). A much more detailed description of this work was given in two papers that were submitted for publication in JAP and JQSRT.

In the JQSRT paper, the mechanism by which the imploded plasma makes the transition from I^4 to I^2 yield scaling is described. The JAP paper provides a complete description of how K-shell emission in aluminum scales with mass and kinetic-energy-per-ion, and it also makes predictions as to how these results should scale with atomic number. We found that under optimum conditions about 30% or more of the total kinetic energy stored in the aluminum plasma can be emitted as K-shell radiation. The atomic number, Z, scaling was done by assuming that this conversion efficiency is constant for all Z materials. However, if this efficiency is substantially less for higher Z materials, then our scaled results are overly optimistic. We have initiated studies using nickel in order to determine more accurately how the conversion efficiency scales with Z.

Chris Deeney at PI took the initiative to set up experiments with imploding aluminum wire arrays to put the above aluminum calculations to experimental test. This provided us with an excellent opportunity to not only work and exchange ideas with the people at PI but also to extend the aluminum scaling predictions, in which the current was turned off just prior to implosion, to the experimental measurements of K-shell emission, where the current persists throughout the implosion. Since the purpose of the experiments was to compare experiment and theory, maximum machine energy coupling had to be insured by having the implosion times occur near the peak

in the open circuit current profile of Double Eagle. According to 0 and 1-D theory, the implosion time can be held fixed if m and r_o are chosen such that $(mr_o^2) \propto \tau^2$, where τ is a fixed implosion time. Then by varying m and r_o along the path defined by mr_o^2 = constant x τ_p^2, where τ_p is the implosion time that corresponds to the peak in the short circuit current profile, one can determine how the K-shell emission varies with mass and radius.

Because these experiments were conducted on a machine with a given current risetime and peak current, they could not be conducted to check against the calculations directly, since the calculations were carried out holding either the load mass fixed or the kinetic-energy-per-ion fixed. However, using the current peak and risetime of the experiment and the condition mr_o^2 = constant, one could theoretically determine the mass, kinetic-energy-per-ion, current, and implosion time variations that should have occurred in the experiments. Then, using the analytic fits to the MHD calculations that were obtained in the analysis, one could determine the K-shell yield that should have occurred if only implosion kinetic energy were being converted to K-shell emission. The comparisons between the theoretically calculated mass, implosion time, current at the time of peak kinetic energy generation, kinetic-energy-per-ion, and K-shell yield and their experimentally determined values are shown in Figures 1-5. In the experiment, values of m were chosen according to the relation $m \sim 1/r_o^2$ as shown in Fig. 1. Note, there is a slight deviation from the mr_o^2 = constant curve for the 80 µg/cm load. The collapse time and peak current, which should have remained roughly constant as r_o and m were varied, had, in fact, the experimental variations displayed in Figs. 2 and 3, respectively. Because the substantial deviations in the peak current shown in Fig. 3 could represent a factor of two differential in energy coupling to the load, these deviations need to be taken into consideration when analyzing the data. Fig. 4 is a plot of η versus $2r_o$, where η is defined as the kinetic-energy-per-ion divided by the minimum kinetic energy-per-ion needed to excite an ion into the K-shell. The minimum kinetic-energy-per-ion is theoretically predicted to be about 12 keV for an aluminum plasma. If this is a true prediction, then one would expect a precipitous drop in K-shell emission as η goes below unity. Indeed, this is

what occurred in the experiment as reflected in Fig. 5, where the K-shell yields as a function of array diameters are graphed. There is a large decrease in K-shell emission which occurs between the 12.5 mm array, which has an η value of 1.3, and the 9 mm array, which has a value of η below unity. The experiments also show a qualitative change in the K-shell emission region when η becomes < 1.

When the masses imploded in these experiments are large enough, the theory predicts that the K-shell yield should be in an I^2 scaling regime and consequently the yield should be approximately 30% - 36% of the total kinetic energy. Therefore any large variation in the theoretical yield predictions would be related to variations in how much kinetic energy was generated. The calculation of kinetic energy is based on estimates of the changes in diode inductance occurring in the experiments and should be roughly constant for different r_o in accordance with the predictions made in Fig. 5. This is interesting, because the experiments show that the maximum experimental K-shell yield, which occurs for η near but > 1, is a factor of 3 larger than predicted by kinetic energy conversion theory, i.e. it is as if all of the imploded kinetic energy had been converted into K-shell emission (which is not possible). Consequently, one can infer from the data that there is more energy being converted to x-rays than was originally thought to occur by kinetic energy conversion alone. This is plausible since the current remains on in the experiment after the implosion has occurred[1,2]. Energy is also likely to be trapped in the diode by an electrical short that develops as the plasma inductance rapidly increases as the plasma nears peak implosion[3]. This trapped magnetic field energy is transferred to the plasma either ohmically or inductively and it ultimately escapes the plasma as radiation. The time over which emission occurs should be indicative of the decay time of the energy trapped in the magnetic field. Because no further collapse of the plasma appears to be observed experimentally, one expects that an anomalous ohmic heating is occurring and that this heating is largest for η near 1. More work is being done to analyze these experiments. Note, though, that the aluminum calculations did correctly predict minimum x-ray output from the pinch. This is an extremely encouraging result.

We have been motivated by these comparisons between experiment and theory to investigate a number of questions and speculations regarding their interpretation. One such speculation is that it may be best in general (and not just in the case of these particular aluminum experiments) to implode the maximum amount of mass that one can while still allowing η to be in excess of unity. There are three reasons for this speculation. First, of course, this is what the comparison of K-shell yield versus $2r_o$ shows in Fig. 5. Secondly, the theory predicts that maximizing mass while keeping η greater than 1 will virtually guarantee that maximum conversion efficiency of machine energy to K-shell emission is achieved. The third reason is related to the fact that there appears to be experimental evidence to support the conclusion that the experiments never achieve as large a density as predicted by theory. Since a large density as well as a long pulse duration are key ingredients in determining when a plasma is in the maximum efficiency (I^2) theoretical K-shell emission scaling regime, it makes plausible sense that if the experiments that achieve the largest density have the more massive loads, that they are thus more likely to produce maximum emission. This is at present only a reasonable speculation. However, we are presently in the process of doing a comparison between experimental and theoretical temperatures and densities in order to quantify any differences between theory and experiment and to verify the applicability of the above speculation to these particular experiments.

We have also begun investigating the implosion dynamics of nickel wire arrays using the same simplifying assumptions as were used in the aluminum calculations. During the runin phase of the dynamics, we assumed that the current was linearly rising. In this case the final kinetic-energy-per-ion that is generated prior to assembly on axis depends only on the implosion time of the array. Secondly, we assumed that the current was shut off just before the plasma collided with itself on axis. Then, the dynamics of implosion and collision could be calculated using a 1-dimensional magneto-hydrodynamics (MHD) code that contains three essential attributes: (1) it contains a structurally complete, state-of-the-art atomic model of nickel, (or aluminum for the work described above), (2) it contains an extensive nonlinear, nonlocal description of line photo-couplings within the plasma. (Because of the inelastic nature of the z-pinch collision process, to be seen shortly,

this attribute is of prime importance), and (3) it consists of a fully consistent coupling of the atomic ionization model and radiation transport to the array implosion MHD.

From an analysis of a slug model description of the implosion dynamics, one finds that two energies play vital roles in determining the radiation characteristics of the imploded array. The maximum kinetic-energy-per-ion, which is drawn in Figure 6 for the radiating cases shown in Figures 7 and 9, controls the temperature that is reached by the plasma. In order to achieve greater simulation fidelity with plasma radiation sources (PRS) it is necessary to radiate from the K-shell of moderate-Z elements up to krypton. As seen in Figure 6, to radiate in the K-shell of aluminum with energies around 1.8 keV requires a kinetic-energy-per-ion, in the case under study, of ~ 50 keV/ion (4 times the minimum); whereas, to radiate in the K-shell of nickel around 8 keV and beyond requires that the nickel ions reach corresponding energies of 700 keV/ion. If these ion energies are reached, the amount of radiation actually emitted from the K-shell depends on the amount of kinetic-energy-per-centimeter generated in the implosion, i.e. on the mass imploded. For aluminum imploded to a kinetic-energy-per-ion of ~ 50 keV/ion, the yield of K-shell x-rays increases at first as m^2 at low masses and then as m at high masses (greater than 24 µgm/cm as seen in Figure 7). This transition occurs as a result of the collision becoming more and more inelastic as the mass increases (see Figure 8). When this transition takes place, roughly 36% of the kinetic-energy-per-centimeter generated during the implosion can be converted to K-shell x-rays.

As seen in Figure 9, the results for aluminum can be scaled to nickel. For the first three cases shown in the table, the nickel reached a kinetic-energy-per-ion of ~ 700 keV/ion when imploded from 1 cm in 33 nsec. (If one wanted to lengthen this implosion time, one would have to start the array implosion from proportionately larger radii, hence the importance of studying screwpinch implosions.) As the mass is increased from 10 to 100 to 500 µgm/cm, the K-shell yield from nickel at first scales as m^2 and then begins to approach m-scaling. The peak currents needed to achieve these implosions scales as √m. Thus, 20 MA is needed to implode nickel from 1 cm in 33 ns to

5

achieve a yield of 58 kJ/cm. (A 2 cm length array would radiate 116 kJ.) As the last case in Figure 9 shows, the same 20 MA can, in principle, produce increased yields if the implosion time can be shortened.

It is worth contrasting the results of this paper with the results presented in another paper at the Simulation Fidelity Workshop. In C. Hartmann's paper on "The Compact Torus Accelerator, A New X-Ray Source for High Fidelity Simulator", we learned that if an energetic beam of ions, enclosed in some electrons, i.e. a plasma, is shot at a stationary copper wall it bounces from the wall and generates, in principle, upward of hundreds of kilojoules of 10 keV x-rays. In nickel z-pinch implosions we showed that, if a plasma is collided and compressed against itself (compare ring accelerator concepts), one can get, in principle, hundreds of kilojoules of 10 keV x-rays if one controls the amount of mass participating in the emission carefully. Both concepts require that the plasma be focusable. Both have their problems in this regard, and both have different options for flexibility. For this reason, both research approaches and options should be vigorously pursued. However, there is one important difference between the two approaches that should be noted. In z-pinches significantly more than kinetic energy conversion has been observed to occur in the experiments, as the current continues to cook the plasma. This important energy dividend is not available in the ring accelerator.

References

1. J. W. Thornhill, F. L. Young, K. G. Whitney, and J. Davis, "Theoretical and Experimental Comparisons of Gamble II Argon Gas Puff Experiments", presented at the DNA NVOO Meeting, April 5-6, 1988.

2. M. Krishnan, "PRS - A critical Assessment," Phys. Inter. Report 89-01.

3. C. Deeney private communication.
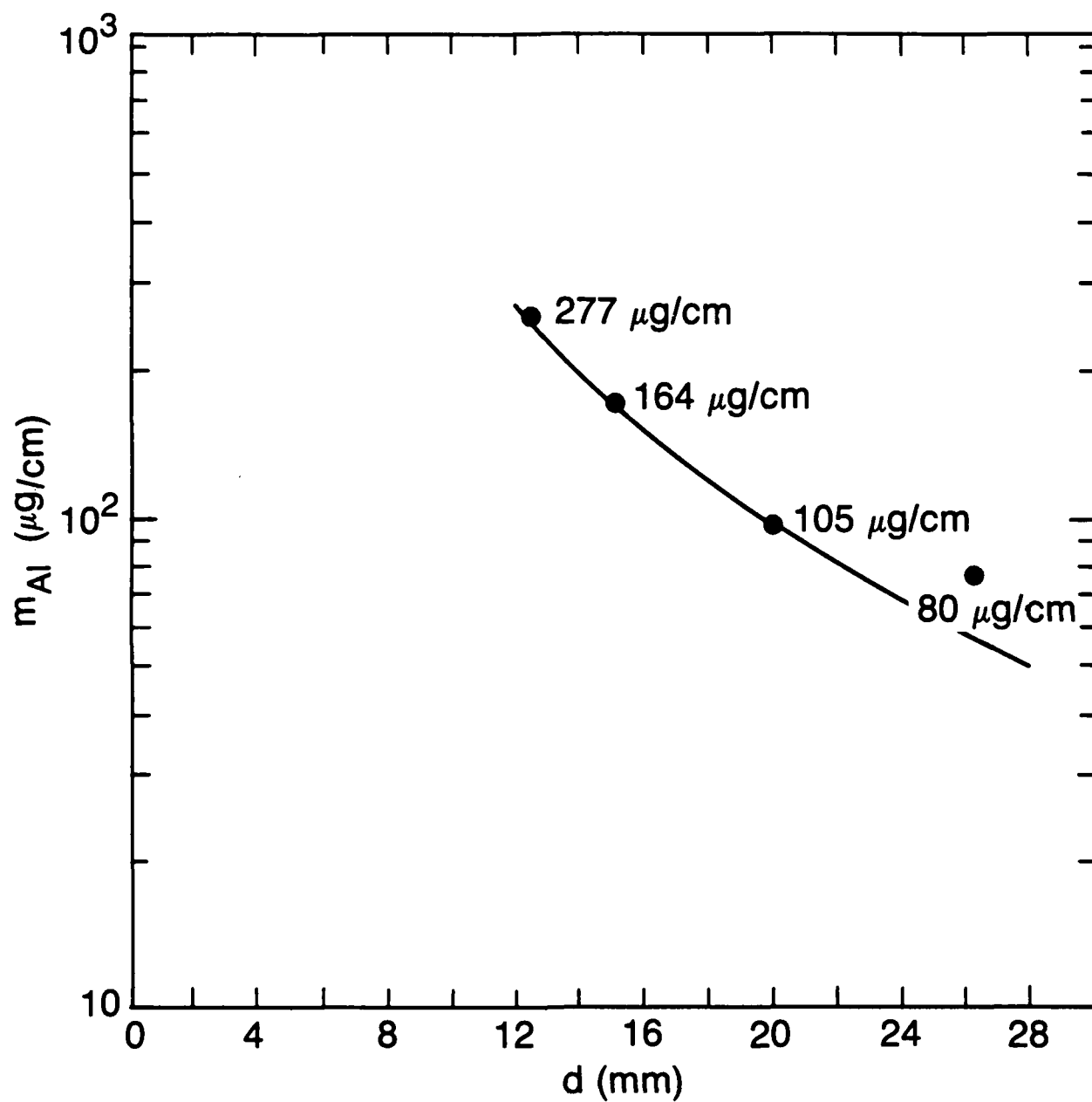
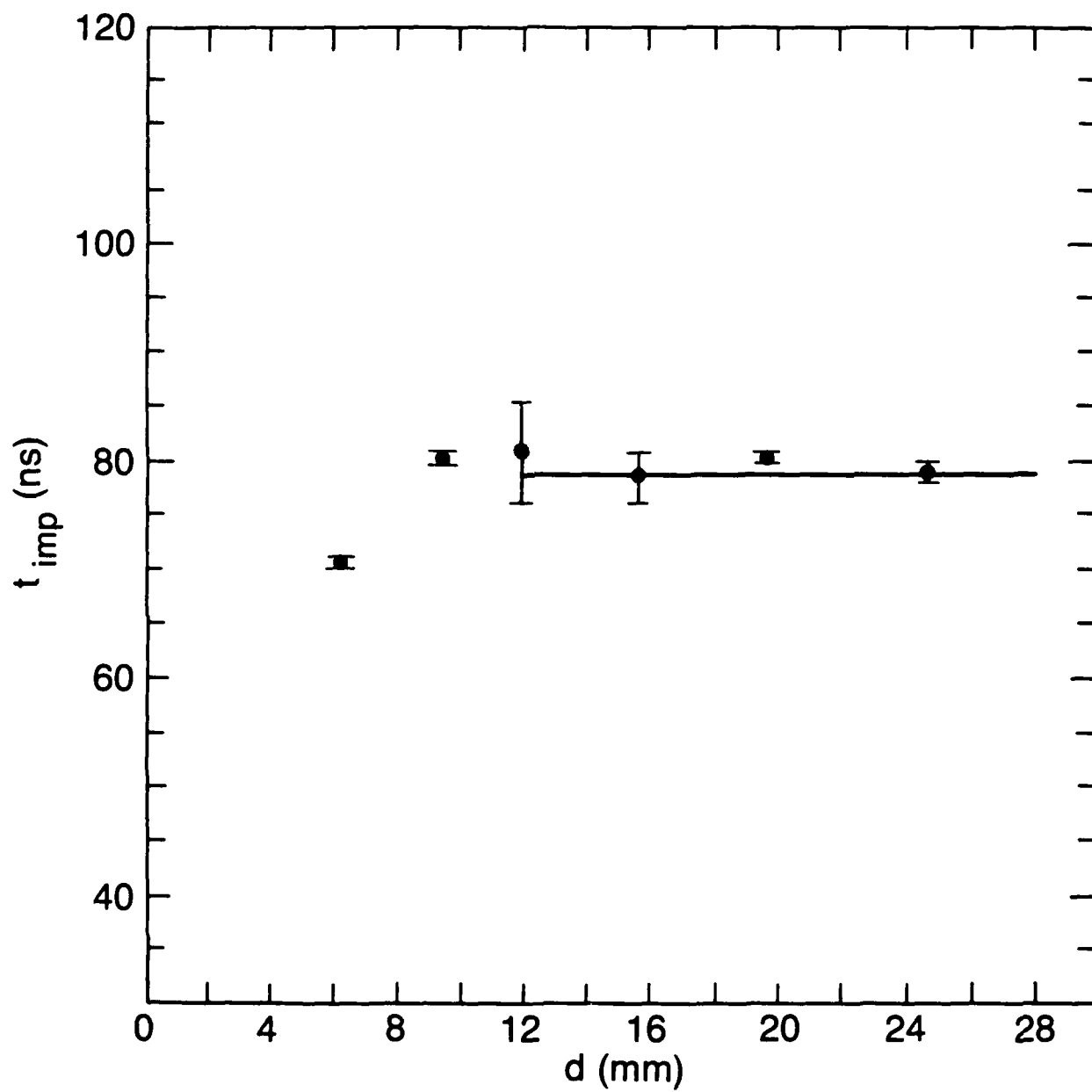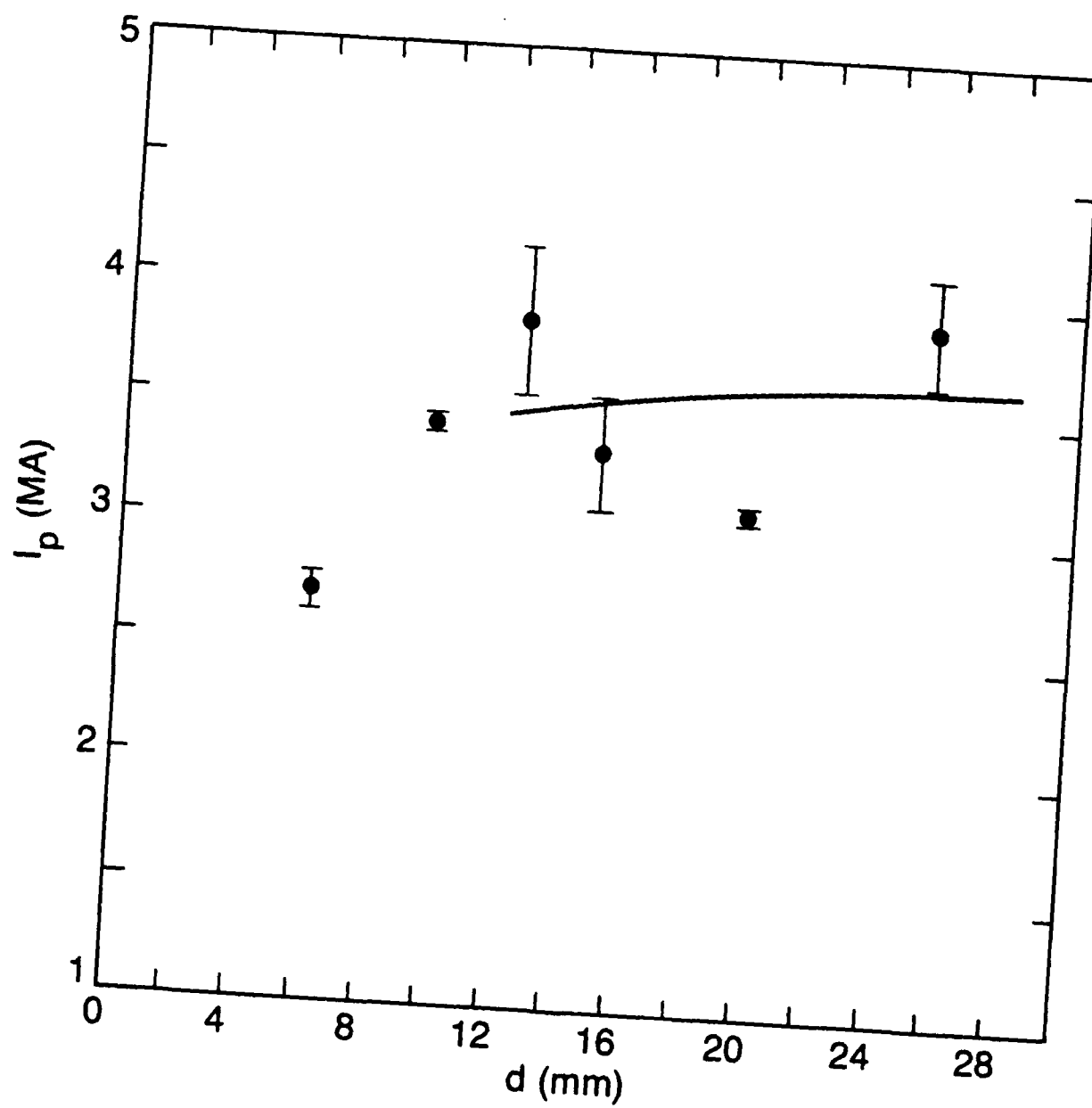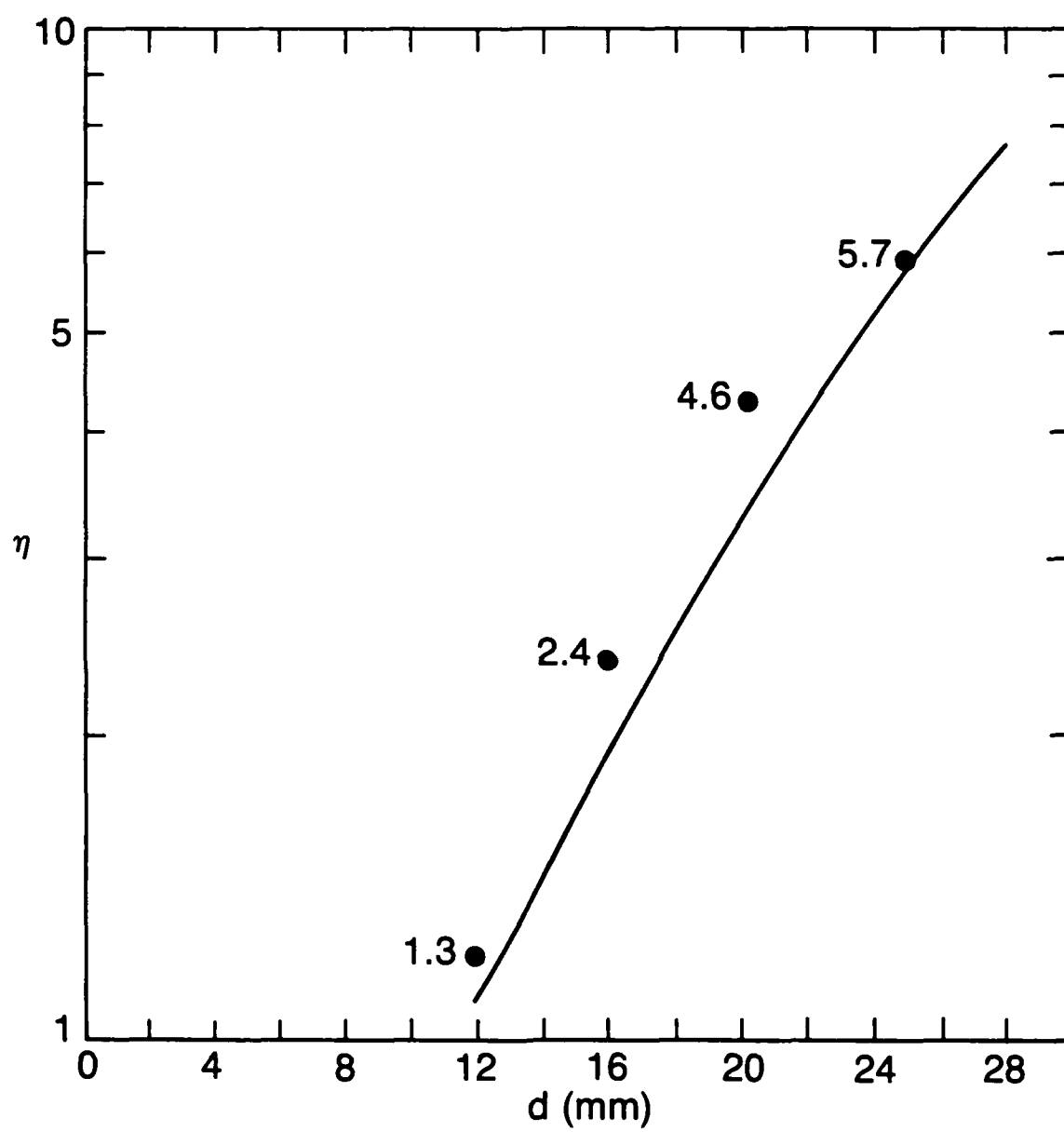NOTE: 25 mm ϕ array does not fall on md^2 = constant
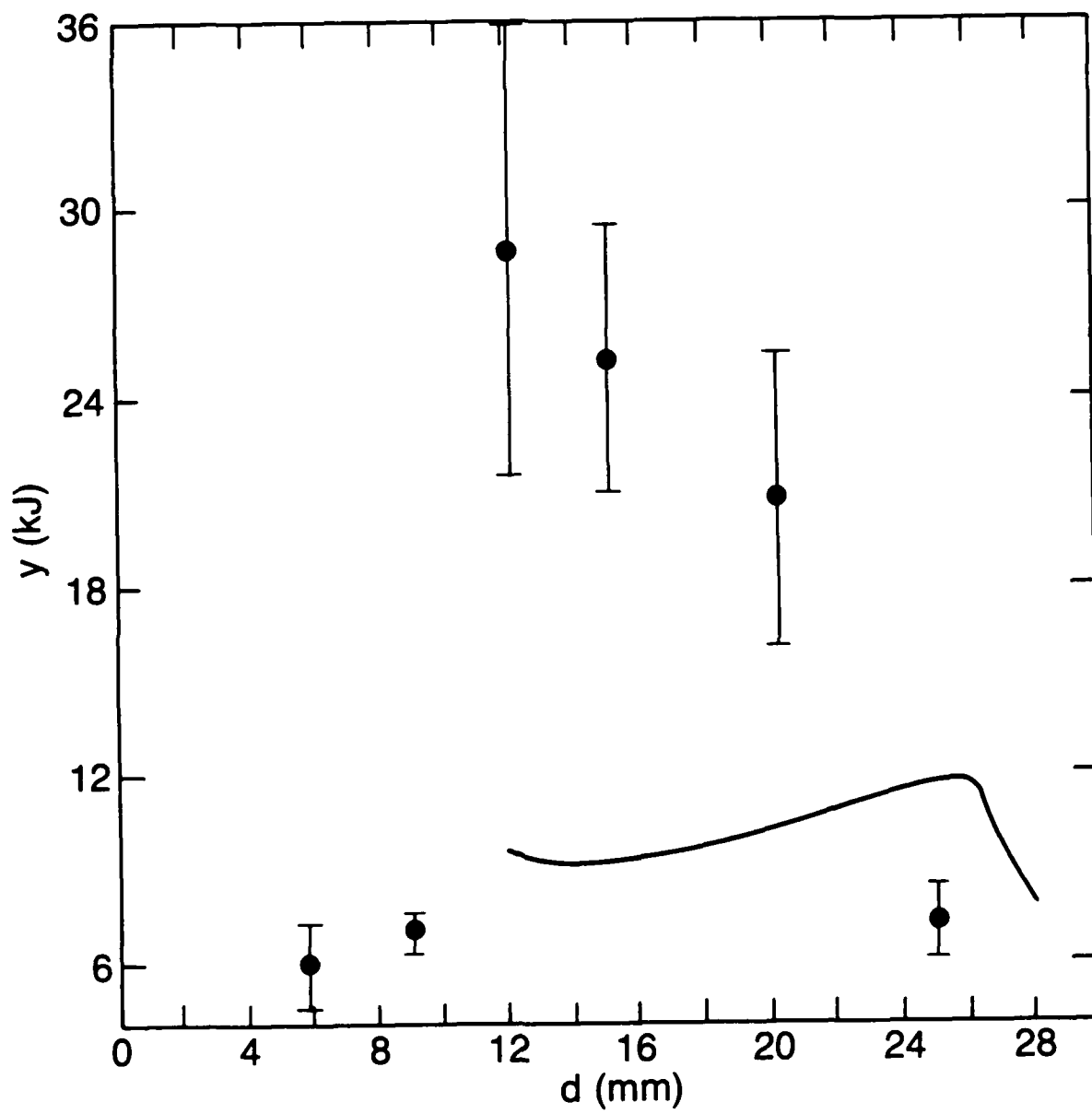
Figure 1
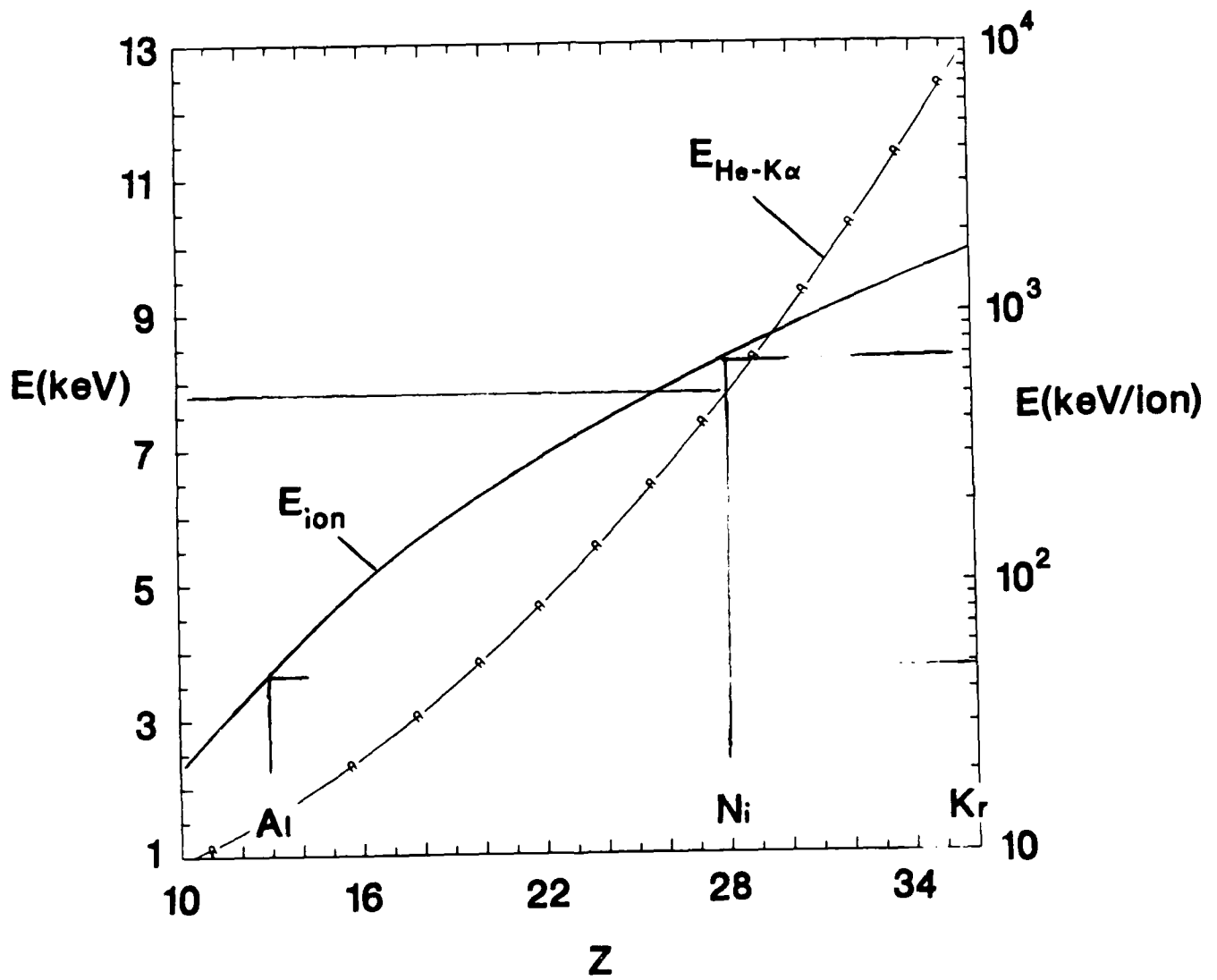
Figure 2

Figure 3

Figure 4

Figure 5

IMPLODING WIRE ARRAYS

Figure 6

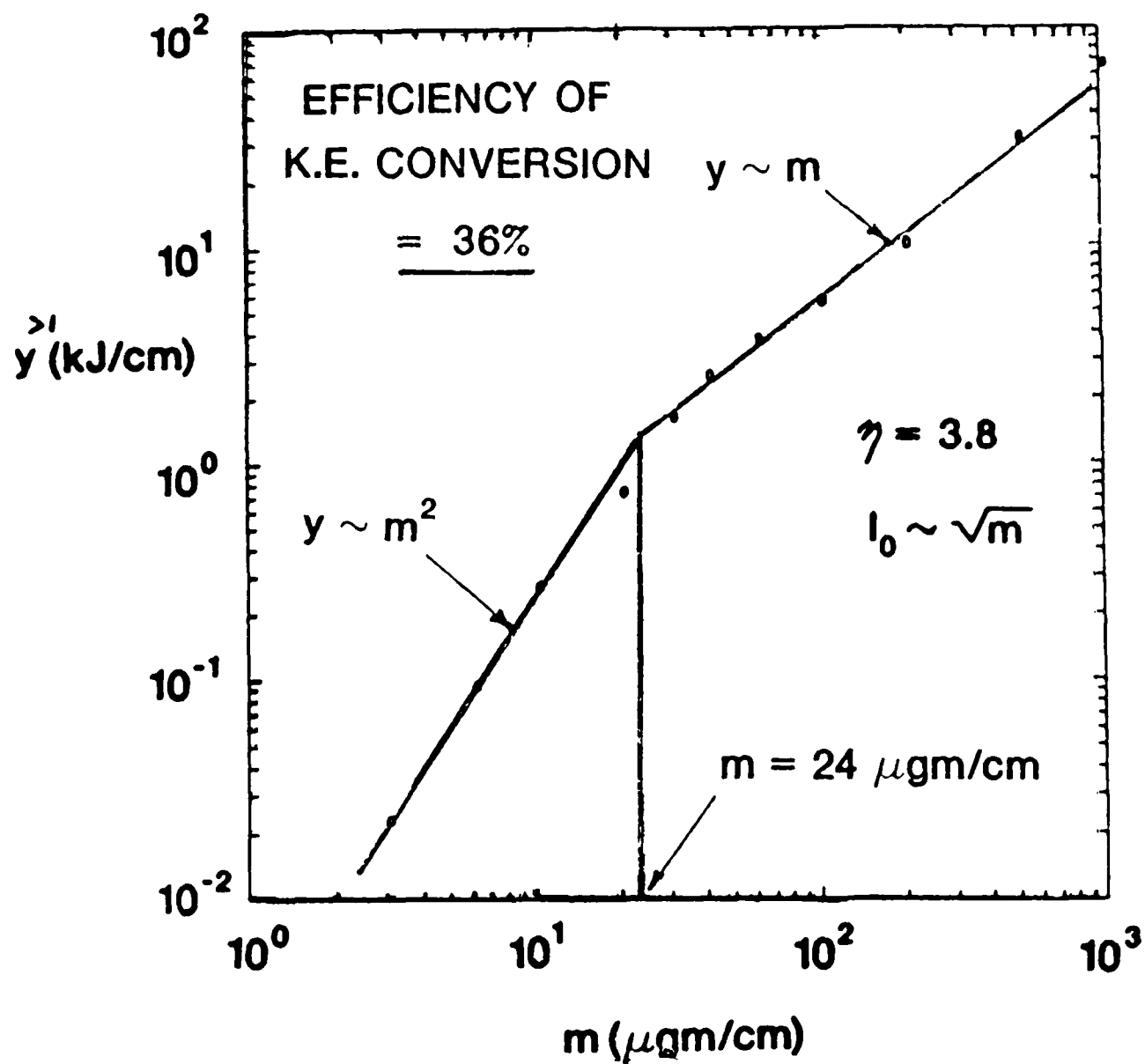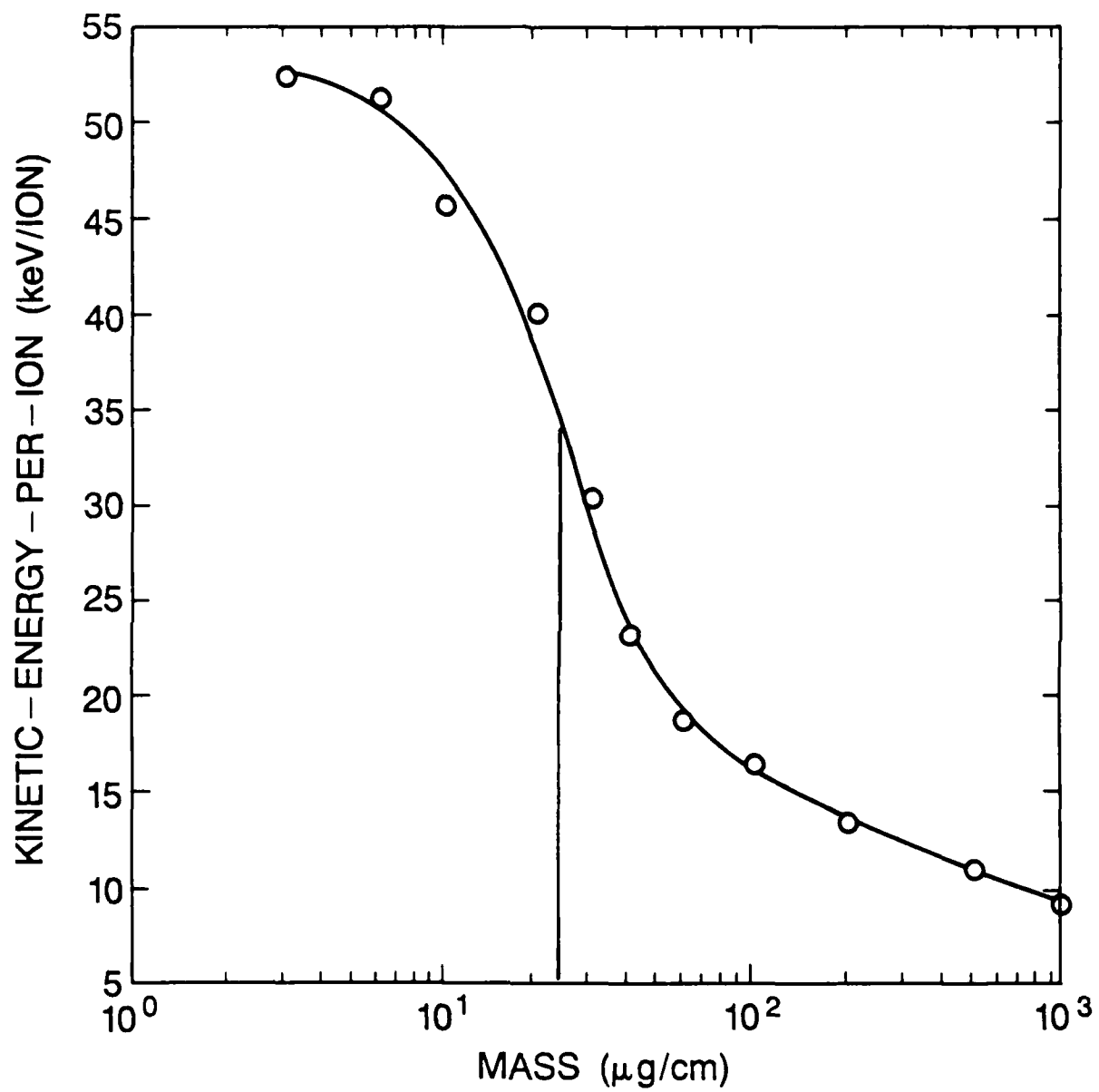Figure 7

Figure 8

14

NICKEL RESULTS

$m(\mu g/cm)$	$t_i(ns)$	$I_0(MA)$	$y_K(kJ/cm)$
10	33	2.7	0.08
100	33	8.6	8.3
500	33	19.3	56
50	21	9.8	2.7
200	21	19.5	83

$r_0 = 1$ cm

Figure 9

PRELIMINARY ANALYSIS OF ALUMINUM Z-PINCH - DATA TAKEN ON BLACKJACK 5

As described in the 1988 DNA Final Report [1] and in NRL Memo 6383 [2], one can use theoretically determined line ratios and yields to estimate the average ion density and electron temperature reached during peak compression in a particular experiment. In previous work, we looked at titanium wire experiments performed on Blackjack 5. We have now taken a preliminary look at several aluminum wire experiments recently done on Blackjack 5.

As with the theoretical titanium database used previously, the aluminum database is composed of a series of collisional radiative equilibrium (CRE) calculations done for a steady-state, homogeneous cylindrical plasma at different ion densities, electron temperatures and radii. From these CRE calculations we have derived the dependence of the radiated power per centimeter, the He-α to Ly-α line ratio, the He-β to Ly-α line ratio, and the He-β to Ly-β line ratio on the ion density and electron temperature. Given the size of the emitting region, these four values can then be compared to the experimentally determined average K-shell energy production rate and the relative line strengths.

2. Experimental Data

Seven of the filtered SXR series aluminum wire array shots, recently performed by Nick Loter on BLACKJACK 5 at Maxwell Laboratories, have been analyzed. These shots were all filtered by the addition of 1.5 mils of kapton and all except one shot, shot 2137, contained some magnesium. The mass loading ranged from about 80 to 400 ug/cm, while the resulting K-shell yields ranged from around 7 to 40 KJ. Table 1 summarizes the experimental parameters.

TABLE 1.* BLACKJACK 5 source performance during aluminum wire SXR series.*

Shot No.	Mass Loading (ug/cm)	K-shell FWHM (ns)	K-shell Yield (KJ)	Emitting Radius (cm)	Plasma Length (cm)
2111	53	30	8.6	0.065	3.1
2122	118	37	20.6	0.045	3.1
2125	161	57	32.3	0.050	3.1
2126	210	49	20.7	0.035	3.1
2127	210	51	32.9	0.050	3.1
2132	210	48	29.6	0.050	3.5(2.1)
2137	397	60	15.9	0.100	1.7

* Based on a table and other information provided by Nick Loter, Maxwell Labs.

Both the emitting radius and plasma length were estimated from pinhole pictures. Due to the resolution of the pinhole pictures, accurate measurements were difficult, therefore, the numbers quoted in Table 1 are approximate. The actual emitting radius can vary considerably along the length of the plasma column. Indeed in some cases, the emission region can pinch off entirely forming almost spherical blobs.

From table 1 and the spectra, the average K-shell energy production rate and the line ratios can be determined. These values are shown in Table 2. Note that the K-shell yields in Table 1 include a small amount of energy from the the magnesium lines. To account for this we have decreased the K-shell yields for all shots except shot 2137 by 5%. As with the emitting radius and length, there is some as yet unknown amount of uncertainty in these values.

TABLE 2. K-shell Production Rate and Line Ratios for aluminum shots.

Shot No	J/ns/cm	He-α/Ly-α	He-β/Ly-α	He-β/Ly-β
2111	88	0.66	0.12	1.11
2122	171	0.68	0.11	0.97
2125	174	0.86	0.13	1.41
2126	129	1.47	0.25	0.57
2127	198	1.26	0.11	3.16
2132	167(288)	0.68	0.14	2.10
2137	156	1.38	0.08	2.06

Analysis of Experimental Data

A fixed value of radiated power per centimeter will map out a single contour in (N_i, T_e) space, where N_i is the average ion density and T_e the average electron temperature. Similarly, the three line ratios will map out three different contours. The intersection of the contour for a fixed radiated power per centimeter with any of the contours for a fixed line ratio will give a single ion density and electron temperature. One can, therefore, obtain the average conditions needed to produce each of the line ratios seen in the experimental spectrum. By averaging all three temperatures or densities together, one would obtain an overall average temperature and density necessary to produce the K-shell emission seen. Figure 1 illustrates this for filtered shot 2125.
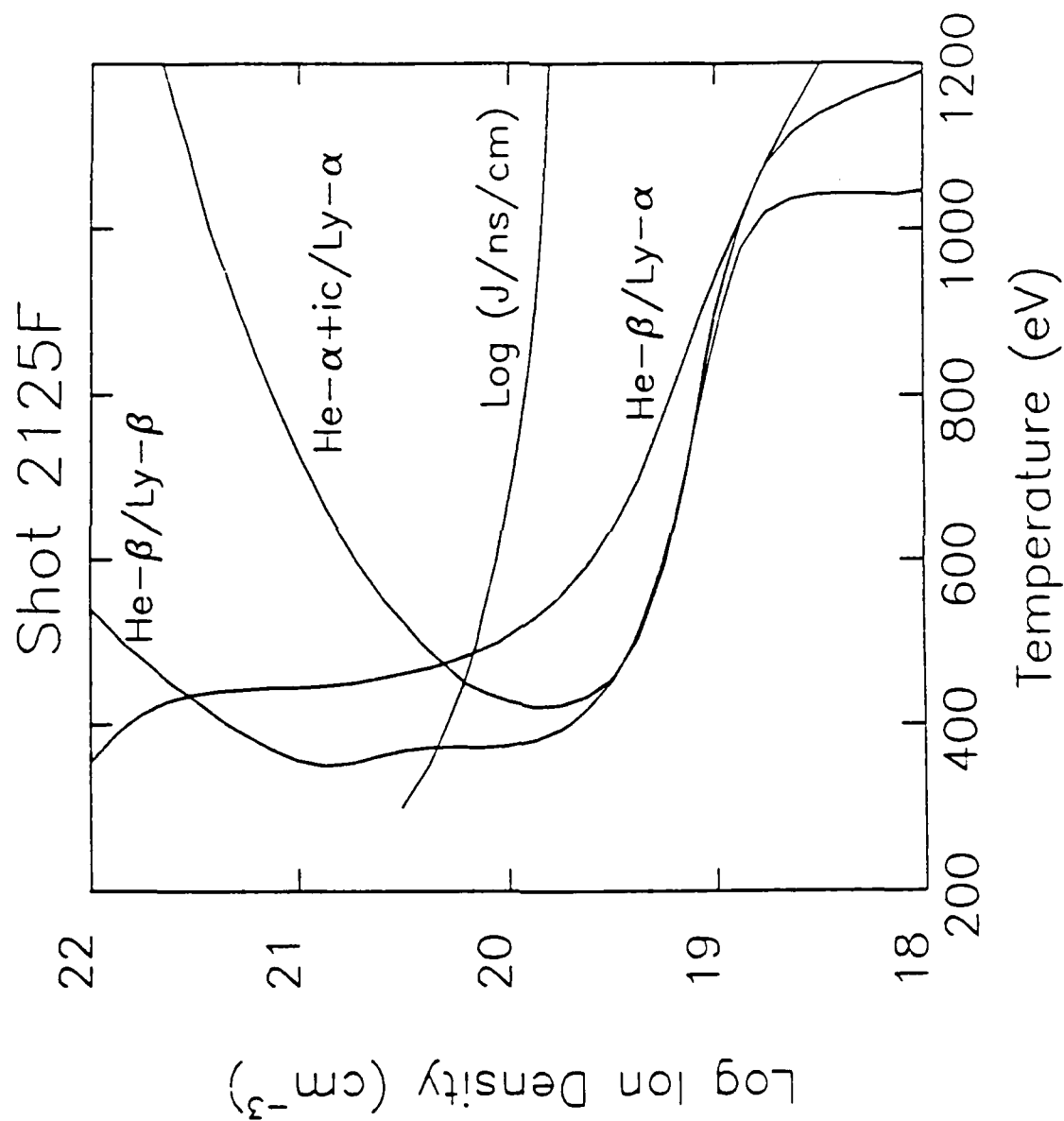
Figure 1. Intersection of the radiated power per centimeter with the three line ratios (He-α/Ly-α, He-β/Ly-α, and He-β/Ly-β) as a function of the logarithm of the ion density and the electron temperature for a homogeneous cylindrical plasma with a radius of 0.05 cm.

A separate estimate of the electron temperature can be made from the continuum. All four temperature estimates are shown in Table 3, while the three ion densities are listed in Table 4. The values quoted depend on the line ratios, size of the emitting region and yield. Any uncertainties in these quantities will result uncertainty in the estimate of the average temperature and ion densities reached during peak compression.

TABLE 3. Estimates of the Electron Temperature (in eV).

Shot No	From Continuum	From Intersection of J/ns/cm with:		
		He-α/Ly-α	He-β/Ly-α	He-β/Ly-β
2111		770	430	430
2122	800	570	500	420
2125	520	490	460	380
2126	435	380	410	530
2127		400	490	
2132	640	570(540)	450(480)	
2137		520	450	340

TABLE 4. Estimates of the Ion Density (cm^{-3}) from Intersection of J/ns/cm with the three line ratios.

Shot No	with He-α/Ly-α	He-β/Ly-α	He-β/Ly-β
2111	2.9×10^{19}	6.2×10^{19}	6.2×10^{19}
2122	1.4×10^{20}	1.7×10^{20}	2.1×10^{20}
2125	1.5×10^{20}	1.7×10^{20}	2.2×10^{20}
2126	2.6×10^{20}	2.4×10^{20}	1.7×10^{20}
2127	2.4×10^{20}	1.7×10^{20}	
2132	$1.2(2.2) \times 10^{20}$	$1.7(2.5) \times 10^{20}$	$3.4(5.3) \times 10^{20}$
2137	5.0×10^{20}	3.9×10^{20}	9.0×10^{19}

Conclusions

Using the ion density obtained from the intersection of the radiated power per centimeter (J/ns/cm) with the He-α to Ly-α line ratio, one can estimate the amount of mass that is radiating. This quantity is shown in Table 5. The last column gives the fraction of the initial mass that radiated.

An estimate of how sensitive the average electron temperature and ion density are to uncertainty in the size of the emitting region, the yield and the line ratios still needs to be done.

TABLE 5. Emitting Mass versus Initial Mass.

Shot No	Initial Mass (μg/cm)	Emitting Mass (μg/cm)	Fraction Emitting %
2111	53	17	33
2122	118	40	34
2125	161	53	33
2126	210	45	21
2127	210	84	40
2132	210	42(77)	20(37)
2137	397	70	18

References
1. Plasma Radiation Branch, 1988 DNA Final Report (1988)
2. M. C. Coulter and K. G. Whitney, NRL Memo Report 6383 (1988)

II. Atomic Data Aquisition

Complete data bases of collision strengths for the hydrogen-like to neon-like ionization stages of iron and selenium have been finished. Our next goal in the area of data bases is to complete the ionization stages of H-like to Ne-like for argon. The data base will include energy levels, transistion probablities, photoionization cross sections, ionization and excitation collision strengths and rates. This data will allow us to use the Z-scaling software that is under development to determine oscillator and collision strengths for $18 < Z < 36$. Otherwise, it would be prohibitive in time and storage either to calculate or store all the necessary oscillator and collision strength data for this large number of elements and ionization stages. It is sufficient to provide fits to a much smaller data base that is accurate enough for modeling and transport calculations moreover there is a built in reliability to this procudure for producing data.

The software used to discover the systemic trends which exist for atomic oscillator strengths has been developed and implemented successfully. The electric dipole oscillator strengths, computed using R. D. Cowan's atomic structure package, show smooth variations of the calculated values as a function of the nuclear charge, Z. The oscillator strength fit is of the form

$$f \approx f_0 + f_1 Z^{-1} + f_2 Z^{-2}$$

where f_0 is the hydrogenic oscillator strength. The helium-like and neon-like models have been completed.

The results from Cowan's Program RCG Mod 9 fit remarkably well into the systematic trends for both of the completed models. Table 1 gives the details of each model. Figure 1 is a plot of f-number versus nuclear charge for the He-like model. Transistions A and L show smooth variations with nuclear charge. As was expected, these two transistions are simply a multiplicative factor of the hydrogenic values. Curve K, as well as all other $\Delta n=0$ transistions, are distincitive in curvature and exhibit more pronounced 1/Z behaviour. This is a result of the hydrogenic value, f_0, being quite small. In hydrogen, $\Delta n=0$ transistions are degenerate which means the oscillator strengths are zero. Figure 2 shows two transistions from the Ne-like model.

The oscillator strength models that we are building have the advantage of being completely self-consistent. In other words, the random errors which have plagued similar

21

calculations and are a result of gathering avialable data from various sources have been completely eliminated.

Table 1: Oscillator Strength Models

Isoelectronic Sequence Modeled	Number of Energy Levels	Number of Transistion Probabilities	Transistion Arrays	Data Base
He	38	80	$1s^2 - 1s^1nl$ $1s^1nl - 1s^1n'l'$	Ne IX, Ar XVII, Fe XXV, Se XXXIII
Ne	51	83	$2s^2 2p^6 - 2s^2 2p^5 nl$ $2s^2 2p^6 - 2s^1 2p^6 nl$ $2s^2 2p^5 nl - 2s^2 2p^5 n'l'$ $2s^2 2p^5 nl - 2s^1 2p^6 nl$ $2s^1 2p^6 nl - 2s^1 2p^6 n'l'$	Ar IX, Ti XIII, Fe XVII, SeXXV

Finally, the development of software to fit collision strengths along isoelectronic sequences is well underway. The form that we are attempting to fit for the collision strength data is a two parameter fit in energy and nuclear charge.

$$\Omega(X) = F_1(Z)(A + BX^{-1} + CX^{-2}) + F_2(Z) \ln(X)$$

where $F_n(Z) = (Z - B_n)^2$ are screening factors and X is energy in threshold units.

The first stage in the process is an energy fit for each of the transistions. A simple procedure for the energy fitting to the data has been implemented for the Ne-like isoelectronic sequences of iron and selenium. A comparison of the two data sets provided a check for the relative correctness of the data. Because the matrix element is proportional to Z^{-2}, the collision strength magnitude should get smaller as Z increases. This fact led us to discover a serious error for a few of the transistions in the iron data base. This is illustrated in figure 3. The curve labeled C is the old iron data and is much lower than the selenium data for this transistion (curve B). Notice after correcting the mistake, the new iron data (A) and the selenium data are in the correct relative order. With the Ne-like iron corrected, we can proceed to the next stage in the scaling process.
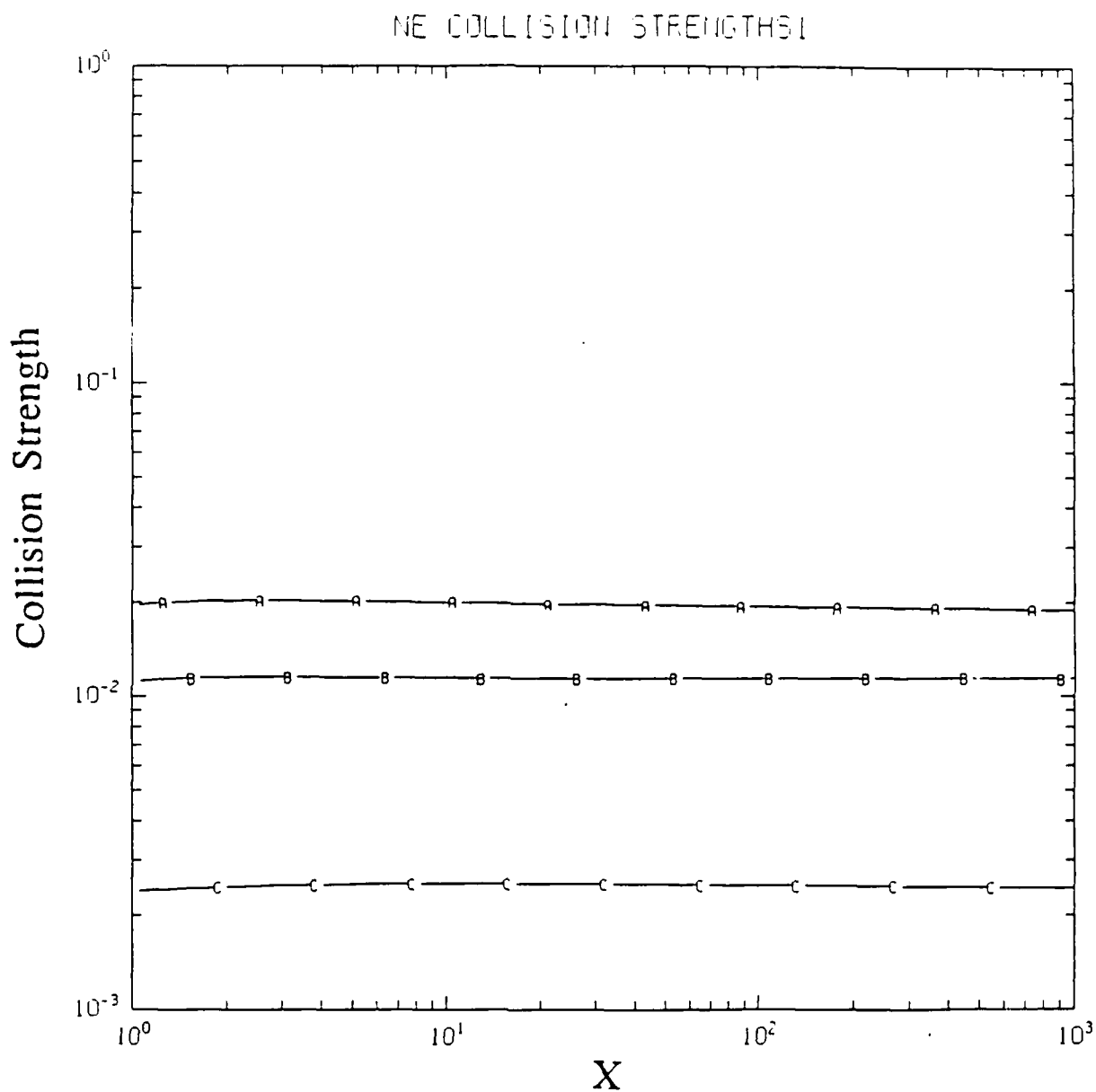
Neon-like trans.
$1s^2 2s^2 2p^6 - 1s^2 2s^1 2p^6 3s^1$
Fe - new(A), Se (B),
Fe - old(C)

F-NUMBERS
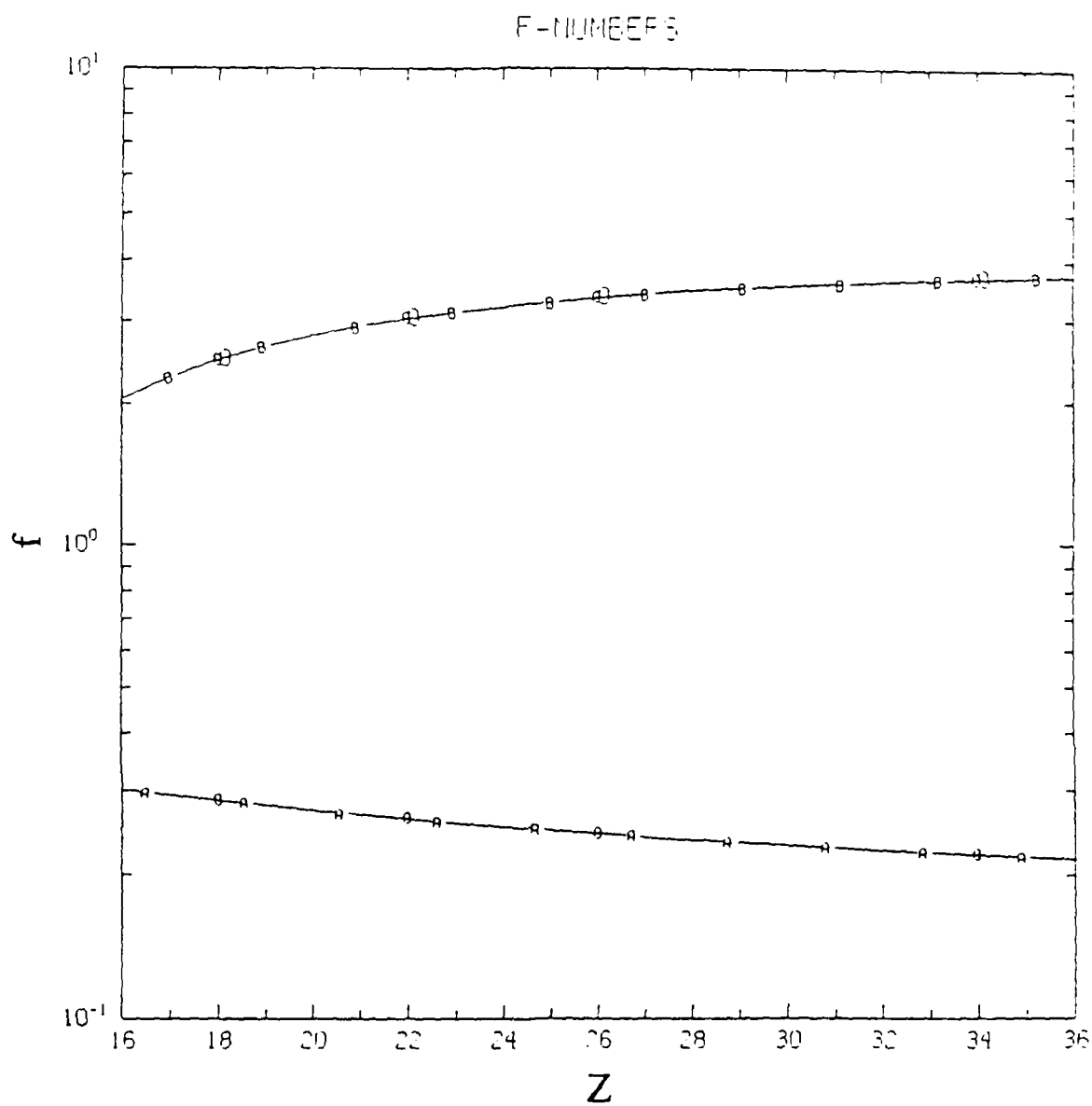
Neon-like   trans.
$1s^2 2s^2 2p^6 - 1s^2 2s^2 2p^5 3s^1$ (A)
$1s^2 2s^2 2p^6 - 1s^2 2s^2 2p^5 3d^1$ (B)

24

F-NUMBERS
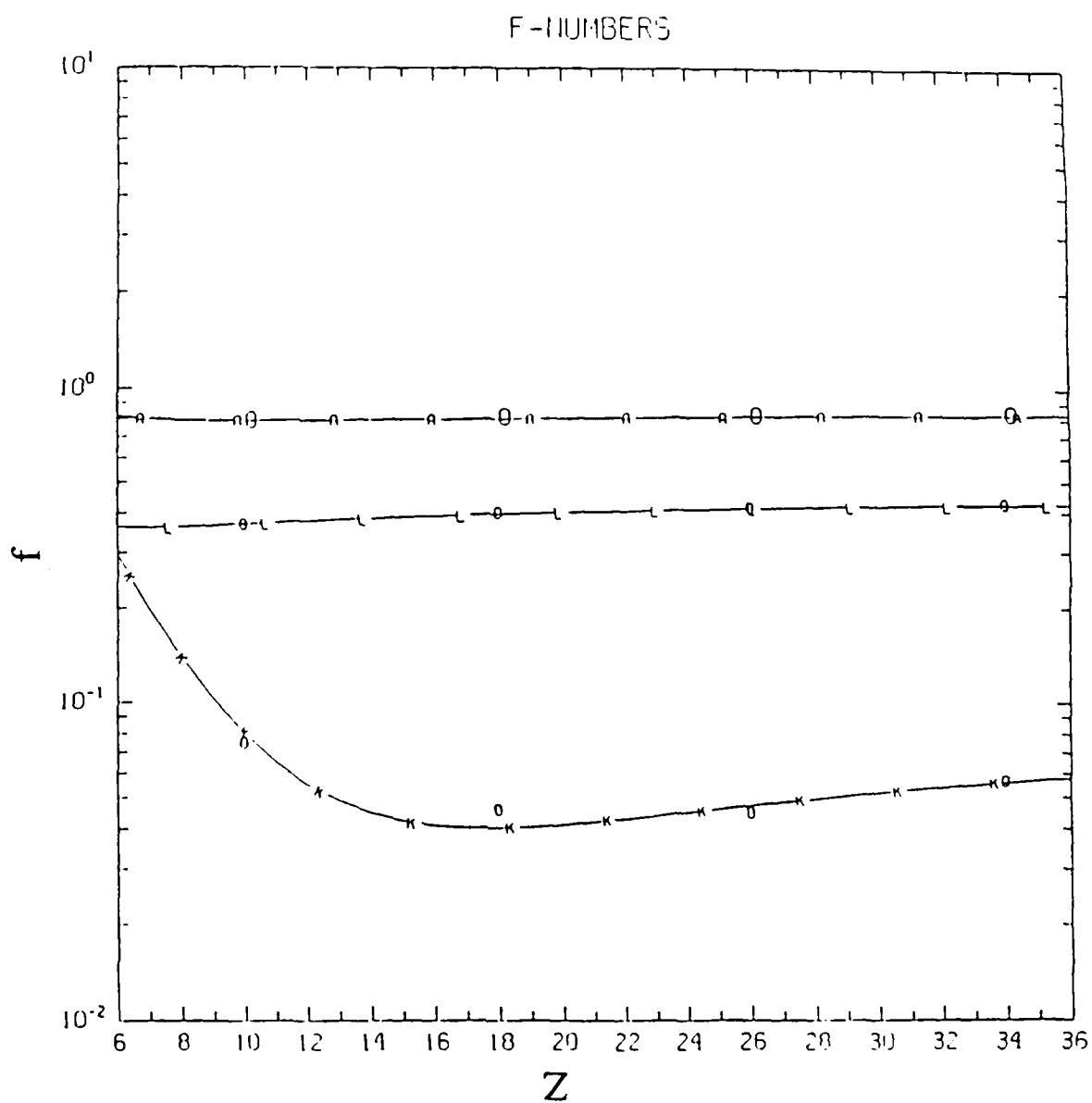
He-like   trans.
$1s^2$ - $1s^1 2p^1$ (A)
$1s^1 2s^1$ - $1s^1 2p^1$ (K)
$1s^1 2s^1$ - $1s^1 3p^1$ (L)

DIELECTRONIC RECOMBINATION RATE COEFFICIENTS FOR F-LIKE IONS AND Z-SCALING OF AUTOIONIZATION AND DIELECTRONIC RECOMBINATION RATES

Dielectronic recombination (DR) is an important recombination process for plasma diagnostics of atomic processes in high temperature and moderate density plasmas. The dielectronic satellite lines observed in the emission spectra as a result of these recombinations can be used for such plasma diagnostics. The models used to describe high temperature plasmas consist of rate coefficients for atomic processes in the ionization balance or transport equations. Semi-empirical formulas predict the total effective ground-to-ground DR rate coefficients at best within a factor of two. On the other hand, the calculations being carried out here for the first time will provide accurate DR rates into specific excited states (i.e. into the states that radiate) and from which the highly approximate total effective rate can be obtained, if needed, after summing the state specific rates. More improved calculations of   DR and accurate calculations of other rate coefficients are thus extremely important for their utility as proper plasma diagnostics and for accurate calculations of X-ray yields in the L-shell.

Dielectronic recombination is a two step process. In the first step , there is an initial capture of an electron by an ion X^{+z} into a doubly excited state $(X^{+(z-1)})^{**}$ which stabilizes by subsequent radiative decay to singly excited states $(X^{+(z-1)})^{*}$ or by autoionization to the initial state X^{+z} or any excited stated $(X^{+z})^{*}$ of the initial ion. In order to calculate the total DR rate from one ion stage to the next or even the total DR rates to a specific singly excited state of

the next ion stage, one has to calculate from a large number of doubly excited state all possible radiative decay rates as well as all energetically allowed autoionization rates . This amounts to calculating an enormous amount of radiative and autoionization rate data. However, for an accurate calculation of the DR rates, a detailed level accounting scheme, with extrapolations or configuration averaging only when sufficient convergence is present, is crucial.

In this years work we have completed the calculation of DR for ions of the flourine isoelectronic sequence covering ions with Z= 18,22,26 and 34. We have also calculated DR rates from neon like ions and we are thus in the process of developing scaling laws for these rates throughout the K- and L-shell ionization stages. We calculate DR rates by calculating autoionization rates and radiative rates from intermediate resonance states using a Hartree-Fock calculation with relativistic correction (HFR method of R. D. Cowan [1]). Approximate relativistic corrections in the radial wave functions as well as in the energies are included in this calculation. Thus calculation of DR rates involve calculations and organizations of a range of atomic quantities such as energies of the doubly excited and singly excited states, autoionization and radiative rates from each doubly excited states to each recombining states and final stabilizing states respectively. We thus developed computer codes to extract relevant quantities from the output files of this structure code calculations and stored and organized them into different data files so as that we can use them not just to obtain DR rates, but even configuration averaged autoionization rates , radiative

decay rates, and resonance excitation rates from a particular state to another.

This amounted to a large amount of bookkeeping and organizational work (which had to be done only once) since depending on the complexity of the ion there could be a very large number of doubly and singly excited states. In calculating the DR rates we are thus obtaining data which will give us other important rates besides DR rates such as resonance excitation rates as mentioned before or quantites needed for dielctronic satellite spectra calculations.

We expect that this method of calculation will give more accurate results than previously calculated DR rates using single configuaration non-relativistic wave functions or using a simple angular momentum averaged procedure by averaging over many intermediate states. On the other hand it is less time consuming and less complex than calculating α^{DR} using fully relativistic multiconfiguration Dirac-Fock (MCDF) method. Thus for calculating autoionization or DR rates for moderate Z ions, our method of calculating α^{DR} is a very good compromise between accuracy and computer time.

The DR rate coefficient α^{DR} from an initial state $|i\rangle$ into a specific stabilizing bound state $|k\rangle$ through a particular autoionization state $|j\rangle$ is given by :

$$\alpha^{DR}(i,j,k) = \left(\frac{4\pi}{T}\right)^{3/2} a_0^3 \; e^{-\epsilon_j/kT} \; \frac{g_j}{2g_i} \frac{A_{ji}^a A_{jk}^r}{\sum_{i'} A_{ji'}^a + \sum_{k'} A_{jk'}^r} \qquad (1)$$

for a Maxwellian distribution of electrons ; where g_i ang g_j are the statistical weights of the initial and doubly excited states respectively, T is the electron temperature and ε_j is the energy of the free recombining electron in Rydbergs. A^a_{ji} and A^r_{jk} are the autoionization and radiative rates from state $|j>$ to states $|i>$ and $|k>$ respectively.

The Auger transition probability for each doubly excited state is calculated from the perturbation expression

$$A_{ji}^{\ a} = (\ 2\pi/h\ )\ |<j|1/r_{12}|i>|^2 \qquad (2)$$

where $|j>$ and $|i>$ are intermediate-coupling wave functions and the radiative electric dipole transition probability from state $|j>$ to $|k>$ is given by

$$A_{jk}^{\ r} = (\ 2\pi/2J_j+1\ )\ |<k|T|j>|^2 \qquad (3)$$

where $<k|T|j>$ is the reduced matrix element. The transition matrix elements in Eqs. (2) and (3) can be expressed as sums of terms involving the product of angular integrals and radial integrals. These matrix elements were calculated using Cowan's atomic stucture code[1].(RCG Mod 9)

Most published works[2,3] report only the total dielectronic recombination rates $\sum_{m, j, k} \alpha^{DR}(m, j, k)$,where the summation over m extends over all levels of the ground configuration $|i>$ of the ion, as a function of temperature and the sum extends over all the singly excited bound final states as well. However, separate bookkeeping and presentation

of partial atomic data such as the autoionization rates A_{ji}^a from state $|j\rangle$ to state $|i\rangle$, radiative rates A_{jk}^r from state $|j\rangle$ to all singly excited levels $|k\rangle$ below the ionization limit and dielectronic recombination rates $\sum_j \propto^{DR} (i,j,k)$ from initial state $|i\rangle$ to specific final state $|k\rangle$ are extremely important for various reasons. With only the total rate coefficients, it is not possible to study density effects on these rates and to calculate DR rates accurately at densities of PRS (Plasma Radiation Source) interest, dielectronic recombination rates to these specific singly excited bound states are needed. Therefore, considerable effort was expended to set up the computer bookkeeping to isolate these rates and to define and calculate the necessary data files to make this data available to other of the ionization calculations that are to be carried out in this DNA program.

To calculate Dielectronic recombination from F-like ion to a Ne-like ion the initial continum states before recombination are taken to be:

$$1s^2 2s^2 2p^5 \ (^2P) \quad \text{and} \quad 1s^2 2s 2p^6 \ (^2S)$$

The autoionization states for $\Delta n \neq 0$, where n refers to principal quantum number of the excited electron are :

$$2s^2 2p^4 3ln'l' \ , \ 2s 2p^5 3ln'l' \ \text{and} \ 2s^0 2p^6 3ln'l'$$

These states stabilize by dipole allowed radiative transitions to the following states:

$$2s^2 2p^5 n'l' \quad \text{and} \quad 2s 2p^6 n'l'$$

where n' and l' represent the quantum numbers of the captured electron.

For $\Delta n=0$ transitions, the autoionization states are of the form $2s2p^6n'l'$ and these can stabilize by radiative decay to $2s^22p^5n''l''$, $2s2p^6n''l''$ and to the ground state $2s^22p^6$ of Ne-like ion. These transitions become energetically possible for high Rydberg states, specifically for higher Z ions such as selenium. Additional autoionization to excited states of the recombining ion included $2s^22p^43l$ and $2s2p^53l$ states whenever they were energetically possible.

In this present calculation, we neglected the cascade effect, i.e, radiative transitions leading to other autoionization states since it is assumed that its contribution in reducing the DR coefficients is very small.

For $\Delta n \neq 0$, we calculated the radiation rates A^r and autoionization rates A^a, i.e, α^{DR} explicitly for $n \leq 10$ and $l' \leq 6$. For states with $n>10$, the DR coefficients were obtained by using the $1/n^3$ extrapolation to these coefficients. For $\Delta n=0$, as mentioned before, autoionization transitions become energetically possible for $n \geq n_o$ where n_o varies from ion to ion. For each ion the value of n_o was determined by computing the energy levels of the autoionizing state. We calculated the transition rates for $n_o \leq n \leq 15$ and $1 \leq 8$ for these $\Delta n=0$ transitions. For states with $n > 15$, the radiative rates remained constant where as the autoionization rates were extrapolated by the usual $1/n^3$ extrapolation procedure. For $\Delta n=0$, radiative decay from the Rydberg electron is found to contribute significantly to the DR rate coefficients. For the autoionization states of the $2p^53lnl'$ configurations, these states can autoionize to the excited states of the initial ion as

mentioned before. We have also included these autoionization channels in our calculations.

These rates were calculated using the structure code of R.D.Cowan[1]. The calculations were done in the Hartree-Fock approximation. Relativistic terms were included in the differential equation to give relativistic correction to the radial wave functions as well to obtain improved energies. The continum wave functions were calculated in the distorted wave approximation. All calculations were carried out in intermediate coupling and single configuration approximation. Thus configuration interaction between autoionizing states were neglected in this calculation.

DR rate coefficients for the F-like ions were calculated for ions with Z=18,26 and 34. We have also completed a similar calculation for F-like titanium with Z=22. However, the results for Ti is not included in this report. These rates were calculated and new bookkeeping procedures were set up using the atomic structure code of R. D. Cowan[1]. Data files were created for each ion with a specific structure for calculating and storing the data. We have calculated and stored the energies of the doubly and singly excited Ne-like states with respect to the ground state of F-like state. The energy level structure of the Ne-like autoionizing and singly excited states are built such that high Rydberg states with closely lying energies are grouped together and identified as one level. In this present caculation, we include all autoionization states with Rydberg electron having principal quantum number upto n=10 or 15 for $\Delta n \neq 0$ and $\Delta n = 0$ respectively. We included all possible Auger decay and

radiative decay channels including autoionization to excited states. Radiative decay to other autoionization states, i.e, cascade effects were not included in this calculation. It has been seen from other DR calculations that the contribution of this cascade effecft is only about 3-4% of the total DR rate. We calculated and stored from each doubly excited state , all possible autoionization rates, and all possible radiative and dielectronic recombination rate to each specific singly excited state. After calculating the individual autoionization rates and radiative rates we calclate and store the branching ratio

$$A^{DR}(i,j,k) = \sum g_{j'} \frac{\sum_m A^a_{j'm} \sum_k A^r_{j'k}}{\sum_m A^a_{j'm} + \sum_{k'} A^r_{jk'}}$$

relevant for calculating the DR rate coefficient. The DR rate coefficient is then calculated from each doubly excited state to each singly excited state for each electron temperature in the range $0.01 \leq T \leq 10$ keV by using Eq. (1). The partial DR rates are then summed over the final singly excited states to obtain the total DR rate from F-like ground state to Ne-like state.

In Figs. 1-3 we present these DR rate coefficients for Ar^{9+}, Fe^{17+}, and Se^{25+} for the ^2P ($\Delta n \neq 0$), ^2P ($\Delta n = 0$) and ^2S initial states as a function of electron temperature. It can be seen from the graphs that the peak values of the rate coefficients is at higher temperatures for ions with higher Z values. From Fig. 2 we also notice that for $\Delta n = 0$ transitions, the DR rates are very large at very low temperature and becomes insignificant at higher temperatures. This is because the doubly excited

states for these   transitions are lying just above the initial ground state.

For $\Delta n \neq 0$, the low lying doubly excited states i.e,states with Rydberg electron having low principal quantum number ($3lnl'$,$n \leq 4$) contribute 30-60% to the total rates for Ar^{9+} through Se^{25+} respectively. Thus for higher Z ions, the contribution of low-lying states is much more significant compared to those with high Rydberg states. The partial DR rate coefficients from $3lnl'$ configurations are compared in Fig. 4 for Z=18 through 34. It is seen from this figure that the high n values become important for higher temperature.

The dielectronic recombination for the F-like ions have been investigated by different authors for several ions . Roszman[2] has done a non-relativistic Hartree-Fock calculations where the orbital energies, autoionization and radiative rates are calculated in the single configuration, LS-coupled, distorted wave approximation. Chen[3] on the other hand has calculated DR rate for F-like ions using a fully relativistic multiconfiguration Dirac-Fock model(MCDF). They have taken into account configuration interaction among states in the same complex. Figs. 5-7 present comparisons of our results with the other two calculations. In Fig. 5 , we compare our results for Ar^{9+} and Fe^{17+} (^2P, $\Delta n \neq 0$) with the nonrelativistic HF calculation of Ref. 2 . We see that our rates are always higher (by 35% at the maximum value at 0.2 and 0.4 keV for Ar^{9+} and Fe^{17+} respectively). In Fig. 6 we compare our results for Fe^{17+} and Se^{25+} (^2P, $\Delta n \neq 0$) with MCDF calculation of Chen[3]. Our results are very close to the results of Ref. 3. (higher by less than 8% at the

maximum value for both Fe^{17+} and Se^{25+}). All results of ref. are the angular momentum average results. Even though we expected to be closer to the nonrelativistic HF results of Roszman[2] compared to the relativistic results of Chen[3] ,the much closer agreement with Chen[3] suggest that relativity may not play a significant part in the DR rate coefficients. The differecne between our results and those of Roszman's[2] could be due to the sensitivity of the differences in the atomic models used in each case. In Fig. 7 we compare the total DR rate coefficients for the initial ^2P state of Fe^{17+}. Again, results of this calculation is closer to those of Chen[3] than the non-relativistic calculation of Roszman[2] In Figs. 8-12 we present graphs of energies,autoionization rates, radiative rates and DR rate coefficients for several doubly excited states as a function of Z. Thus using these graphs, energies of doubly excited states , autoionization rates, radiative rates and DR rate coefficients can be found for the particular Z of interest. In fig. 8 we present the energies of the 3131' doubly excited states as a function of the atomic number Z. In Fig. 9 we show the Z-scaling of the oscillator strength for the 3131' configurations for n=3→2 radiative decay rates. The oscillator strength can be written as

$$f^{rad} = (g_u / g_1) (mc/8\pi^2e^2) \lambda^2 A_{ul}^{rad}$$

where g_u and g_1 are the statistical weights of the upper and lower states respectively, λ is the wave-length of transition and A_{ul}^{rad} is the radiative decay rate. The oscillator strength scales like

$$f^{rad} = a_0 + a_1/Z + a_2/Z^2$$

The oscillator strength is mostly independent of Z whereas the radiative rate scales as Z^4. It can be also justified that the autoionization rates are independent of Z. We therefore define a f-number for the autoionization rate equivalent to the oscillator strength for radiative decay.

$$f^{ai} = (g_u / g_l) (mc/8\pi^2 e^2) a_0^2 A_{ul}^{ai}$$

$$= b_0 + b_1/Z + b_2/Z^2$$

where A_{ul}^{ai} is the autoionization transition rate for transition from state u to state l. In Fig. 10 and Fig. 11 we show the Z-dependence of these autoionization f-numbers for autoionization from 3131' doubly excited states to the first excited (^{2}S) and ground (^{2}P) states respectively. Thus using Cowan's code , we have found the scaling relations with atomic number of energies, autoionization rates, and radiative rates from doubly excited states in Ne-like ionization stage. From these scaling relations, those for the Dielectronic recombination rates into the neon like singly excited states can be found for any temperature. In Fig. 12 we present the Z-dependence of the DR rates from ground ^{2}P state to $2p^5 3s$ excited state for temperatures T= 100, 200, 300, and 600 eV. In developing the Z-scaling of autoionization, radiative and DR rates, only 3131' autoionization doubly excited and n=3 singly excited Ne-like states have been considered. It is

expected that the higher autoionizing states ($3lnl'$ with $n \geq 4$ and $nlnl'$ with $n,n' \geq 4$) and singly excited states with $n \geq 4$ will also scale accordingly.

Because of strong heating of a plasma, the distribution of atoms among the various ionization stages is no longer best represented by the Maxwellian electron distribution function. When the excitation and ionization rate coefficients are integrated over non-Maxwellian rather than the usual Maxwellian electron distribution function, they do not detail balance with the deexcitation and recombination (including dielectronic recobmination) rate coefficients. This leads to significant shifts in ionization abundances as a function of temperature and in the excited state population distribution. Thus using the branching ratio A^{DR} obtained for this F-like calculation and integrating it over Maxwellian as well as non-Maxwellian distribution function, we found important effects of these rates on the excited state population of F-like ions.

We will soon complete our Z-scaling calculation by scaling the energies and autoionization and radiative transition rates for doubly excited states with high Rydberg electrons. With the use of such scaling laws, it will be possible to carry out more accurate analyses of the feasibility of different elements in the isoelectronic sequence as plasma sources for Z-pinches. Equally important, scaling will allow us to obtain these rates throughout the portion of the periodic table of interest to DNA Z-pinches with a great saving in the amount of theoretical effort expended than would otherwise be needed if they were calculated directly as was done with Ar, Ti, Fe, and Se.
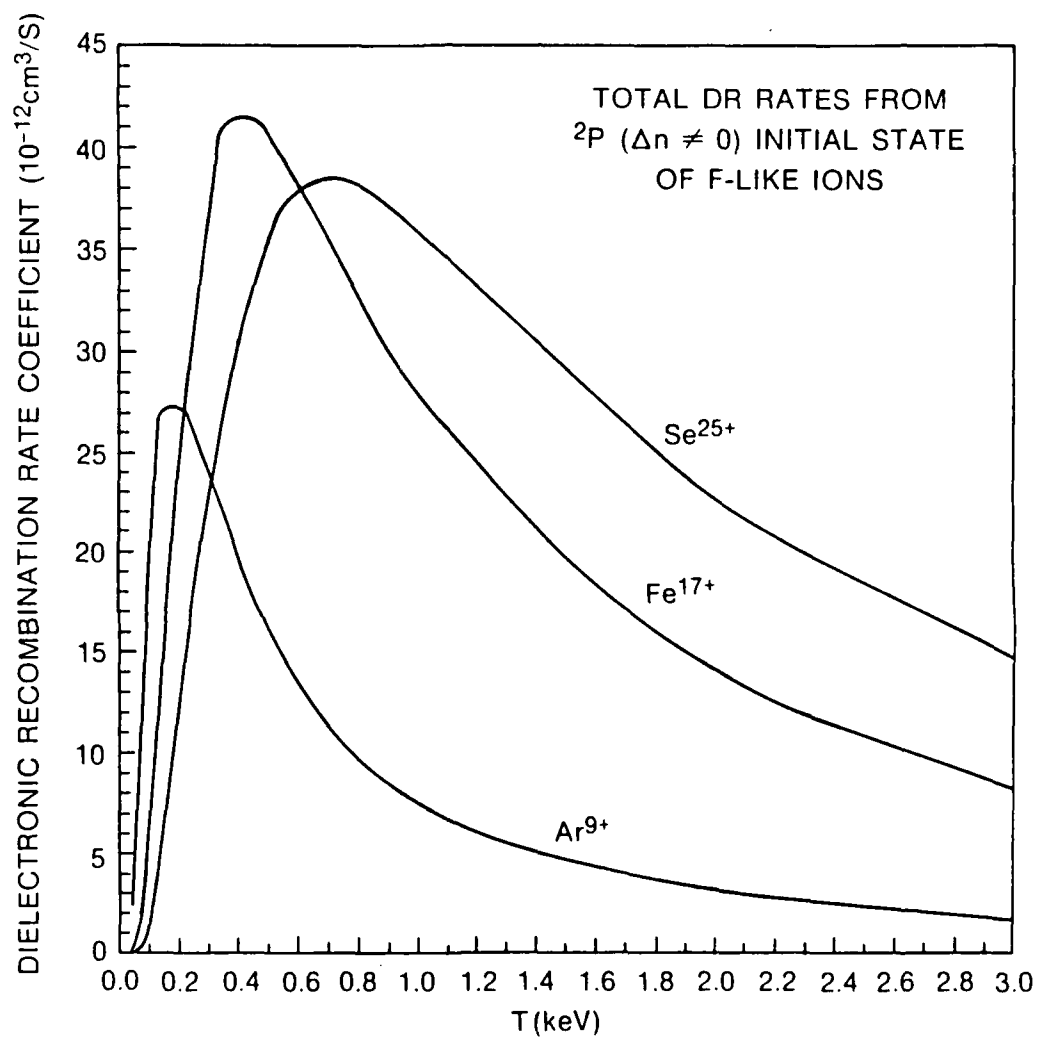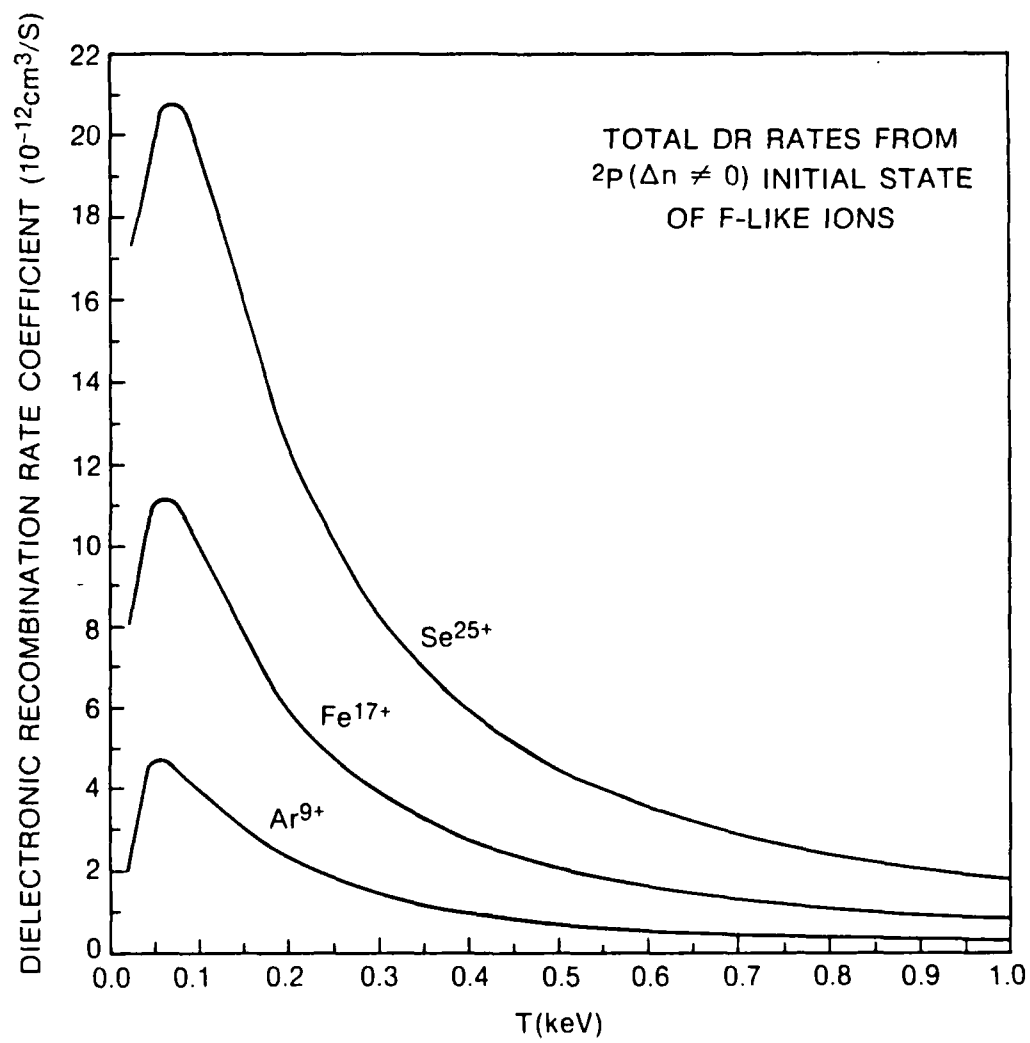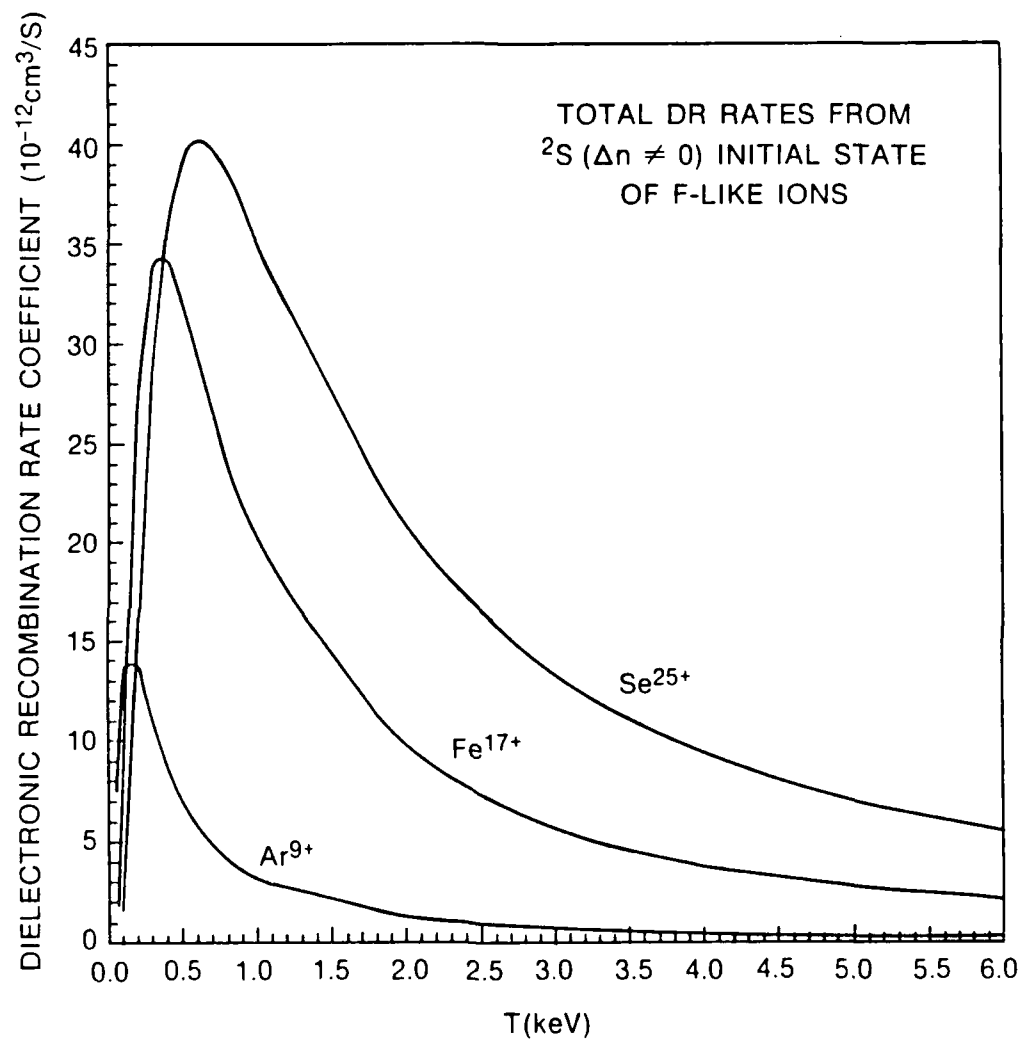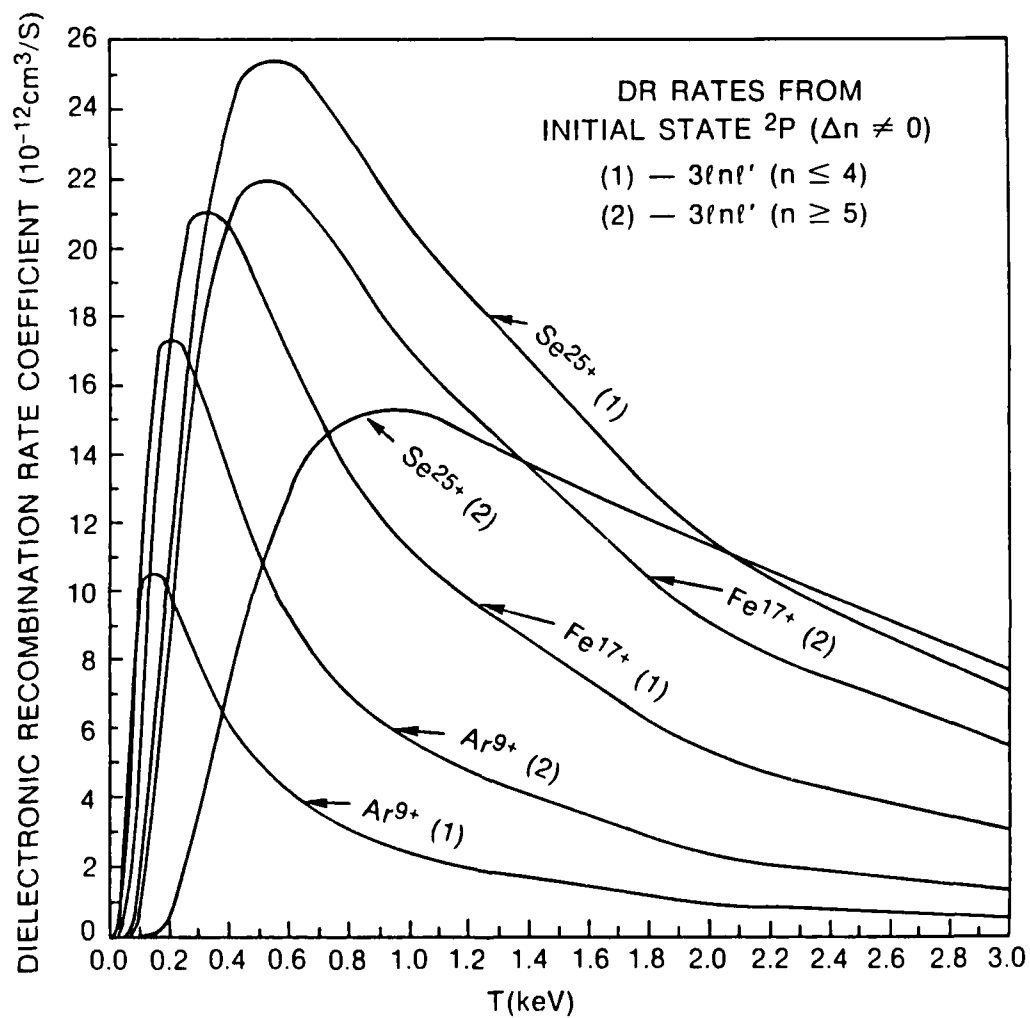
Figure 1

38

Figure 2
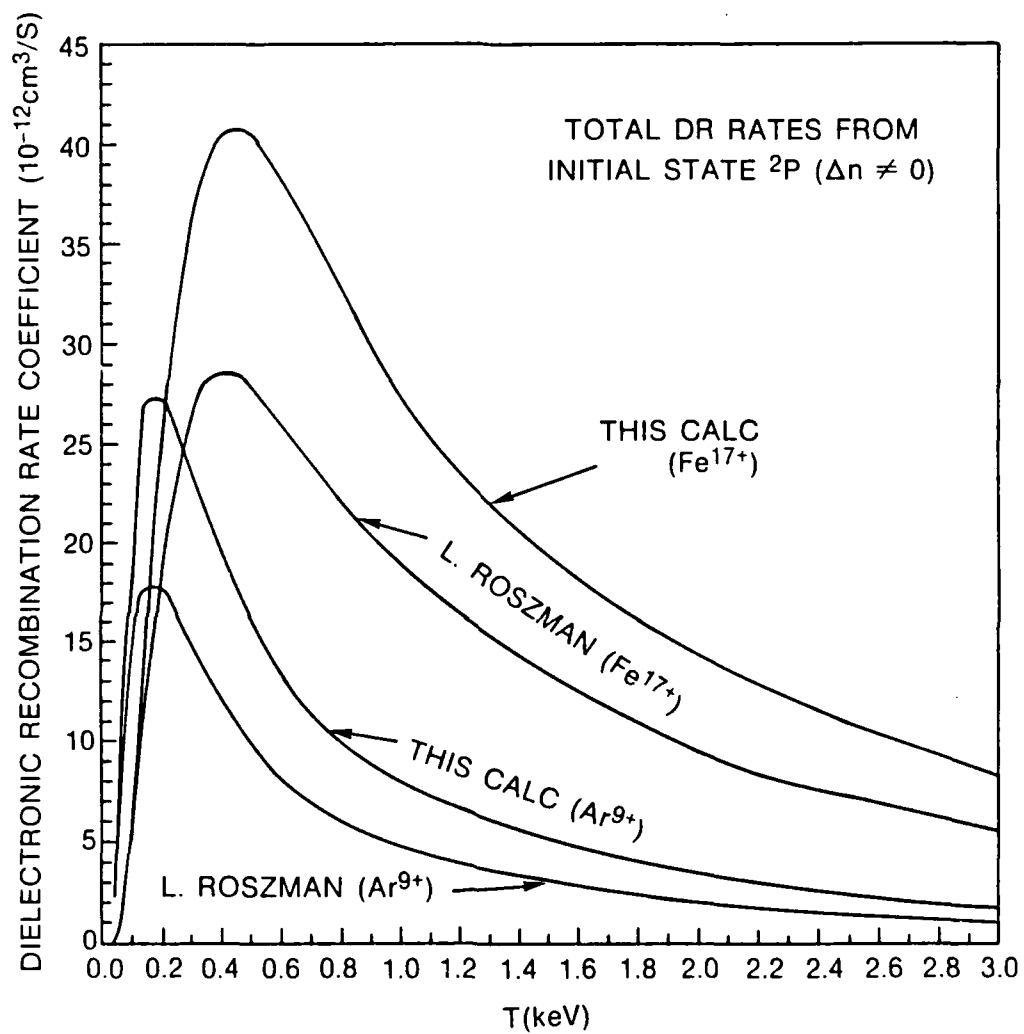
Figure 3

Figure 4

Figure 5

Figure 6

Figure 7

doubly excited state energies

1: $2p^4 3p 3d$
2: $2p^4 3d^2$
3: $2s 2p^5 3p^2$
4: $2s 2p^5 3s 3d$
5: $2s 2p^5 3p 3d$
6: $2s 2p^5 3d^2$
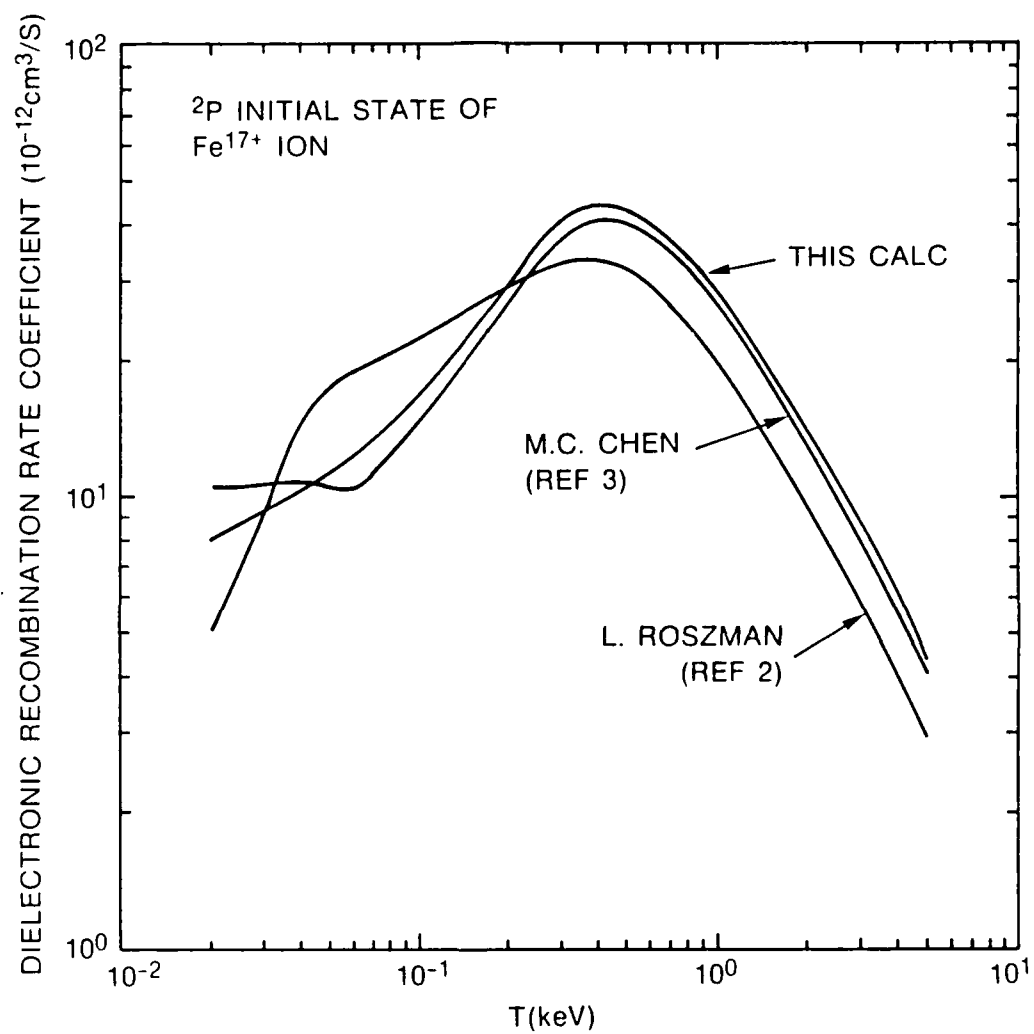
Figure 8

45
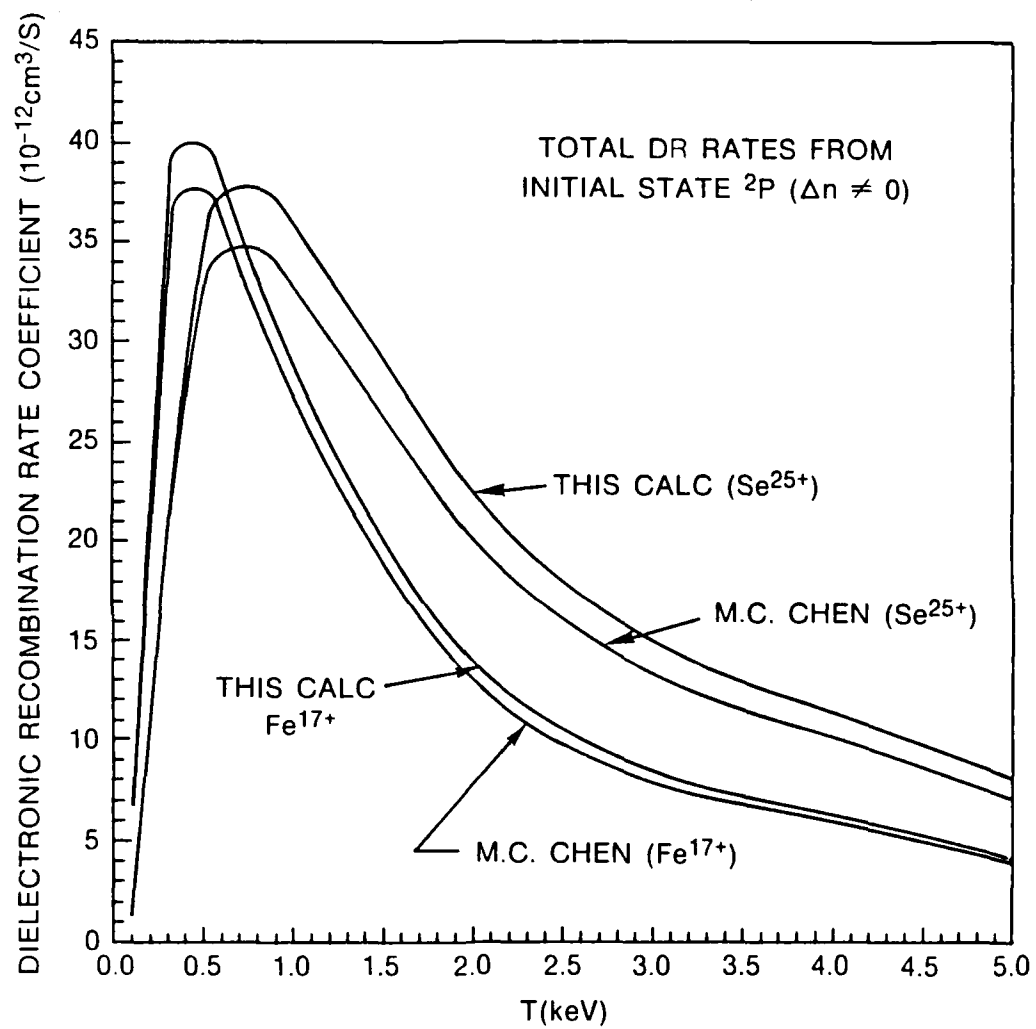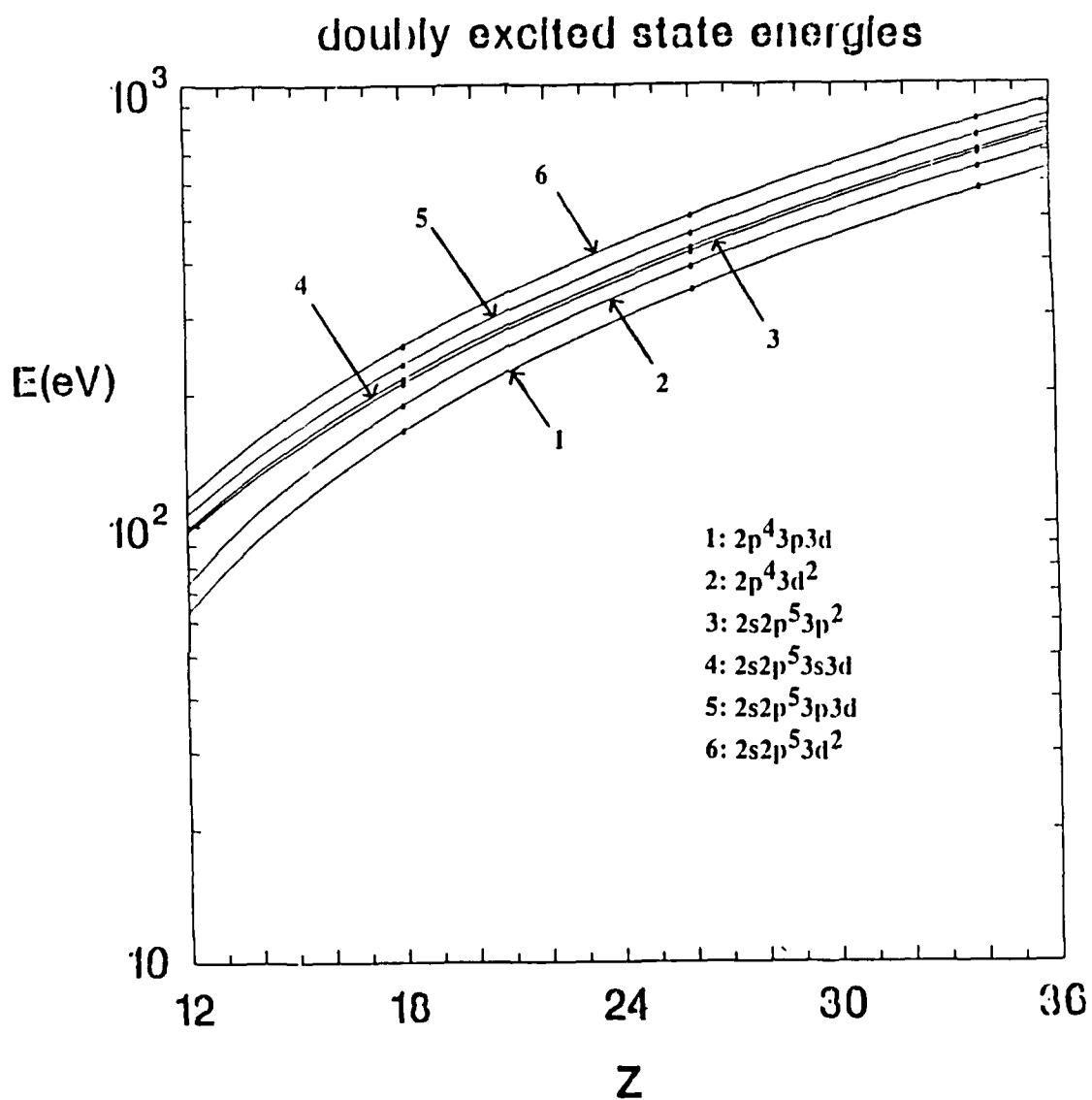
RADIATIVE DECAY TO SINGLY EXCITED STATES

Figure 9

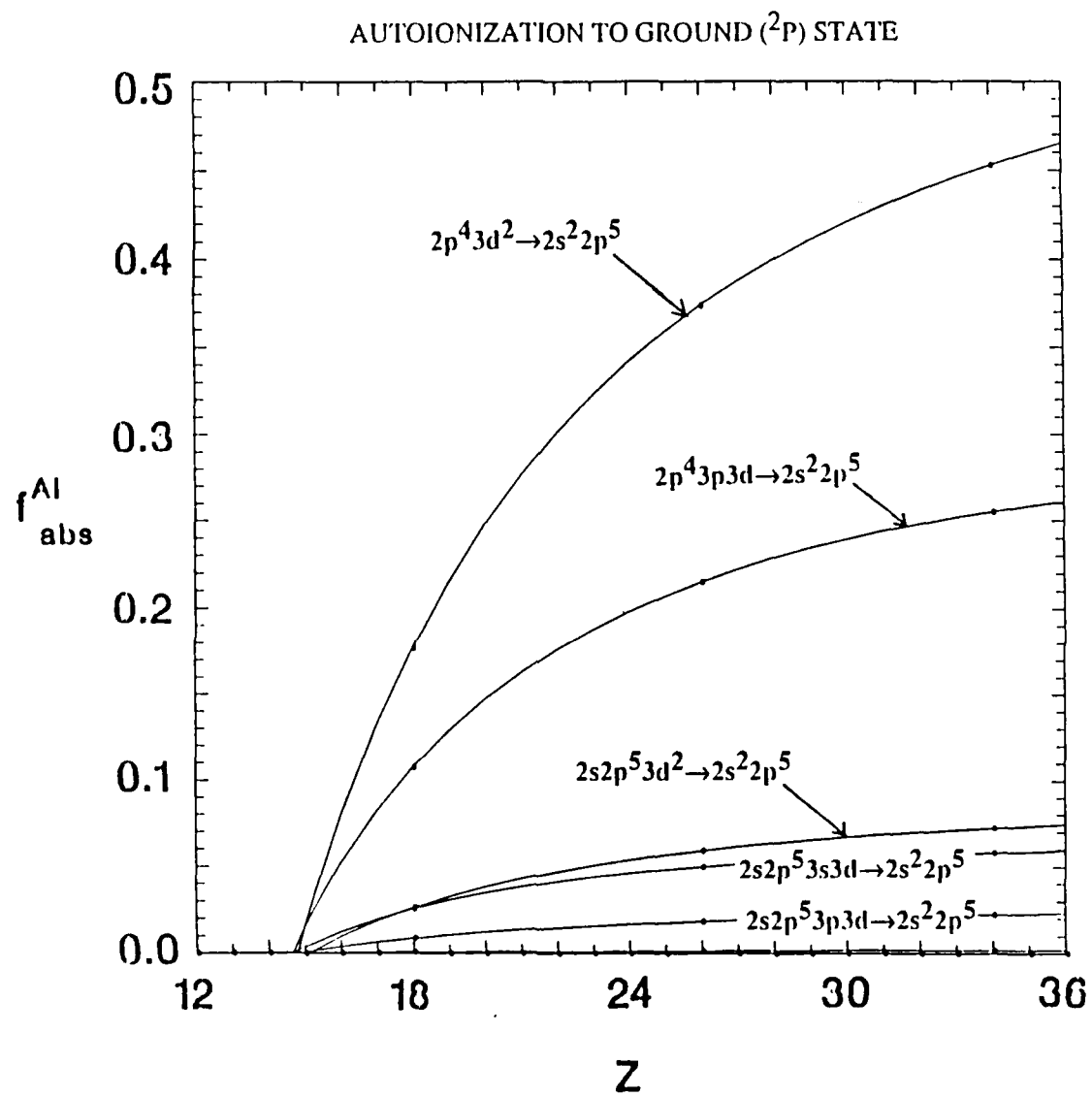AUTOIONIZATION TO FIRST EXCITED (^{2}S) STATE

Figure 10

47

AUTOIONIZATION TO GROUND (^{2}P) STATE
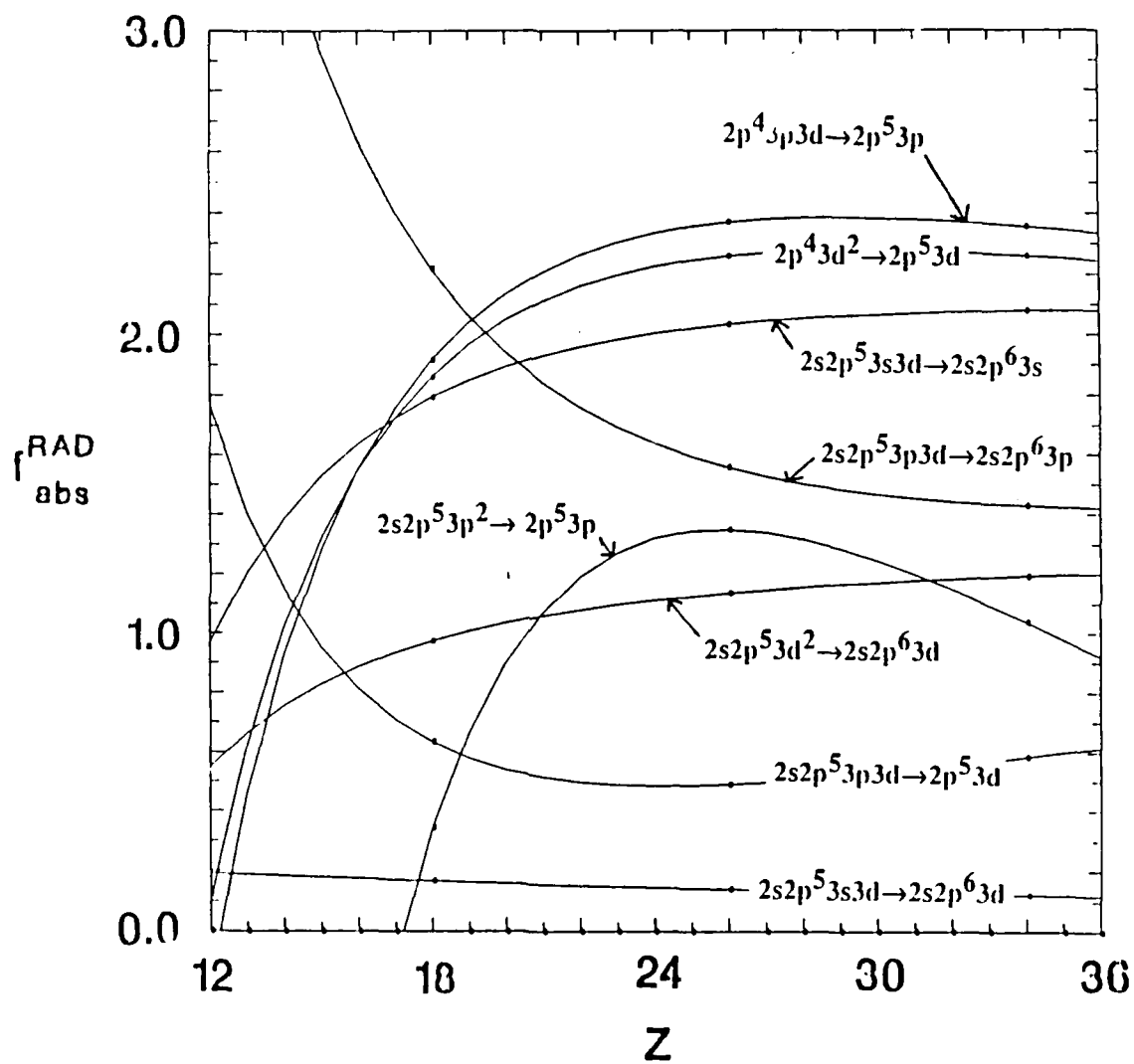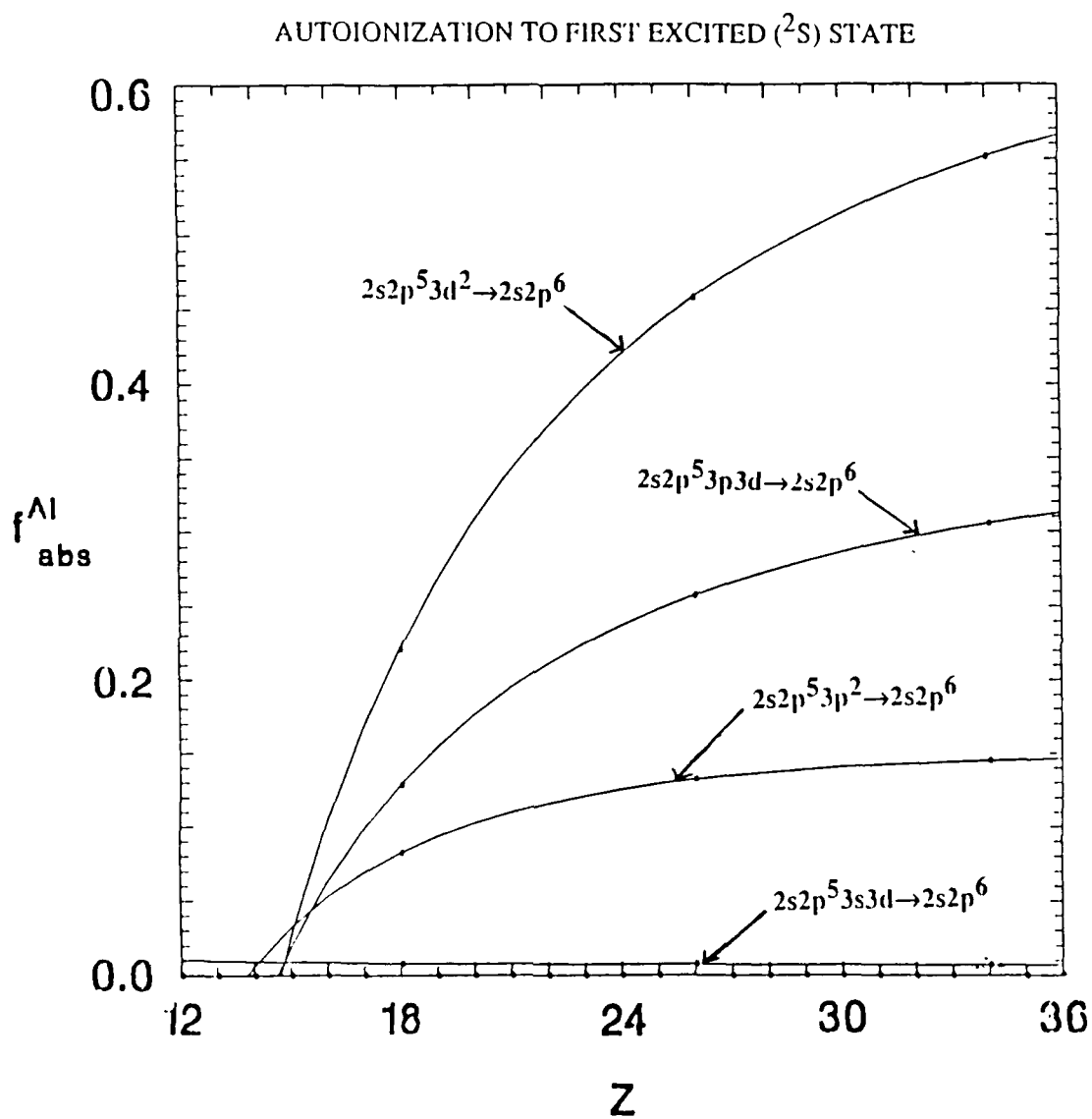
Figure 11

DR FROM GROUND STATE TO $2s^2 2p^5 3s$ STATE

$\alpha^{DR}_{(cm^3/sec)}$

Z

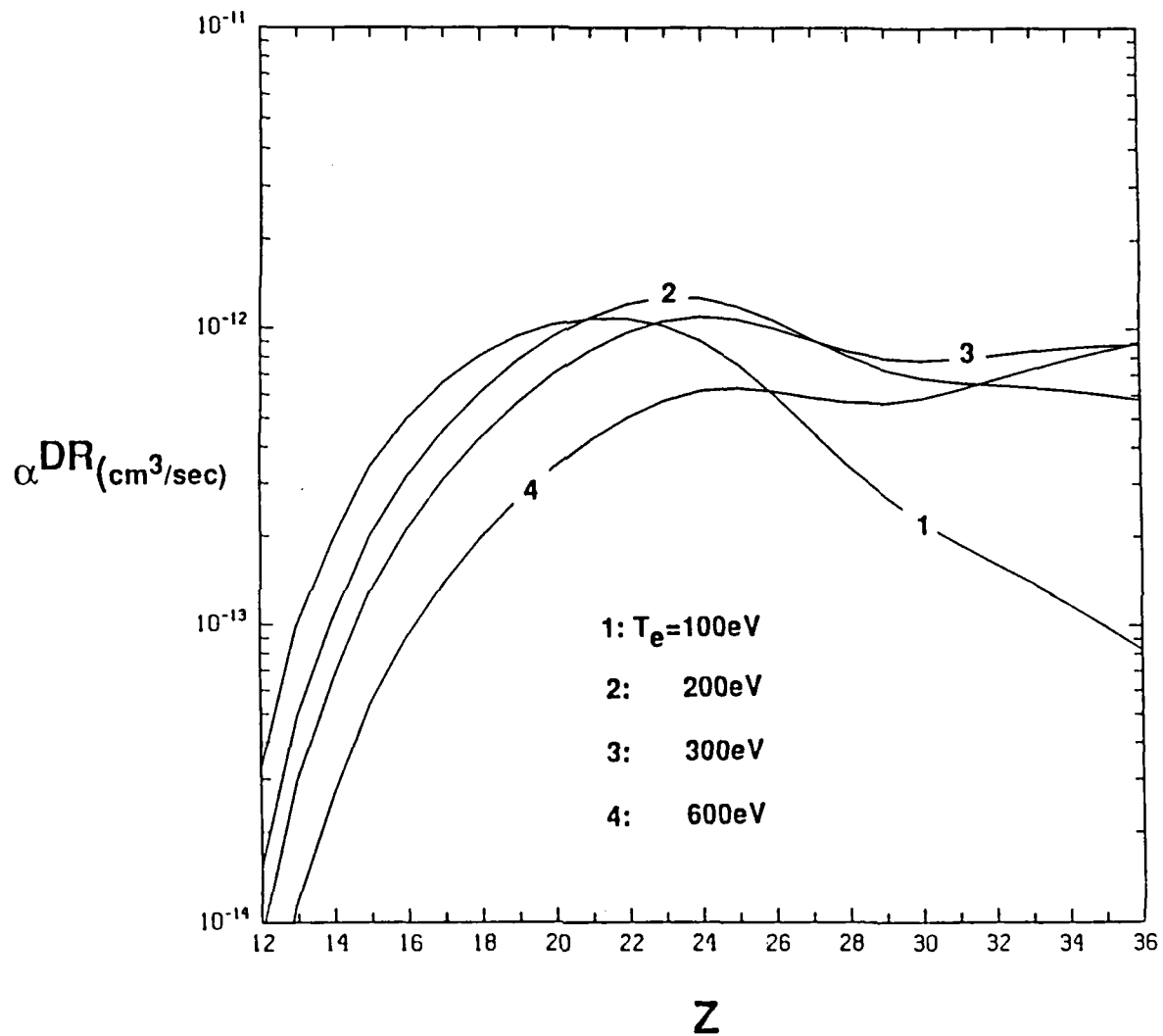1: T_e=100eV

2:     200eV

3:     300eV

4:     600eV

Figure 12

REFERENCES

1. Atomic Structure Code of Robert D. Cowan following his book, "The Theory of Atomic Structure and Spectra," (University of California Press, Berkeley, 1981).

2. L. J. Roszman, Phys. Rev. A 35, 2138 (1987).

3. M. H. Chen, Phys. Rev. A 38, 2332 (1988), Phys Rev. A 35, 2138 (1987).

III. RADIATIVE COLLAPSE

One of the important objectives of the Radiation Hydrodynamics Branch is to promote understanding, interpretation, and prediction of the dynamics and radiation from a Z-pinch implosion based upon numerical simulations. Such studies can lead to new methods and approaches for improved coupling between the pulse power machine and the pinch load, as well as enhancement in the radiative yields from the implosion. The ideal configuration of the machine and load would lead to a radiative collapse wherein a large fraction of the energy delivered to the load is returned as radiation in the keV range, while only a small fraction is lost to turbulent kinetic motions. For example, a 3 MAmp machine could ideally yield over a hundred kJoules in keV radiation from the radiative collapse of an aluminum implosion. The central question is how such an ideal machine-load configuration which exists in principle can be realized in practice. To this end we have been studying the Z-pinch implosion of wire arrays coupled to a realistic circuit which models the pulse power machine.

Unfortunately, it is known that <u>ab initio</u> numerical simulations of PRS Z-pinch loads with radiation hydrodynamic codes do not at present correctly predict many of the radiative and dynamic features observed in implosions. Thus the first theoretical task in devising the ideal machine-load configuration is to determine the reasons for the existing disagreement. In the present section we summarize a new set of simulations which extend previous modeling by including the effects of (i) a short circuit in the pulse power feed, and (ii) a phenomenological anomalous resistivity in the pinched plasma. This study is part of an ongoing effort to uncover those physical processes which will bring the simulation results more into line with the experimental data. The present results for the pinch

radii, total and K-shell yields, and K-shell pulse widths are encouraging but still do not exactly match the observations.

The present simulations were done for aluminum wire array implosions on the Double Eagle pulse generator of Physics International. This choice was motivated by the recent set of experiments on this machine and the accompanying excellent data set kindly provided to us by C. Deeney of Physics International. For the numerical simulations we used the ZPIMPO radiation-magnetohydrodynamic code. This code has been fully describe in an NRL Memorandum Report #6448. Briefly, the ZPIMPO code is a single zone ("0-D") cylindrically symmetric hydrodynamic code, i.e., the plasma dynamics and state is modeled as a shell with uniform density and temperature and separate momenta equations for the inner (R_{in}) and outer (R_{out}) radii. The diffusion of the magnetic field, however, is followed over several zones in order to model the current penetration into the plasma and resistive heating correctly. The ionization state of the plasma in the shell is followed by solving time dependent rate equations. The radiation transport uses the probability of escape formalism for the lines and edges and multi-frequency for the free-free emission. The sole advantage of this single zone modeling compared to a full multi-zone 1-D code is the efficient running time and consequent ability to survey a large range of parameter space in a cost effective manner.

The magnetohydrodynamics in the plasma is coupled self-consistently to an equivalent circuit model for Double Eagle shown in Fig. 1. The voltage source supplied by the generator V_{source} is a known function of time, while the feed from the insulator stacks to the load is characterized by fixed inductances L_a and L_b, and a fixed resistance R_a. In the discussion presented below we have considered the effect of a short circuit in the feed with a variable resistance R_s. The location of the short divides the total feed inductance into a part before the short and a part after the short.

The currents to be determined in the circuit are denoted by I in Fig. 1. The imploding plasma provides the load voltage V_{load}.

We considered three sets of runs, comprised of six cases each. The first set, termed the standard set, has no short in the feed and uses classical Spitzer resistivity. For the second set we added a short in the feed once the load voltage exceeded 3 MVolts. The third set also has a short but in addition we employed a phenomenological resistivity which increases as the plasma pinches. Specifically

$$\eta = \eta_{Spitzer} \times \left[1 + \beta \left[1 - \left(\frac{R_{out}(t)}{R_{out}(0)} \right)^2 \right] \right] . \qquad (\star)$$

The parameters for the three different run sets are summarized in table I.

TABLE I

SET PARAMETERS

run set	short	resistivity
A	no	Spitzer
B	yes	Spitzer
C	yes	eqn.($\star$) with $\beta=100$

Since the load is an array of solid wires the initial conditions in a cylindrically symmetric model are the total mass of the array and its radius R(0). The initial conditions for the six cases in each run set are listed in table II.

TABLE II

INITIAL CONDITIONS

case	Mass	R(0)	$M*R(0)^2$
	μgm	cm	μgm$*$cm^2
1	2222	0.3	200
2	556	0.6	200
3	200	1.0	200
4	89	1.5	200
5	50	2.0	200
6	22	3.0	200

Figure 2a presents the time development of several quantities for case 3 of the run set A. From top left to bottom right within each figure, we show

   (i) the outer (solid) and inner (dashed) radii;

  (ii) the feed current I_a (dashed) and the load current I_b (solid);

 (iii) the K-shell (solid) and total (dashed) radiation pulse;

  (iv) the electron temperature T_e;

   (v) the mean charge state of the plasma $<Z>$;

(vi) the total (solid) and radiated (dashed) energy in the pinch. Likewise, Fig. 2b presents the time development for case 3 of run set B, and Fig. 2c presents the time development for case 3 of run set C.

Figure 3a presents the total (filled circles) and K-shell (circles) yields derived from the numerical simulations for the six cases of table II in run set A as a function of the initial outer radius R(0). For comparison, we also display the total (filled triangles) and K-shell (triangles) yields measured on the Double Eagle experiments. Likewise, Fig. 3b presents the yields from run set B, and Fig. 3c presents the yields from run set C. Again the same experimental data is shown in each figure.

We first note that the implosion times from the simulations range from 85 to 95 nanoseconds which agree with the experimental values to within ~ 5 nanoseconds. In the experiment the initial time is measured by extrapolating the linear portion of the current rise back to I = 0. The time of pinch assembly on axis is denoted by the appearance of the K-shell pulse. The difference between these two fiducial times is the implosion time. This procedure is indicated in Fig. 2a. This agreement indicates that most of the mass in the wire arrays must participate in the implosion, otherwise the experimental implosion time would be significantly shorter than the simulation results.

Figures 2a and 3a indicate several features of the set A simulation runs which are in disagreement with the experiment. First from Fig. 2a, the minimum pinch radius of the simulation is much smaller than the observed pinch radius, which is about 0.1 cm. Second, also from Fig. 2a, the K-shell pulse width is < 1 nanosecond, while the observed pulse width is on the order of 10 nanoseconds. And third from Fig. 3a, the total and K-shell yields are significantly larger than the observed values. Instead of

collapsing to a pinched configuration of one tenth the initial radius for ~ 10 nanoseconds as in the experiments, the simulation models execute a semi-periodic bouncing at ~ 0.01 cm with K-shell radiation emerging at least during the first bounce. The long term state is a ~ hundred nanosecond long Bennett equilibrium radiating in the L-shell of aluminum. This is the theoretical radiative collapse phase. We note these features are characteristic of 1-D simulation radiation-hydrodynamic multi-zone codes, and are not a peculiarity of our computationaly faster one zone modeling.

The discrepancy in total radiated energy suggests that more energy is coupled to the pinch load in the simulations than in the actual experiment. In order to reduce the amount of coupled energy we supposed that a short circuit is triggered in the feed once the load voltage exceeds a certain value. Since the implosion time occurs before the time of peak machine current, a short in the feed located upstream of the load would effectively limit the energy reaching the load by reducing the load current. Run set B contains the simulations with a short, but again with Spitzer resistivity. The results are displayed in Figs. 2b and 3b. From Fig. 2b we note that the current upstream of the short, where the current monitor is placed in the experiment, continues to rise after implosion of the pinch. The current in the load, however, drops from 3 to 0.5 MAmps at implosion. The total and K-shell yields of the set B runs are, as suspected, smaller than the yields without a short. (Compare Fig. 3b for set B with Fig. 3a for set A.) As a matter of fact, both the total and K-shell yields are on the order of the experimental values for set B runs with a short. This result does not appear to be very sensitive to changes in the parameters which characterize the short, namely, the load voltage which triggers the short, the splitting of the feed inductance, and the variation of the short resistance R_s. The existence of the short circuit could be checked by using several current monitors over the length of the feed and looking for current profiles like those of Fig. 2b. From Fig. 2b one sees, however, that

the pinch radius is still much smaller than the observed 0.1 - 0.2 cm and the K-shell pulse length is still much shorter than the observed ~ 10 nanoseconds.

Clearly some physical mechanism not considered in the simulations appears to cause a rapid thermalization and a hydrodynamic bounce at ~ 0.1 cm, which is much larger than the bounce radius found in the simulations. Within the context of a 1-D simulation code we can mimic the effects of a rapid thermalization by considering a phenomenologically enhanced resistivity according to eqn.(*). Let us estimate the value of the parameter β in this model equation by comparing the classical resistive heating rate with the observed mean K-shell power. The latter quantity is

$$\bar{P}_{rad} \text{ (K-shell)} \sim \frac{30 \text{ kJ}}{10 \text{ nsec}} = 3 \times 10^{11} \text{ W}$$

From the observed pinch radius (0.1 cm) and peak current (3 MA), assuming the Bennett temperature and Spitzer resistivity, one finds

$$\eta_{Spitzer}(T_{Bennett}^{-3/2}) \left(\frac{I}{\pi R^2}\right)^2 \pi R^2 \Delta z$$

$$\sim 6 \times 10^4 \langle Z \rangle (1+\langle Z \rangle)^{3/2} \ln\Lambda \frac{\left(N_{line}/10^{18} \text{cm}^2\right)^{3/2}}{(I/MA)} \frac{(\Delta z/cm)}{\pi(R/cm)^2} \sim 5 \times 10^9 \text{ W}.$$

Thus the classical heating rate is nearly two orders of magnitude <u>smaller</u> than the K-shell radiated power. Hence we considered the effect in run set C of an arbitrarily enhanced resistivity according to eqn.(*) with $\beta = 100$. The results, displayed in Figs. 2c and 3c, do succeed in limiting the pinch radius to ~ 0.1 cm at least on the first bounce, producing broader K-shell pulse widths (~ 5 nanoseconds) compared to previous runs, and predicting total yields in better agreement with the experimental values than the

previous runs. However, the K-shell yields have increased from run set B to about three times the measured values at R(0) = 1.0 cm.

The general improvement in the comparison of simulation results with experimental values provided by the enhanced resistivity of eqn.(*) is encouraging for developing a predictive capability. This enhanced resistivity effectively prevents the radiative collapse observed in previous simulations by continually diffusing the magnetic field into the plasma and increasing the resistive heating. The actual physical mechanism behind the phenomenological resistivity cannot be ascertained from the present 1-D model. The enhancement may arise from convective or sausage instabilities in the plasma shell during the run in phase. The form of the enhancement factor in eqn.(*) is of course not unique. If instead of eqn.(*) we use the following expression for the enhanced resistivity

$$\eta = \eta_{Spitzer} \times \left[1 + \min\left(e^{t(nsec)/25} - 1 \,,\, 100 \right) \right] \,, \qquad (**)$$

we find nearly identical results to those of run set C. This suggests that, if instabilities are responsible for the enhanced resistivity, their growth rate should be on the order of 25 nanoseconds. To pursue the problem of understanding the limitations to radiative collapse in a Z-pinch one must investigate the implosion and radiative dynamics with a multi-dimensional simulation code.
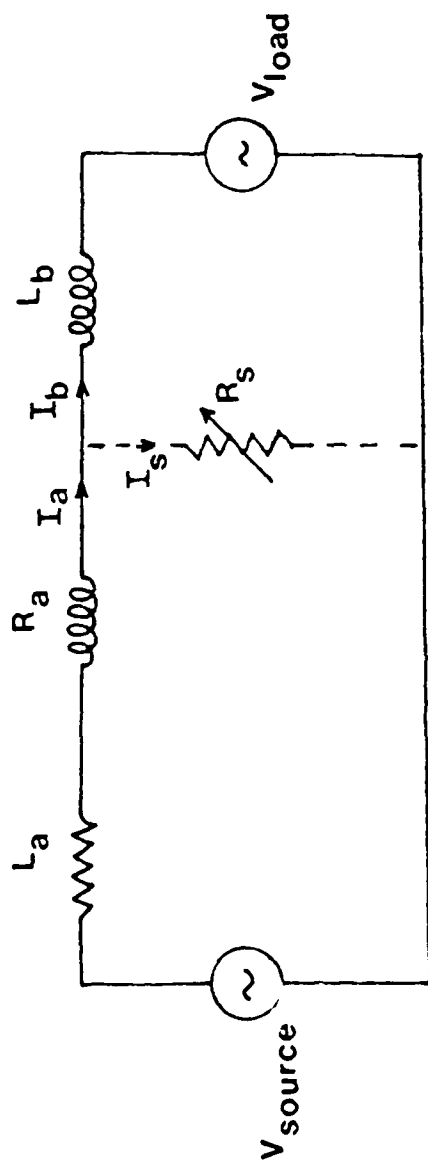
Fig.1

Figure 2a

60

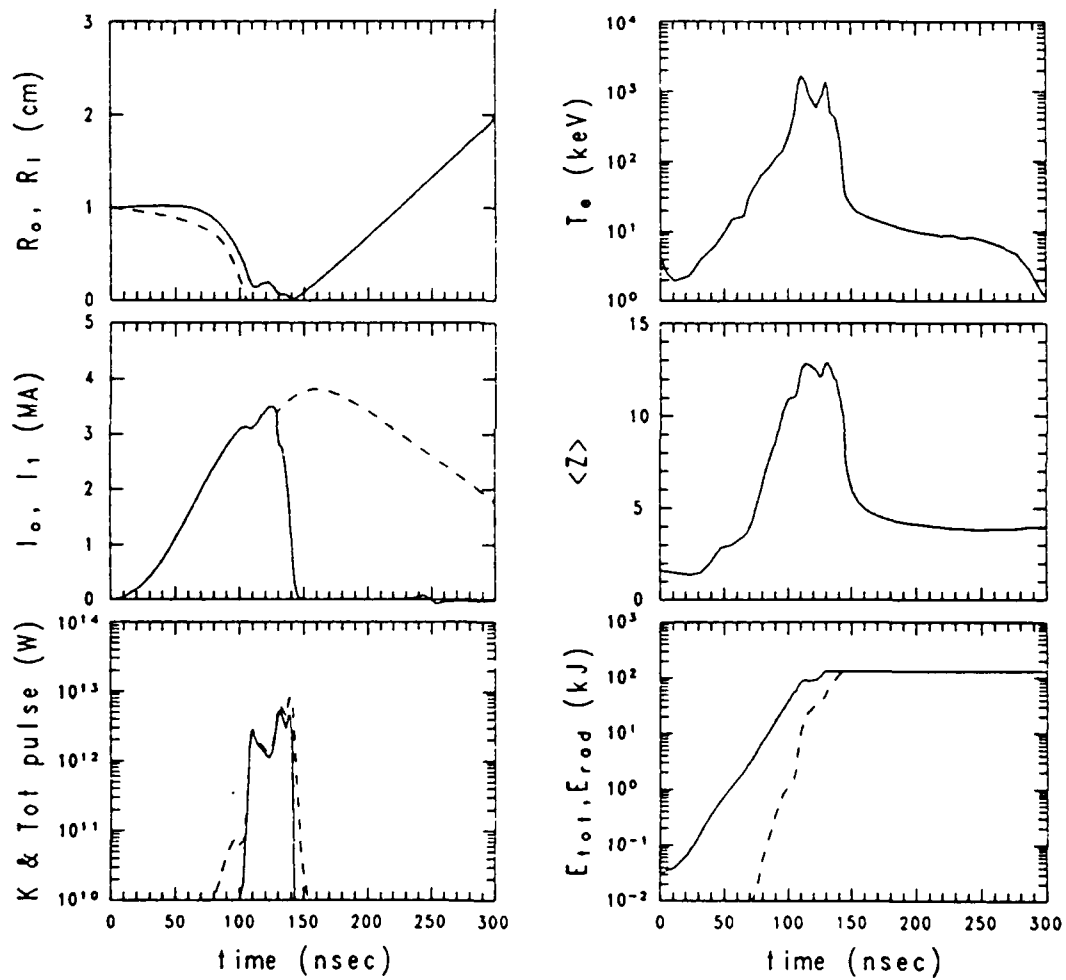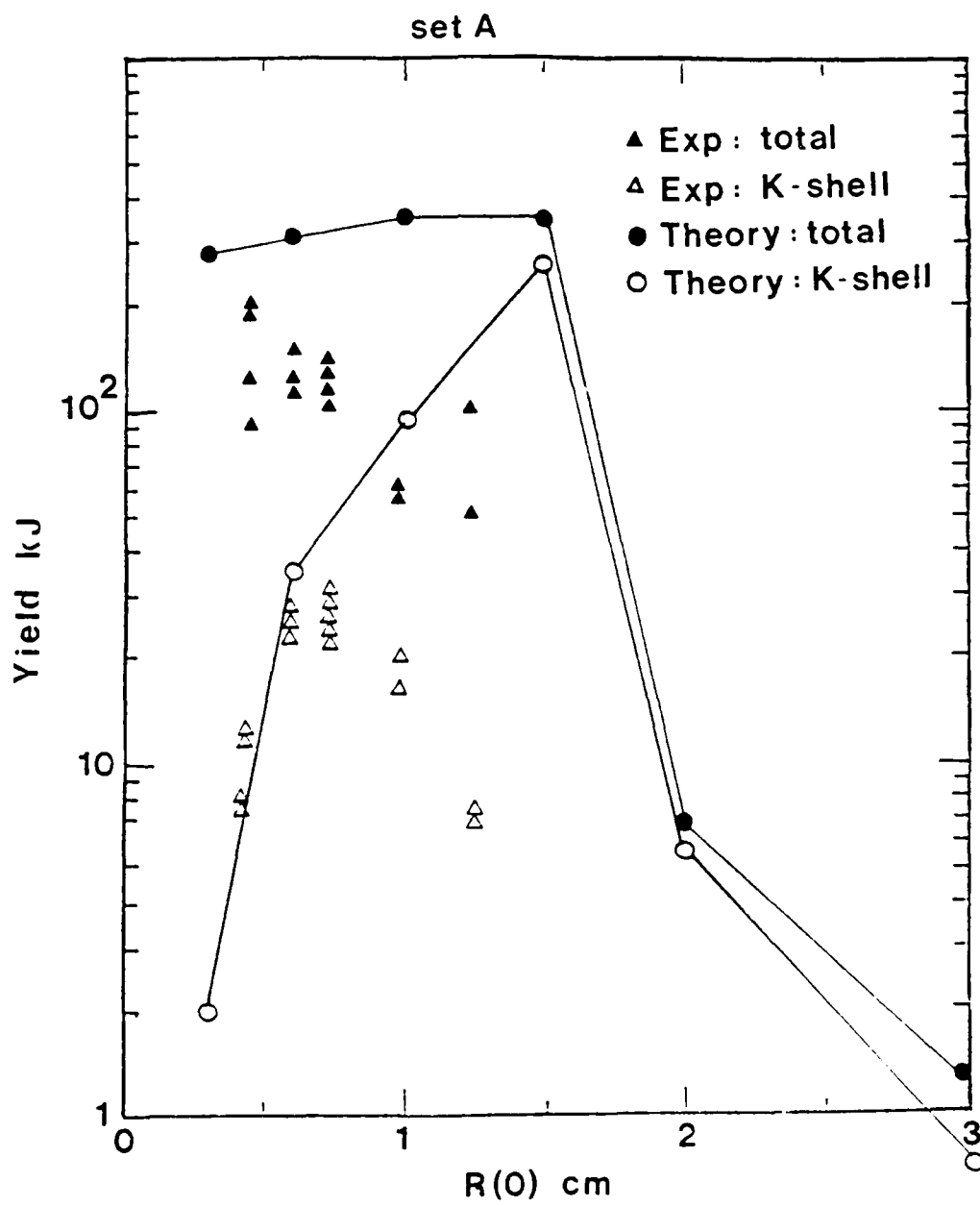| BOX	MACHINE	ATMWGT	ROUTO	RINO	DZ	RWALL	MASS	MASS*ROUTO²	VSHRT	BETA
2	DOUBLE EAGLE	26.98	1.00	1.00	2.00	1.30	200.0	200.0	3.0	1.

Figure 2b

Figure 2c

set A

Figure 3a

set B

Figure 3b

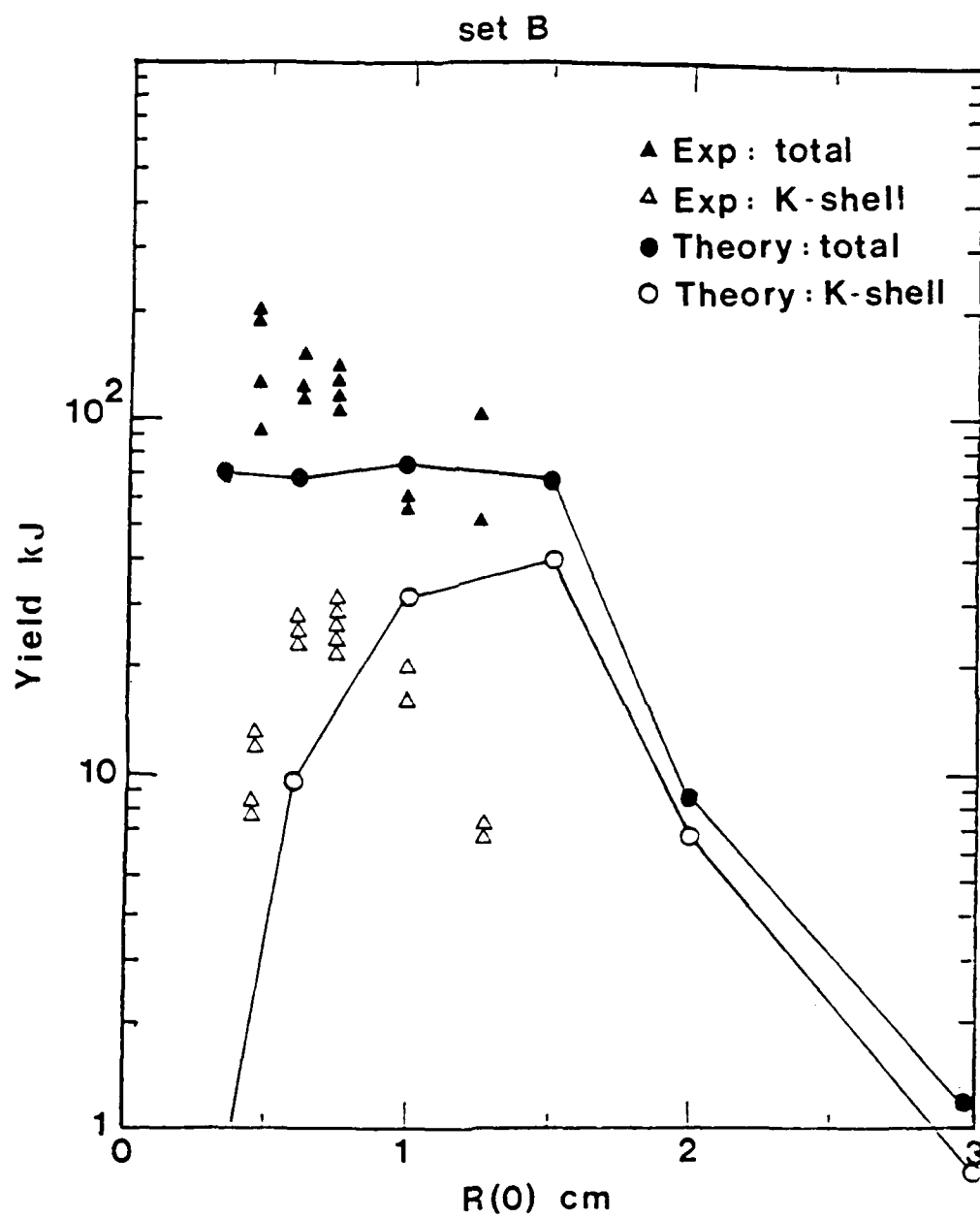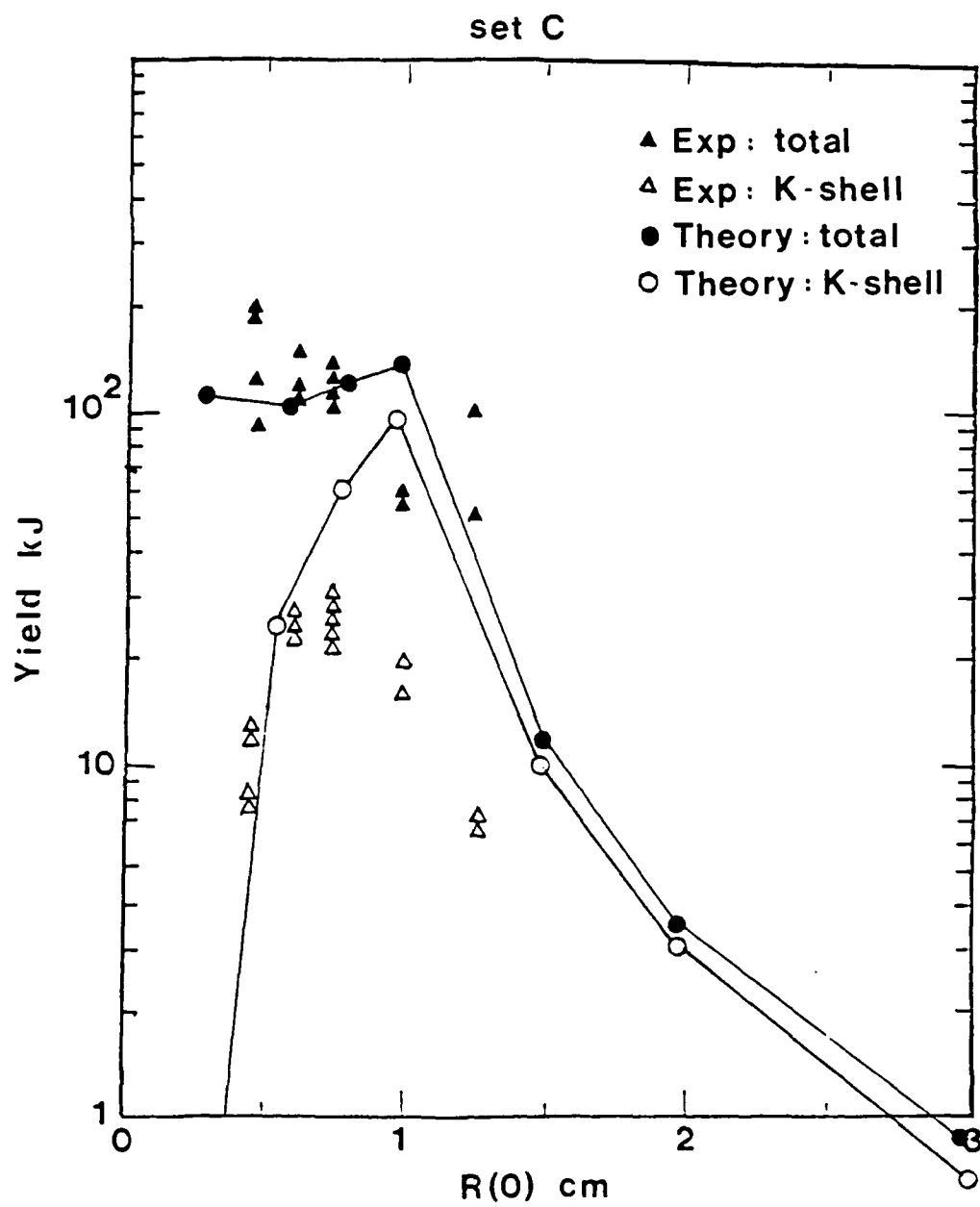set C

Figure 3c

Exploiting Radiative Collapse in a PRS

Radiative collapse has been discussed at some length[7-10] and, while the phenomenon has not been observed to date, the concept has an attractive simplicity when considered alonside the complex technological requirements of imploding PRS load schemes. A PRS made to exhibit radiative collapse would probably consist of several parallel cryogenic fiber sources, made either of pure, moderate Z frozen gases (Ne,Ar), or of high Z seeded hydrogen fibers. The parallel connection would requre vacuum convolutes similar to those contemplated for Reflex Triode bremmstrahlung sources, and could be driven directly (on μs quarter cycle timescales) by fast capacitor banks like those used in the Falcon or FastCap decade machine designs.

In view of the conjectural aspect of the whole "radiative collapse" scenario, a detailed machine or even front end design would be premature, but one can fruitfully examine the source dynamics with simple models in order to crystalize more fully the various tradeoffs involved. We will do this here for two cases. The first is a "classical" radiative collapse at the Pease-Braginskii current; the second, a screwpinch variant on the scheme which allows one to select the critical current level, or at least vary it about the Pease-Braginskii value.

To date we have mapped out only the essential features of these schemes, but, whenever more concrete experimental verification of the phenomenon is available, the model will readily allow investigations into the mutual interaction of such parallel loads in a decade machine environment, or the expected radiation pulse history, spectrum and yield.

Essential features of a classical radiative collapse

The refrigeration is driven by a competition between ohmic heating and radiative cooling in a Bennett equilibrium. For such an equilibrium pinch large current forces a density large enough to cool the plasma quickly. When the current in the pinch exceeds I_{pb}, then

$$\frac{\dot{a}}{a} = \frac{(P_h - P_r)}{I^2} = \frac{3}{4t_r}\left[(\frac{I_{pb}}{I})^2 - 1\right] \; ,$$

predicts a rapid contraction of the pinch. It is this result which implies the use of multiple, isolated loads in parallel, since the pinch current will not significantly exceed the Pease-Braginskii current ($\approx 1.5\ MA$) and the energy sources will provide tens of megamperes.

A more delicate constraint has been pointed out by Robson[11]. The load must accept energy for a sufficiently long time, viz. a collapse time (t_c) $\approx$ several radiation cooling times (t_r). A density- collapse time product then arises

$$n_o t_c = 1.42 \cdot 10^{13}\ \frac{\sqrt{T}}{1 - (\frac{I_{pb}}{I})^2} \; .$$

Whereupon the use of a high initial density is required, since the collapse time must be short enough to be compatible with pulse power sources. Here the temperature T is also deremined by the current through the Bennett condition.

In the laboratory, what conditions might help obtain radiative collapse? Frozen H_2 fiber pinches are observed to be stable so long as the Poynting flux is inward. Typical stable domains are 300 ns to 0.5 MA. An "inductive notch" during the compression will therefore not cause disruption until the voltage has reversed after stagnation. Since the pinch and its immediate inductance are a final energy store

very close to the load, the use of relatively slow driver timescales ($\approx 1 \to 2$ μs) allows an easier energy transfer to this inductive store. The spontaneous collapse, when it occurs (at $I > I_{pb}$), would allow a nearly complete conversion of this nearby magnetic energy to radiation.

What's a favorable machine configuration for obtaining these conditions? A load of this sort would need no opening switch, since the pinch timescales favor a direct drive. The quarter cycle time (≈ 1 μs) for a Falcon or FastCap bank is right in a useful window for this load.

Parallel loads convoluted at the usual radius of the ring diode in bremsstrahlung mode offer the best energy coupling. The overall impedance of the array can remain $\approx 0.10\Omega$ or less even when collapsed to very small radius. Moreover, the individual load modules tend to be self correcting in collapse time because increased motional impedance in one holds the current down while others catch up. These considerations lead to the conceptual design shown in Figure 2.

Fig. 2 A Generic Design

Circuit Element Model for a Bennett PRS

A quasi-equilibrium model for the radial motion is summarized by

$$\frac{\dot{a}}{a} = 10^7 Z_\Omega \left[1 - (\frac{I}{I_{pb}})^2 \right] - \frac{3}{2} \frac{\dot{I}}{I} \,,$$

$$I_{pb} = 433 \left(\frac{\Lambda}{f} \right)^{\frac{1}{2}} \frac{1 + Z}{2Z} \,,$$
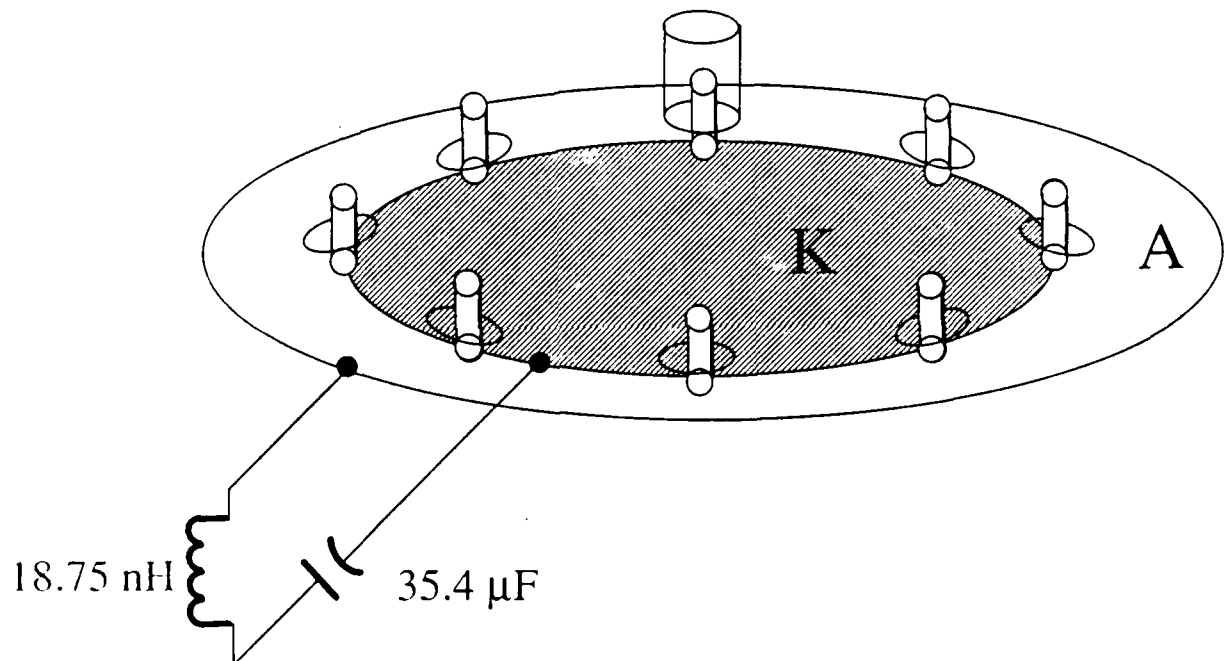
A Generic Design

18.75 nH   35.4 μF

Figure 2

$$f = \frac{1}{\left[(\frac{P_{br}}{P_{bh}})^{0.56} + 1 \right]^{\frac{1}{0.56}}} \ .$$

In our generic design the single module inductance and impedance are given by

$$L = 1.8 \cdot 10^{21} l_p / c^2 \ \ln \frac{r_w}{a} \ [nH] \ ,$$

$$Z = Z_o - \frac{\dot{a}}{a} \ 1.8 \cdot 10^{12} l_p / c^2 \ [\Omega] \ ,$$

and

$$Z_o = 1.109 \cdot 10^9 l_p (\frac{\Lambda}{10}) \frac{\mu^{\frac{3}{2}}}{a^2 I^3} \ [\Omega] \ .$$

What results can be expected in such a radiative collapse? Consider as "middle of the range" test case a 40 μm diameter fiber, driven by a 1.1 μF water capacitor, with a 600 ns quarter cycle time. The initial store energy is 309 kJ and the initial pinch line density is $7.54 \cdot 10^{17}$ ions/cm^3, the resulting evolution is shown in Figure 3(a).

Fig. 3a Radiative Collapse of a Model Fiber Load

The radiated energy per module is decomposed into three classes; we find the yields to be (i) total radiation: 146 kJ, (ii) radiation ≥ 5 keV: 26 kJ, and (iii) radiation ≥ 10 keV: 5 kJ, respectively. The radiation power development is shown in Figure 3(b). Hence between ten to fifteen such modules would be a reasonable array from the standpoint of power flow.

Fig. 3b Radiated Power in Three Channels
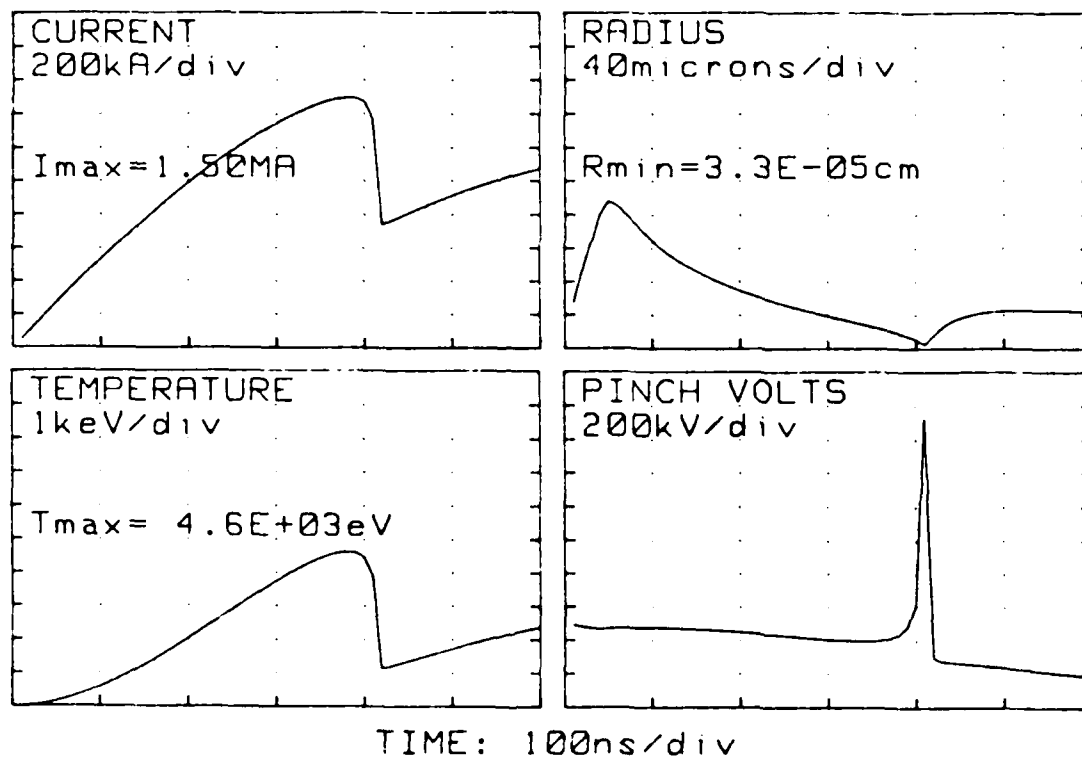
B. Modifications when axial fields are included

CURRENT
200kA/div

Imax=1.50MA

RADIUS
40microns/div

Rmin=3.3E-05cm

TEMPERATURE
1keV/div

Tmax= 4.6E+03eV
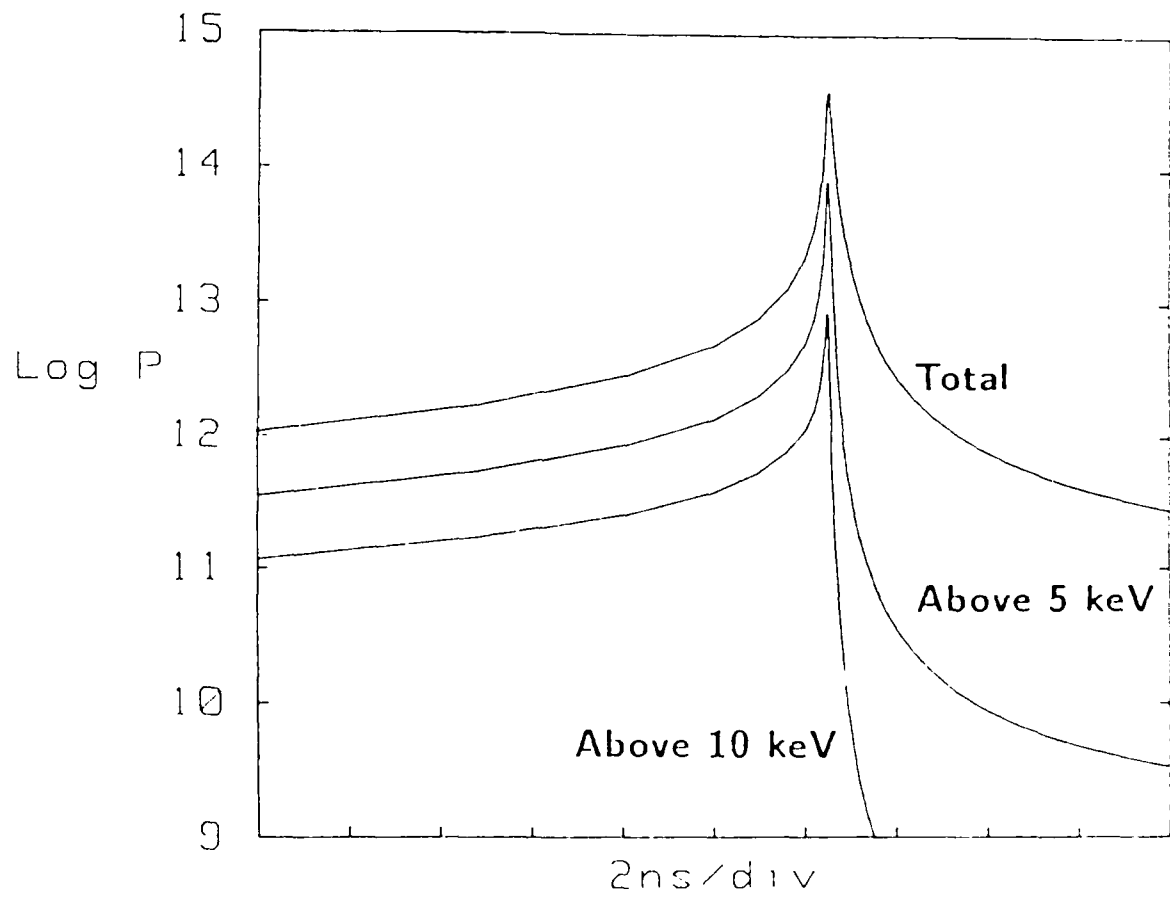
PINCH VOLTS
200kV/div

TIME: 100ns/div

Figure 3(a)

Figure 3(b)

The use of an axial field component can perhaps allow some control over the onset of this spontaneous collapse, as well as the gross stability of the PRS. An arbitrary mix of exterior and interior axial field strengths is allowed, again using the self- similar model. The mix can be adjusted by twisting the return current path to N_{wind} per cm, so that

$$\delta_1 \propto (IN_{wind}/I_{Bennett})^2 \; , \; \delta_2 \approx const. \; .$$

Circuit Element Model for the Screw Pinch PRS

The momentum equation is

$$\dot{U}(\alpha) = r_o\Big(\frac{2\nu_S^2}{\alpha} + \frac{\nu_{B_z}^2}{\alpha^3} - \frac{\nu_{B_\theta}^2}{\alpha}\Big)$$

with $\alpha = r(\tau)/r_o$, $\Theta_e = T_e + (\frac{2}{3})\frac{\epsilon_I}{Z}$, so that $T_e = \Theta_e/B(\Theta_e)$ and:

$$\nu_s = \sqrt{(Z+1)T(\Theta_e)/m_{ion}r_o^2} \; ,$$

$$\nu_{b_z}^2 = \nu_{\delta_2}^2 - \Big(\frac{\pi N I(\tau)}{c\sqrt{\Upsilon}}\Big)^2 \; , \; \nu_{b_\theta} = \frac{I(\tau)}{a_o^2\sqrt{\pi c^2 m_{ion}n_o}} \; .$$

If one neglects ohmic heating, radiation and ionization, viz. $B(\Theta_e \to 1$, the implied adiabatic heating would replace $\frac{2\nu_S^2(\Theta_e)}{\alpha} \to \frac{2\nu_{S,o}^2}{\alpha^{7/3}}$ in the momentum equation.

The energy equation becomes

$$\dot{\Theta}_e = -(4/3)T(\Theta_e)(\frac{\dot{\alpha}}{\alpha}) + \Omega_o(I/\alpha)^2 - P_{rad}(\alpha,\Theta_e)$$

with a radiation model given by

$$P_{r\iota}(\alpha,\Theta_e) = Min\Big[\frac{P_{CRE}(\Theta_e)}{\alpha^2}, G(\Theta_e)P_{bb,o}\Big(\frac{\alpha T^4(\Theta_e)}{1+Z(\Theta_e)}\Big)\Big] \; .$$

here the "grayness" is modeled by $G(\Theta_e) = P_{CRE}/P_{bb}$ at the constant density used to calculate the CRE emission power and equation of state. The inductance and impedance now include the return current windings explicitly

$$L = 1.8 \cdot 10^{21} l_p/c^2 \ (\ln \frac{r_w}{r} + \frac{1}{2}(\ r_w^2 - r^2)[2\pi N]^2)\ [nH]\ ,$$

$$Z = \Omega_p - (\frac{\dot{r}}{r} + [2\pi N]^2 \dot{r} r)\ 1.8 \cdot 10^{12} l_p/c^2\ [\Omega]\ ,$$

$$\Omega_p = 3.257 \cdot 10^{-6}(l_p/\pi r_o^2)(\frac{\Lambda}{10})\frac{\mathcal{Z}(\Theta_e)}{\alpha^2 T_e^{\frac{3}{2}}(\Theta_e)}\ [\Omega]\ .$$

When the implosion is adiabatic an effective potential determines the turning points

$$\mathcal{V}(\alpha) = \nu_{B_\mu}^2(I/I_B)\ \ln \alpha^2 + \frac{3}{2}\nu_S^2\ (\frac{1}{\alpha^{4/3}} - 1) + \nu_{B_z}^2(N,I/I_B)\ (\frac{1}{\alpha^2} - 1)$$

The kinetic energy of the pinch is then

$$T^2(\alpha) = T_o^2 - \mathcal{V}(\alpha)\ .$$

Because of the $1/\alpha^3$ scaling of axial field stress the interior turning points persist until larger I/I_B, N_{wind}, or T_o^2 values can erase the dip in $T(\alpha)$, as shown in Figures 4(a,b,c). The extinction of the adiabatic turning points with larger N_{wind} is shown in Figure 5. A critical value of $N_{wind} \approx 0.08$ is obtained beyond which no rebound is possible – the load is forced to a singular compression.

When Ohmic heating is included, along with "gray" radiation, the critical value of N_{wind} increases substantially, but the hole is still there. A scan of N_{wind} from $0.0 \rightarrow 1$ is enough to show the effect. For $N_{wind} \approx 1$, $\ddot{\alpha}$ is ever more negative for $\alpha < 0.749$, even though Θ_e remains positive as the load collapses. For $N_{wind} \approx 0$, $\ddot{\alpha}$ is ever more positive and the first turning point occurs for $\alpha = 0.727$. On or above $N_{wind} \approx 0.8$, a radiative collapse is unavoidable.
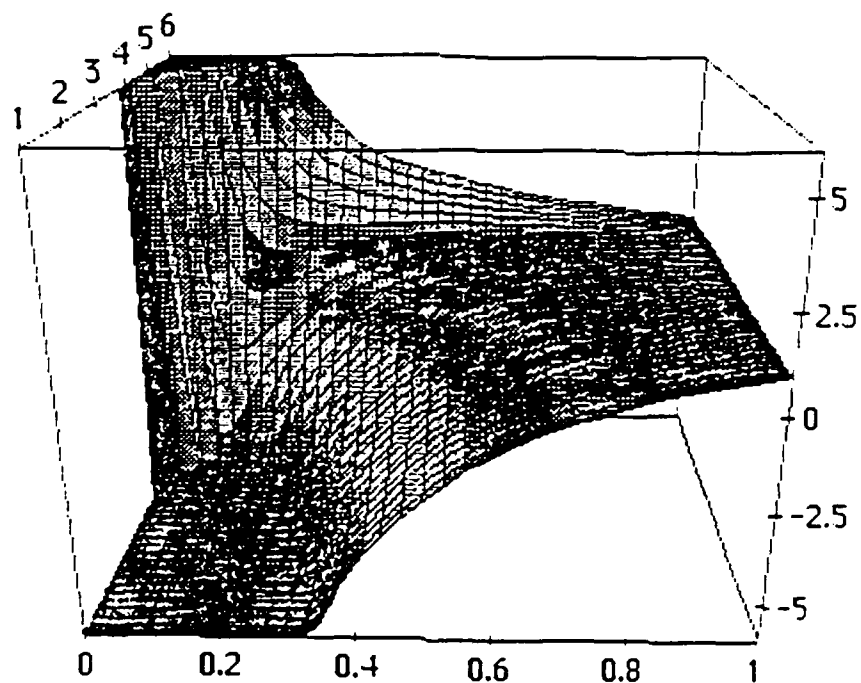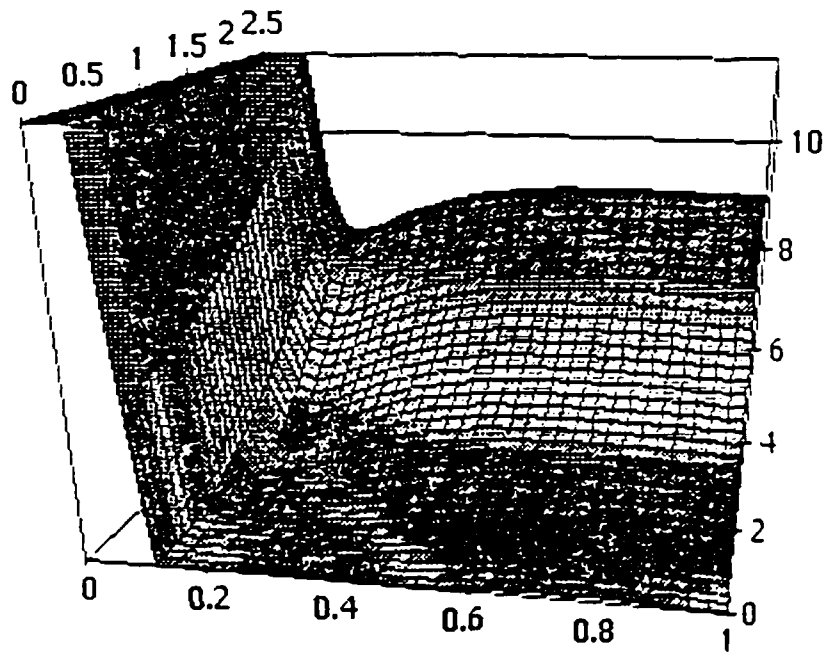
Adiabatic Potential for Initial Kinetic Energy. to=1.0 . Nwnd= 0.125
Variable l./lb = [1.0, 6.0]
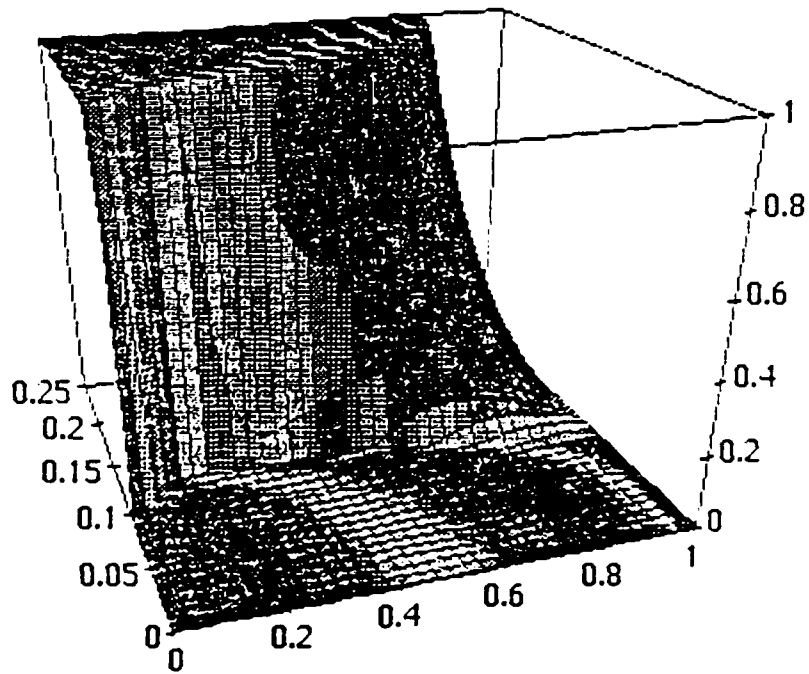
Adiabatic Potential for Initial Kinetic Energy, to=.10 . l/lb = 1.0
Variable Nwind=[0. 0 . 0.25]

Adiabatic Potential for Nωnd=0.125. l/lb = 1.0
Variable Initial Kinetic Energy. to=[0 .0 . 2.5]

TURNING POINTS AS A FUNCTION OF WINDING NUMBER PER UNIT LENGTH
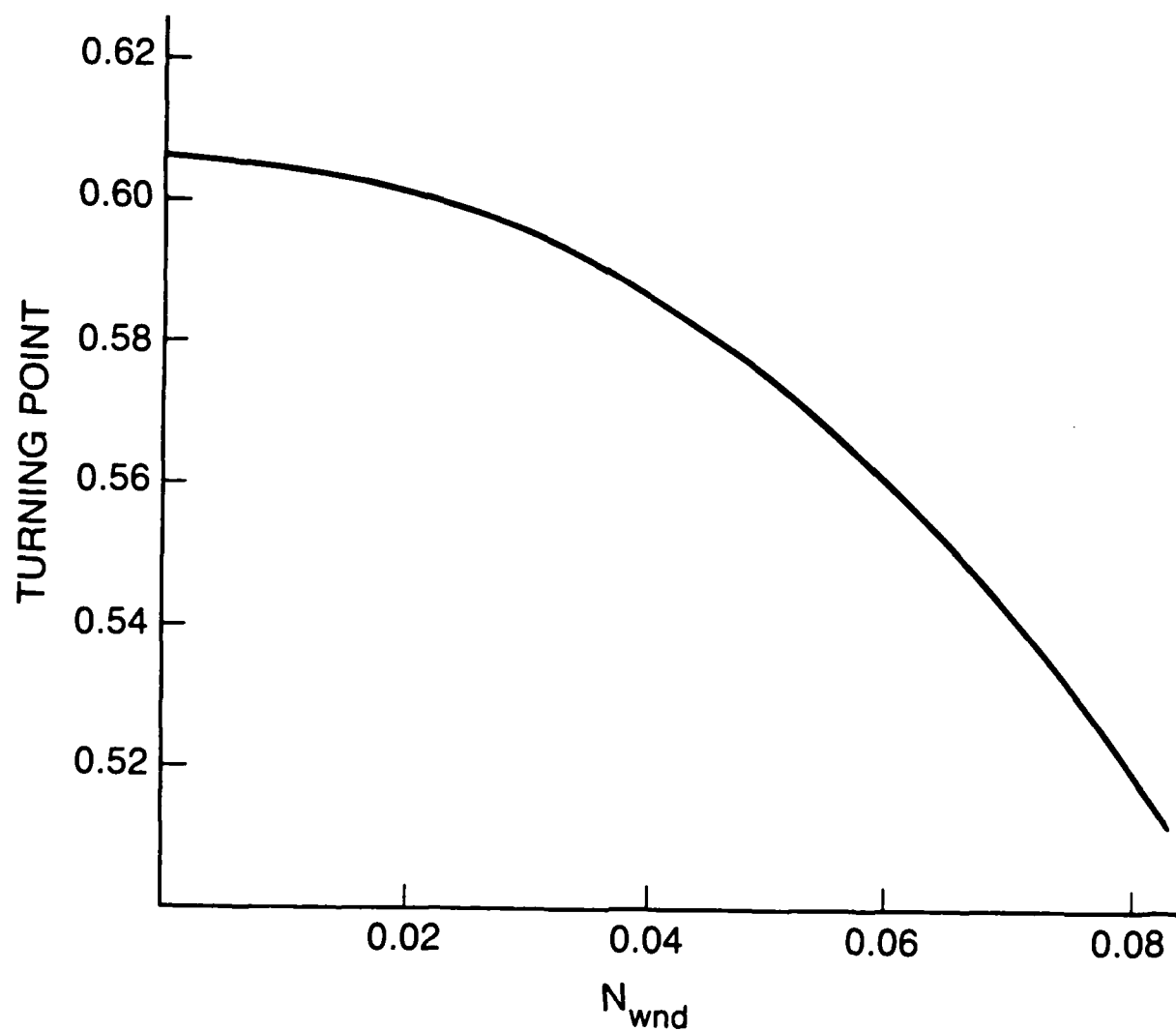

Figure 5

Conclusions

Many inductive store concepts separate fuse, switch and load; others make the load and switch one unit. In the sense discussed here, because of the critical trigger current for collapse, the fuse can be made the load. The Pease-Braginskii current is only one limit on the current per load module and this natural trigger value for highly efficient energy conversion is perhaps tunable with axial field components. Such a PRS device allows one to charge the final inductive store on bank quarter cycle timescales and recover the energy quickly in only one stage of power amplification. A direct drive and parallel load modules offer a ready compatibility and a straightforward development path with presently conceived decade machine designs. High energy ($h\nu \geq 10$ keV) yields on the order of 5 kJ per load module could be realized.

References

7. A.E. Robson. Nucl. Fus. **28**(12), 1988, p.2171.

8. W. Thornhill, J.L. Giulliani, J. Davis, NRL Memo Rep. 6500, 1989, "The Dense Z-Pinch as a Plasma Radiation Source"

9. M.G. Haines, Plasma Physics and Contr. Fus. **31**(5), 1989, p.759.

10. A.E. Robson, "Anomalous Resistivity and the Pease-Braginskii Current in a Z-Pinch", private communication.

11. A.E. Robson, PFB **1**(9), 1989, p.1834.

IV. PRS Optimization: Electron and Field Dynamics in the z-pinch

Introduction and Review

Energetic electrons can be very influential in the dynamics of a z-pinch implosion as well as in the radiation generated by the pinch, yet this influence has not been investigated in any depth to date. Distortions of the electron distribution function from a Maxwellian shape will change transport coefficients (e.g., conductivity) and alter rates of radiation mediated by electron-ion collisions. Beams of electron runaways such as have been observed seem to be connected with the "bright spots" from which a large part of the pinch K-shell radiation typically emerges. Bremsstrahlung from energetic electron beams can also be a significant source of hard x-rays. With increased machine power, these effects could be even more significant and their understanding more important.

The goal of this study is to understand the role of energetic electrons in a z-pinch implosion. In earlier work, the Fokker-Planck equation was analyzed to determine factors significantly affecting the electron distribution function. A one-dimensional numerical solution of the Fokker-Planck equation was developed and used as a diagnostic of one-dimensional MHD z-pinch simulations. From this, estimates of the high-energy electron population and degree of anisotropy were obtained at all times in the simulated implosions.

Three factors affecting the electron distribution function were studied: ohmic heating, charge-conserving inelatic collisions, and compression. Ohmic heating was found to be the most important in changing the shape of the distribution. The inelastic collisions studied were generally negligible, and compressional heating was largely isotropic, even when of significant magnitude (as at stagnation), and had the principal effect of accentuating

ohmically-produced anisotropies.

Ohmic heating causes an enhancement of the distribution function focused at the electron energy

$$\epsilon_{max} = \left[\frac{2\nu_{ei}^2}{\omega_c^2}\right]^{1/3} \frac{3}{2}kT.$$

where ν_{ei} is the thermal electron-ion collision frequency, and ω_c is the electron cyclotron frequency. The magnetic field determines the character of the heating: for low magnetic fields $\omega_c < 2\nu_{ei}$, the superthermal tail is enhanced, while for higher fields, the tail is depleted. The magnitude of heating is determined by the electric field: with a zero magnetic field, significant numbers of runaways are generated by the Dreicer field

$$E_D = \frac{1}{e}\nu_{ee}\sqrt{3mkT},$$

where e and m are the electron charge and mass, and ν_{ee} is the thermal electron-electron collision frequency. With a magnetic field, a higher electric field is needed to produce energetic electrons, and the electrons generated are more isotropic and less like classical "runaways". A strong magnetic field (as defined above) effectively shuts off runaway production and focuses the system's energy on the well-confined bulk of the distribution.

A system that generates a significant number of energetic electrons, then, must experience a large electric field $E > E_D$ while the magnetic field is still relatively small ($\omega_c < 2\nu_{ei}$). A burst of directional electrons should result, which can be amplified by compressional heating, should it occur at that time. Energetic electrons are rapidly confined by a large magnetic field, and high electric fields cannot overcome this effect.

Only a small runaway electron population was predicted from the z-pinch implosion model used for diagnostics. In particular, the electron population at stagnation, while non-

Maxwellian, was found to be highly isotropic. This is not in accord with experiment, where bursts of electrons have been seen at stagnation. The reason for the discrepancy is believed to be incomplete knowledge of the radial distribution of the electric and magnetic field strengths inside the pinch. Small changes in the model field distributions could significantly affect the predicted runaway populations. There is little experimental information about pinch field strengths, which depend strongly on the way the pinch current is carried. A number of different theoretical models of pinch current exist, and there have been some interesting numerical results in the related topic of plasma opening switches that suggest that magnetic field diffusion is much faster than a Spitzer-based fluid theory would predict. With plasma opening switches, initial conditions are very important in determining the evolution of the system.

Plasma opening switches utilize much lower densities than the z-pinch, especially from an exploding wire. The parametrizing study of the pinch corona presented here is a first step in studying the factors determining current and field distributions in an imploding z-pinch.

The coronal current channel in an exploding-wire z-pinch

The corona formed outside an exploding wire plays, at least initially, an important role in current conduction and pinch dynamics. Because of its high conductivity, the pinch medium tends to exclude magnetic field and current. In the corona, however, turbulence will limit the conductivity and an anomolous resistivity will allow rapid field and current penetration. The low density of the corona limits radiative losses and allows high temperatures to be attained which paradoxically enhance the conductivity. So the corona

can carry a large fraction of the pinch current while also maintaining a quite different configuration of electric and magnetic fields from the pinch core.

In addition to its implications for electron energy transport and radiation, the corona potentially has a significant effect on the overally pinch dynamics, since it acts as a competing current channel to the core and heats the core by energetic electron collisions. These effects are incorportated into most pinch models by adding a thin skin current layer to the current channel.

To study the behavior of the corona under various pinch conditions, parameters from a 1D MHD z-pinch model were used to determine the dynamical evolution of the corona extent, density and temperature. The parameters used were appropriate for a titanium wire implosion. The simplest case is examined: a corona where limited conductivity permits field penetration and large currents. Low densities minimize radiative losses, and very high temperatures and currents result. Initial theoretical work on this problem was performed by D.A. Tidman.

Z-pinch model:

The system is considered to be cylindrically symmetric with spatial uniformity in the z direction. The ion atomic mass number is A, and degree of ionization is Z. Corona parameters are:

a = Corona inner radius/core outer radius

I_1 = Core current (amp) I_2 = Corona current (amp)

kT_1 = Core temperature (eV) kT_2 = Corona temperature (eV)

83

The corona is distinguished from the core by having a limited conductivity, such that:

$$j = ec_s n_e$$

where n_e is the electron number density, and c_s is the ion acoustic sound speed:

$$c_s = 9.788 \times 10^5 \sqrt{ZkT_2/A} < v_{th}$$

The core dynamics are determined by MHD model (with Spitzer resistivity and line radiation). Pinch is divided into 30 uniform annular cells, numbered from the inside out. Outside the outermost cell is the isothermal corona.

Fluid Equations:

The complete fluid equations are listed here for reference. These are approximated for the corona considered here by neglecting the right-hand side of each equation. The assumption is that the corona is quasi-static, following the motion of the core, and that it is in Bennet equilibrium. This is just the simplest assumption for a first look at the problem.

$$\frac{1}{c}\vec{j} \times \vec{B} - \vec{\nabla} \cdot P = \rho\frac{\partial \vec{V}}{\partial t} + \rho\left(\vec{V}\cdot\vec{\nabla}\right)\vec{V} + ne\vec{E} - \rho\frac{\partial V}{\partial t}\bigg|_{coll}$$

$$\vec{\nabla} \times \vec{B} - \frac{4\pi}{c}\vec{j} = \frac{1}{c}\frac{\partial \vec{E}}{\partial t}$$

$$\frac{\partial}{\partial t}\left(\frac{3}{2}nkT\right) = \vec{E}\cdot\vec{j} - \vec{\nabla}\cdot\vec{q} - \frac{\partial}{\partial t}\left(\frac{1}{2}nmV^2\right) + \frac{\partial}{\partial t}\left(\frac{1}{2}nmV^2\right)\bigg|_{coll}$$

Quasi-Static Corona:

The equations actually satisfied by the corona are:

$$-\frac{1}{c}jB = kT_2\frac{\partial n}{\partial r}$$

$$\frac{c}{4\pi}\frac{1}{r}\frac{\partial}{\partial r}(rB) = j$$

These can be solved analytically. The marginal-current approximation relates j and n, so that one equation for (rB) can be obtained:

$$\frac{1}{4\pi} \frac{1}{r^2} \frac{\partial}{\partial r} \left(\frac{r^2 B^2}{2} \right) = -\frac{ckT_2}{4\pi e c_s} \frac{\partial}{\partial r} \left[\frac{1}{r} \frac{\partial}{\partial r} (rB) \right]$$

The first integration of this expression (from a to r) gives an equation for $y \equiv rB$:

$$r \frac{\partial y}{\partial r} = 2y - \alpha y^2 + \beta$$

The second integration gives an expression for $y(r)$:

$$y = \frac{y_2 + (r/r_0)^{2\delta} y_1}{1 + (r/r_0)^{2\delta}}$$

where

$$y_{1,2} = \frac{1}{\alpha} (1 \pm \sqrt{1 - \beta\alpha})$$

$$\delta = \sqrt{1 + \beta\alpha}$$

and

$$\alpha = \frac{ec_s}{2ckT_2} = 4.894 \times 10^{-3} \sqrt{\frac{Z}{AT_2}}$$

$$\beta = \alpha y_0^2 - 2y_0 + ay_0'$$

$$= 1.958 \times 10^{-4} I_1^2 \sqrt{\frac{Z}{AT_2}} - 0.4I_1 + 1.971 \times 10^{-13} a^2 n_0 \sqrt{\frac{ZT_2}{A}}$$

This expression for $y(r)$ is plotted in fig. (1), and the corresponding magnetic field is shown in fig. (2). These figures show the shape of the quantities only, which remains the same for any values of the parameters. Different parameter values will, of course, change the scaling.

Profiles:

The scale Length r_0 is given by

$$r_0 = \left(\frac{y_1 - y_0}{y_0 - y_2} \right)^{1/2\delta}$$

The density profile $n(r)$ is then:

$$n = n_0 \left[\frac{1 + (a/r_0)^{2\delta}}{1 + (r/r_0)^{2\delta}} \right]^2 \frac{(r/r_0)^{2\delta-2}}{(a/r_0)^{2\delta-2}}$$

The density profile $n(r)$ is plotted in fig. (3). The scale will change but the shape will remain invariant for different parameter values.

Heating term

To get an accurate estimate of the corona conductivity and energy interaction with the core, it is important to have an accurate heat transport equation. This is one of the most difficult problems, since large amounts of heat are exchanged across the core-corona boundary, and since heat transport across large thermal gradients such as are set up across the boundary is as yet poorly understood. For the present, the simplest approximation is used, namely that of no net heat transport across the boundary. The is certainly true at early time, but thermal conduction from the hot corona to the core is likely to be important and influential to both core and corona at later times, and should be studied in the future. The coronal ohmic heating term is

$$\frac{\partial}{\partial t} \left(\frac{3}{2} n k T_2 \right) = \vec{j}(r) \cdot \vec{E}$$

which becomes, since $j = e n c_s$:

$$\frac{\partial k T_2}{\partial t} = \frac{2}{3} e c_s E.$$

86

Boundary conditions:

At $t = 0$, $T_1 = T_2$ and $n_2(a) = n_1(a)$. The electric field E is considered to be continuous across the core-corona boundary. For $t > 0$, current is continuous across the corona boundary:

$$n_0 = \frac{j_1}{ec_s(T_2)}$$

$$y_0 = \frac{2I_1}{c} = 0.4I_1 [A]$$

$$y_0' = a \left[\frac{4\pi}{c} j(a) \right]$$

Note that $y_1 > y_0 > y_2$.

Results

Corona characteristics for a Titanium z-pinch implosion are shown in fig. (4)–(11) as a function of implosion time. Parameters from the MHD simulation are first shown: The average ionization Z and the corona inner radius a are shown in fig. (4); the electric and magnetic fields are shown in fig. (5); and the temperature and current are shown in fig. (6). Then the corona parameters are shown: Fig. (7) shows the scale length r_0 compared to the corona inner radius; fig. (8) shows the theoretical position of maximum electron density (at a radius smaller than the inner corona edge a), while fig. (9) shows the density at the inner edge and at the maximum; fig. (10) shows the core and coronal current, and fig. (11) shows the core and coronal temperature. Note that the coronal current is nearly always at least an order of magnitude greater than the core current. The later-time conductivity of the corona is not realistic, however, because of the impossibly high temperatures it attains. This is because there is no cooling mechanism for the corona, and the conduction that

87

certainly occurs in reality is not accounted for. Thus, only the early-time results should be considered for dynamical conclusions. Still, these results do show the importance of heat conduction in cooling the corona, and motivate further work on finding a practical heat-transport term.

Conclusions

• The structure and characteristic parameters of a current-limited region have been presented. In this model corona, current is limited by scattering from ion-acoustic instabilities.

• Time evolution was followed of a turbulent corona of a simulated titanium wire z-pinch. Scale length, temperature and total current were calculated and compared to the pinch values.

• Although conductivity is limited, increased penetration of the electric field and reduced magnetic field results in significant heating, which enhances conduction.

• The corona can carry a significant fraction of the pinch current, especially early in the pinch.

• Accurate heat transport is very important to the model. Strong heating can cause the model to break down. Future work should include better calculation of radial heat conduction into the core as well as losses from atomic line radiation.
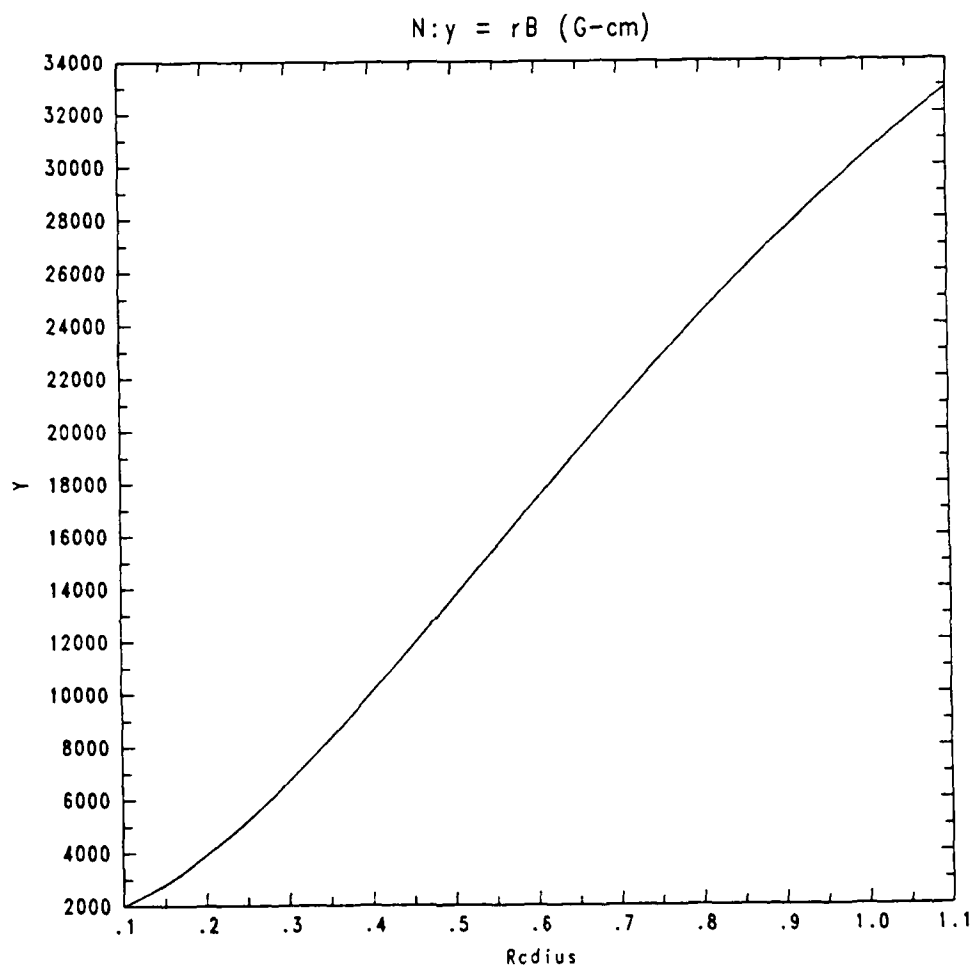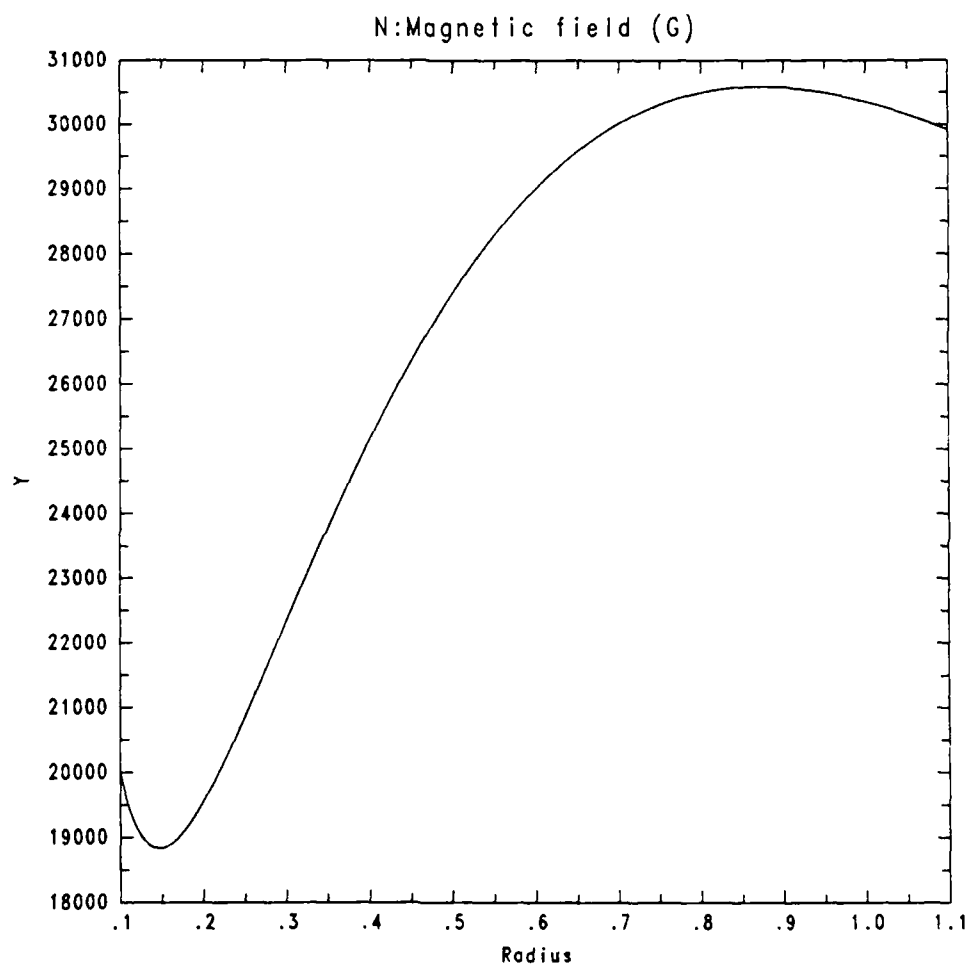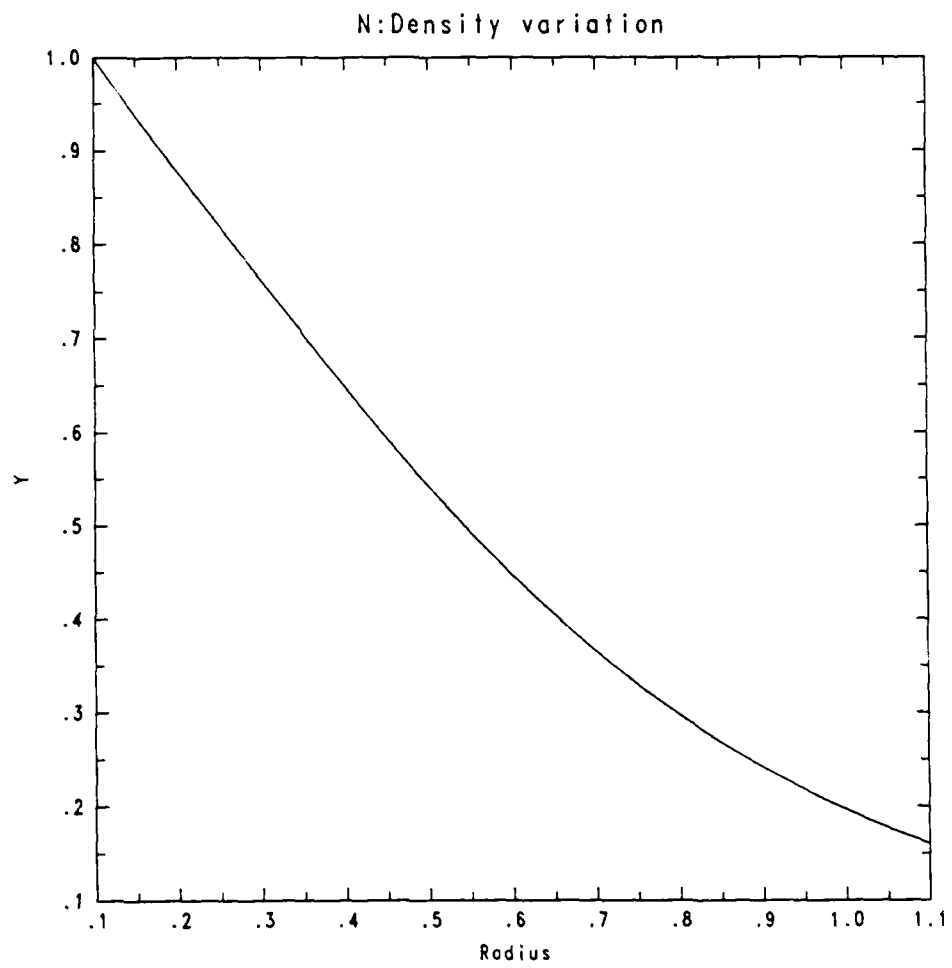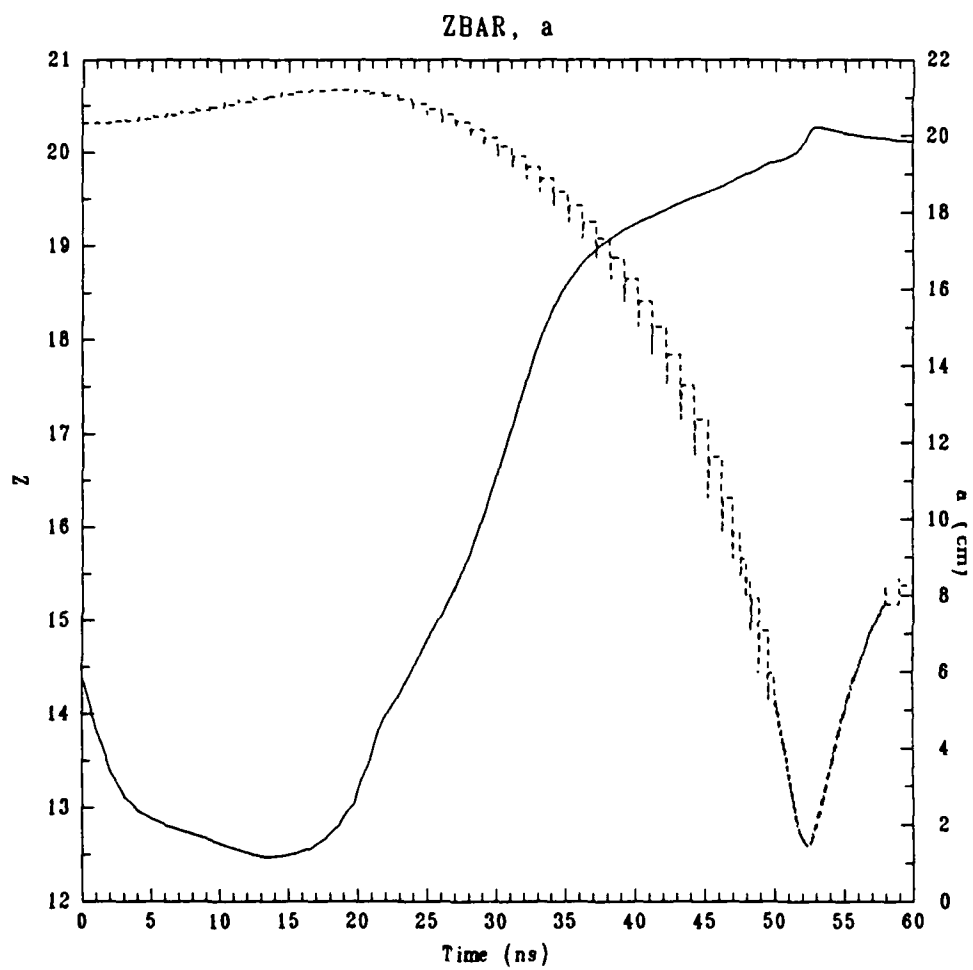
Figure 1

Figure 2

Figure 3

ZBAR, a

Figure 4

92

EFIELD, BFIELD

Figure 5

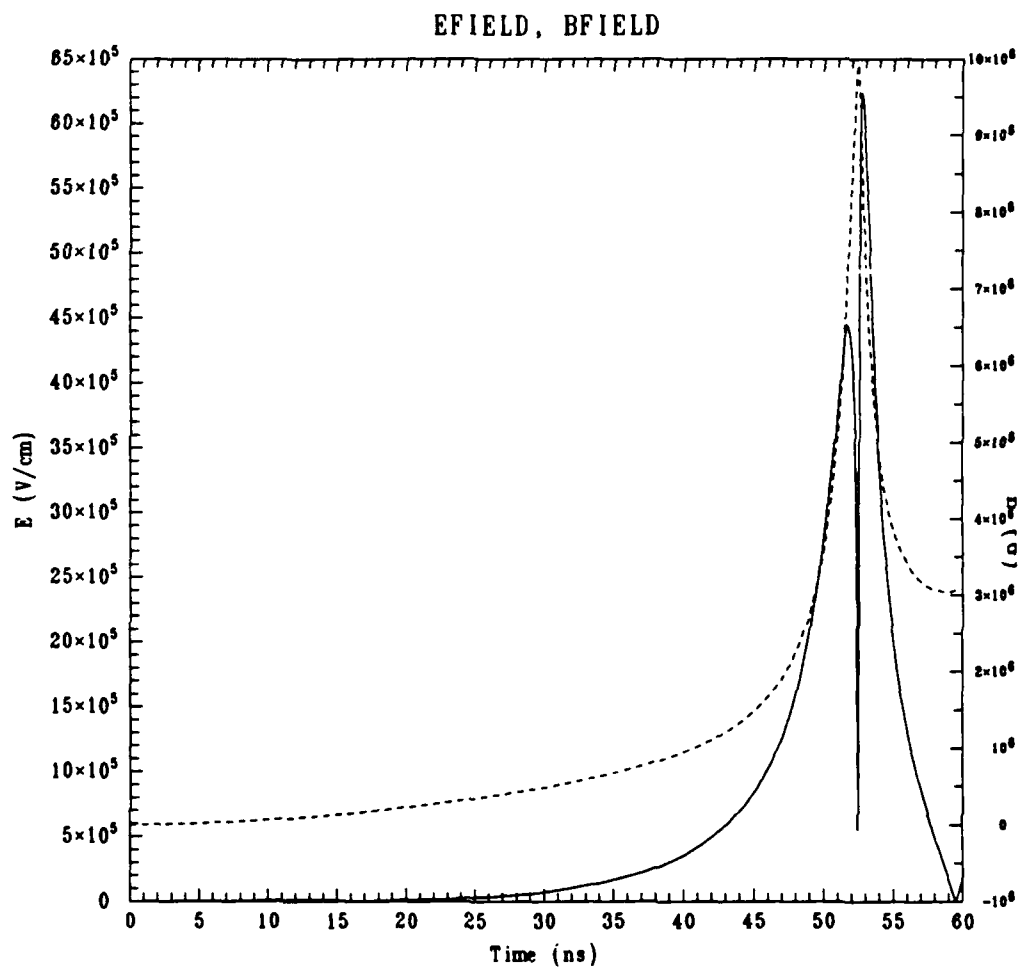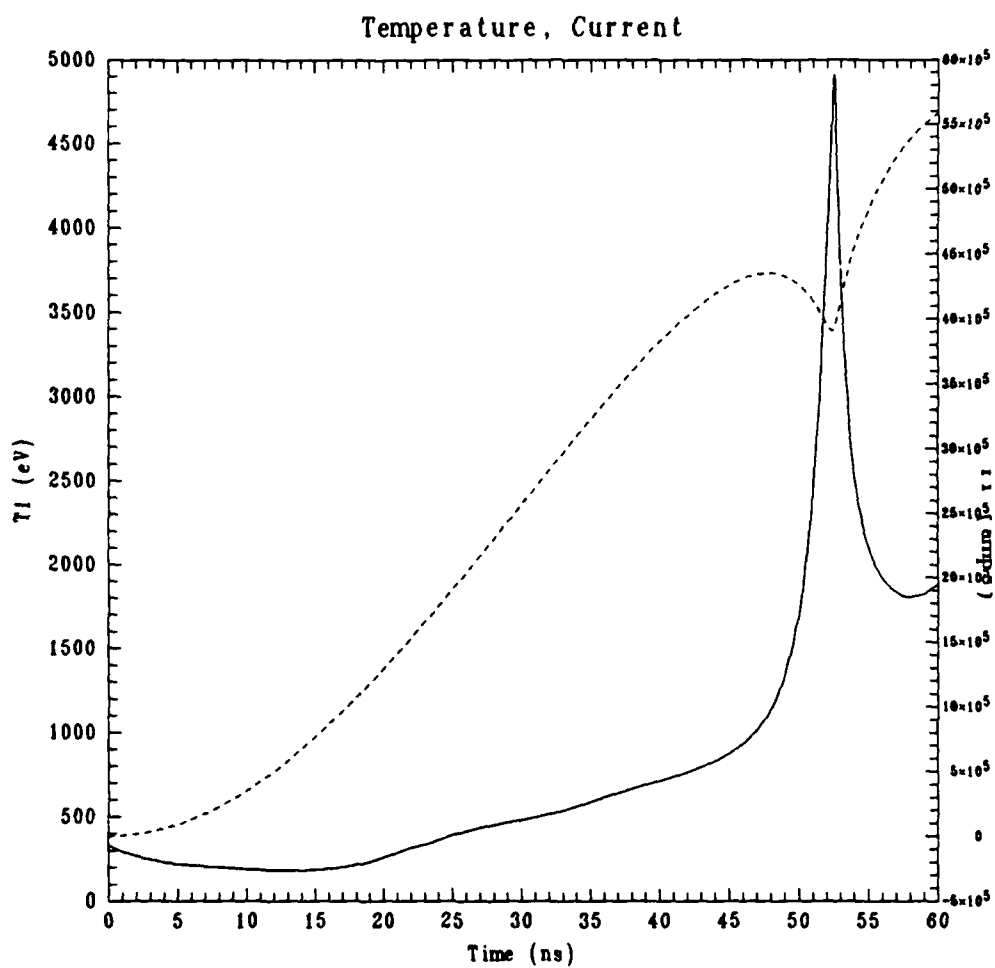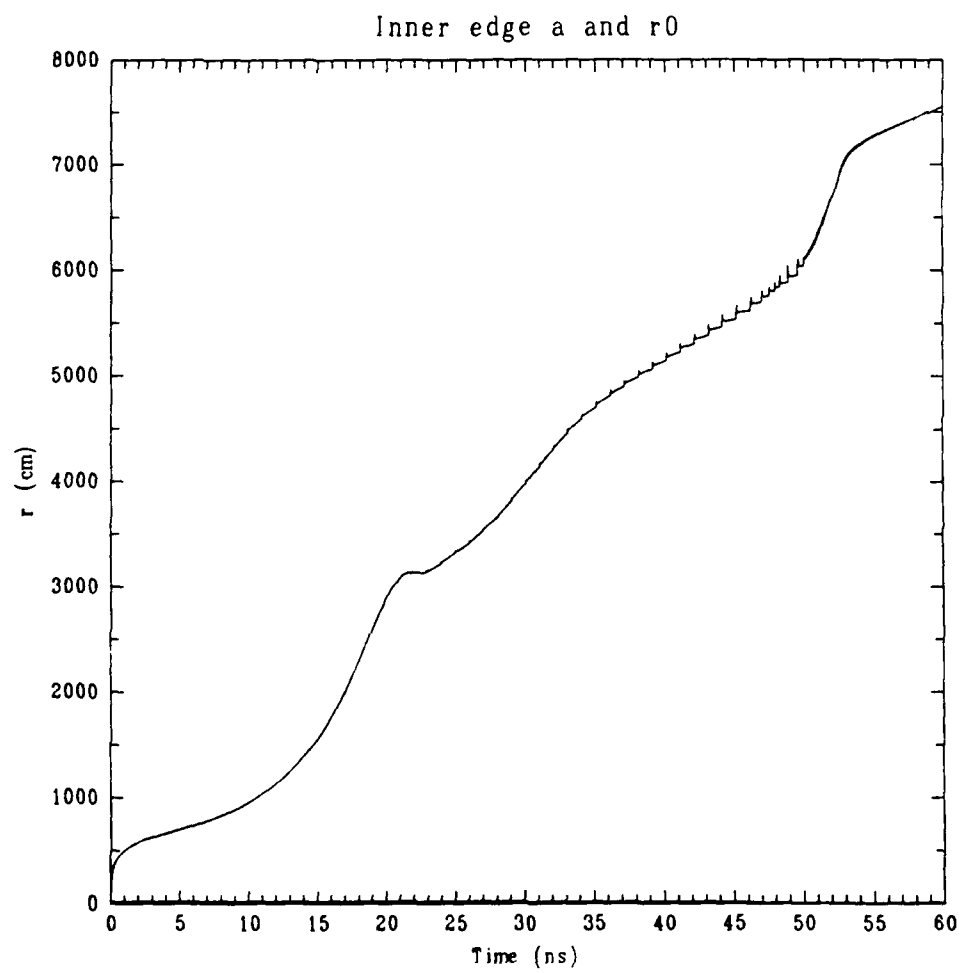Temperature, Current

Figure 6

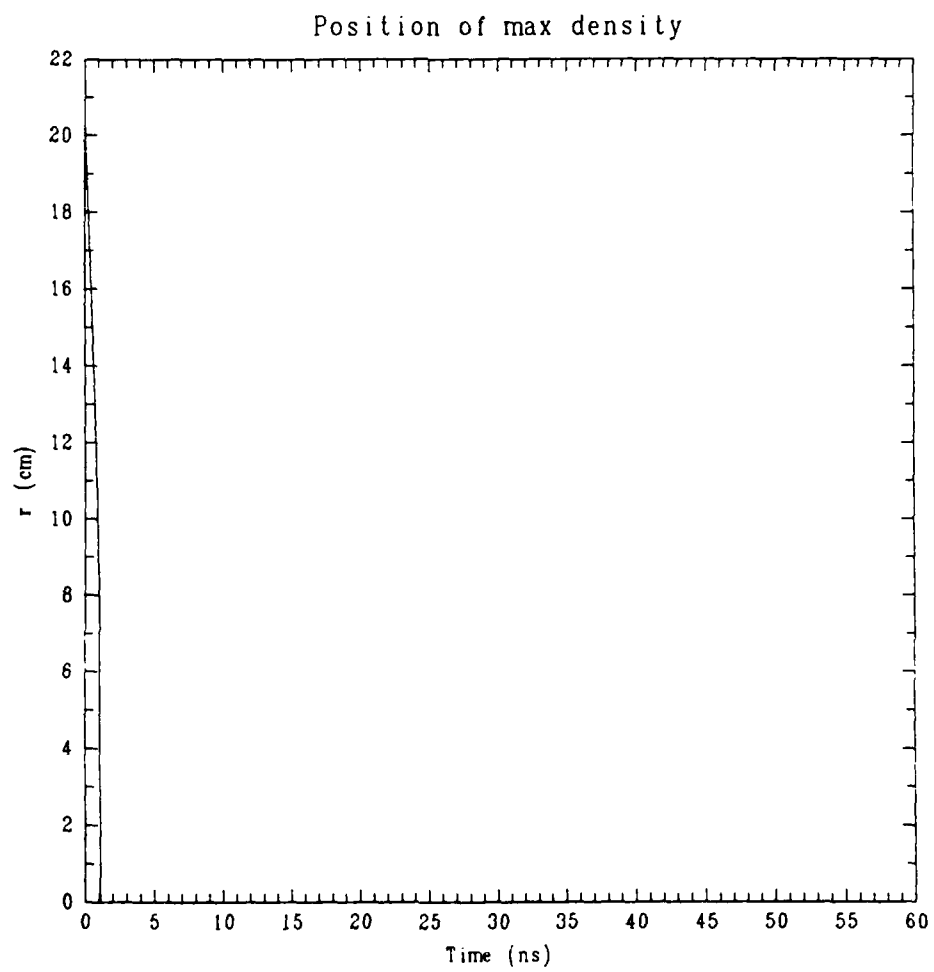Inner edge a and r0
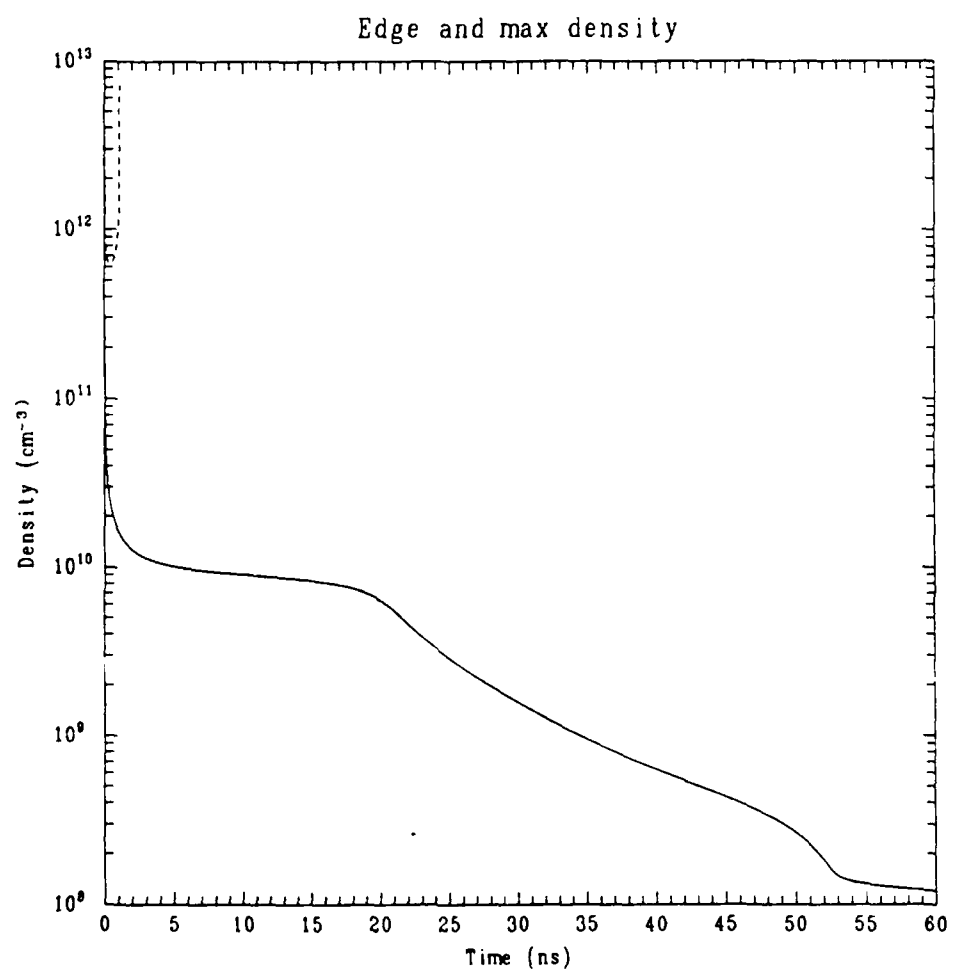
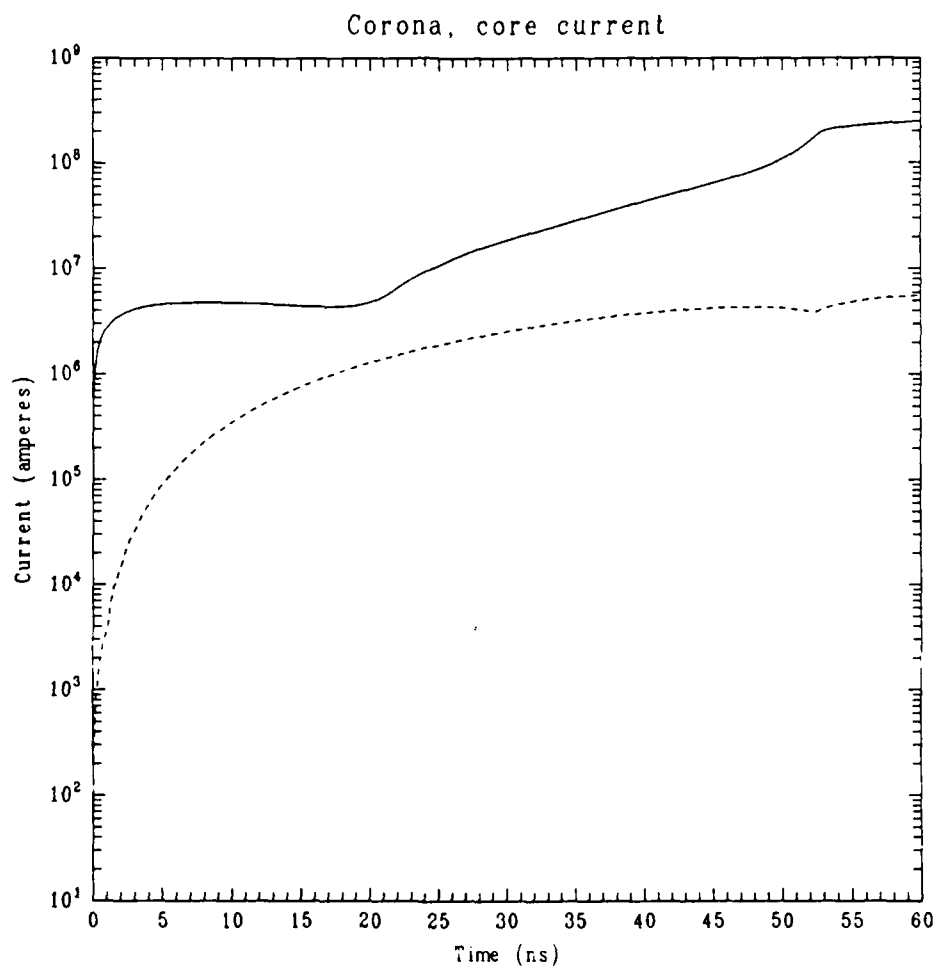Figure 7

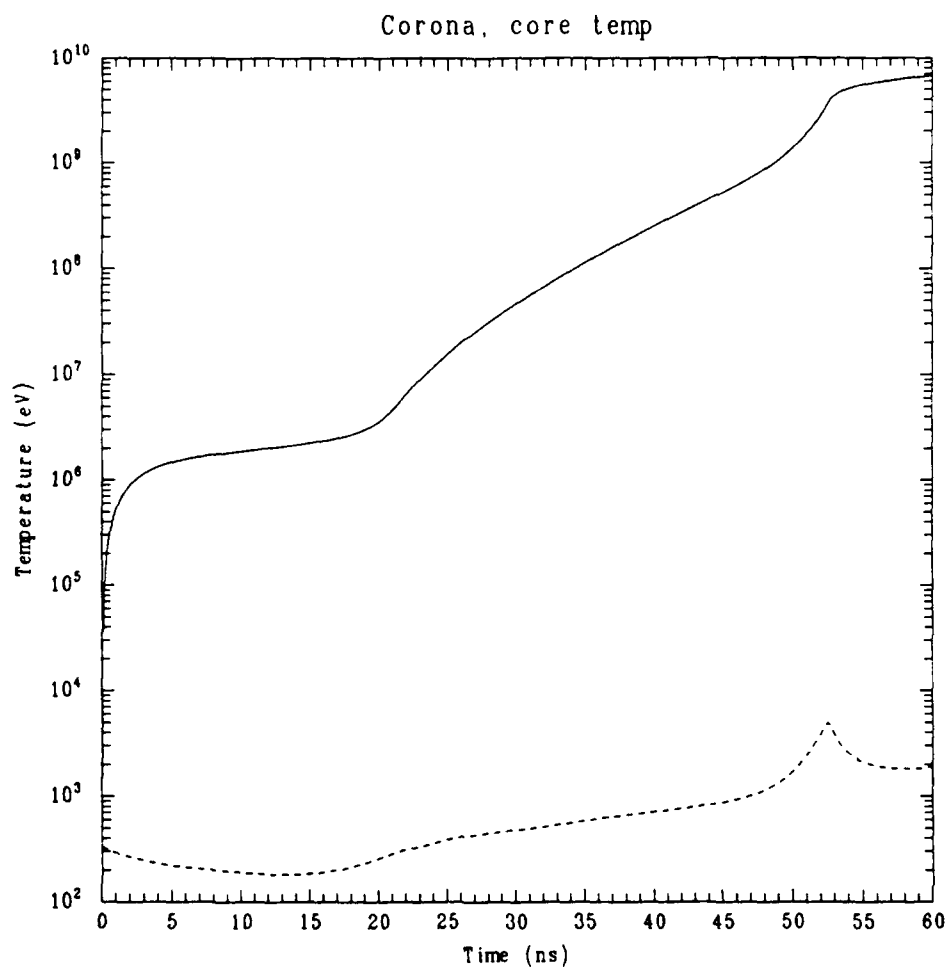Position of max density

Figure 8

Figure 9

Figure 10

Figure 11

V. New PRS Approaches

a) Modeling The Fast Screw Pinch PRS Load

Introduction

Plasma Radiation Sources (PRS) have always presented something of a dilemma to theorist and experimenter alike in that instability channels seem to occur more frequently than not in experiments, making it difficult to obtain detailed and meaningful comparisons between theory and experiment.

Yet, in order to scale K-shell yields to higher values in moderate Z elements, it is highly desireable that stable array implosions be achieved with large initial array diameters, which then allow a longer rundown period for instability growth. The known radiative efficiency of one dimensional PRS implosions in converting kinetic energy to heat and (K-shell) X-radiation leads therefore to efforts at stabilizing the laboratory plasma and thereby achieving the theoretical K-shell yields characteristic of large diameter implosions. There is no shortage of data indicating that both $m = 0$ and $m = 1$ motions are present in PRS loads, but the most disruptive of these is the "sausage" mode. The general strategy in sausage stabilization is to provide an axial magnetic field component which cannot be "sidestepped" by the plasma through an interchange of field and fluid, nor can the axial field be as easily compressed – it builds "backpressure" with an r^{-3} scaling as compared with the r^{-1} scaling of the pure z-pinch stress. The next order of refinement of this basic idea involves the details of the magnetic shear profile in the load, for in the simplest limit it is not so much the absolute magnitude of the axial field as the rapidity

of spatial change in the "safety factor" which stabilizes things. If one can find a practical, effective balance of axial and azimuthal magnetic fields, there will result a close laboratory approximation to the idealized, one-dimensional implosion process and a wider variety of load options, probably more forgiving in design tolerances, becomes accessible. For the screw pinch PRS then, our primary challenge is finding a means of suppressing the load instabilities in spite of all natural tendencies to the contrary. The physical model is more conventional and homogeneous in its composition, but the risk is that such an implosion path may not exist.

On the other hand, should the proclivity of Z pinches to distort into "sausages" and "kinks" be suppressed? Several approaches can, in principle, lead to the exploitation of these instabilites to enhance the radiative yield – perhaps through non-thermal processes[1,2]. A successful development along these lines, e.g. using X-pinches, must deal with very delicately balanced systems, designed to close tolerances and likely to develop large, rapidly evolving gradients in plasma conditions. Because of these stiff gradients, many competing processes must be folded into the analysis. X-pinch loads which might be productive sources of runaway electrons evolve into twin axial blobs with the current sheet expanded in a more diffuse structure near the midplane. A hot cavitated region between the blobs would be the expected source for useful fluences of supra-thermal electrons. Such a region would be only weakly magnetized, semi-collisional and quite likely microturbulent as well. The adjoining denser portions will be magnetized and more fluid like and thus domains requiring quite different theoretical limits can be expected to be in intimate contact. The initial conditions required to achieve the bifurcated end state and produce a reasonably deep density cavity are based on specific mass loadings as functions of radial and axial position. While the minimum tolerances in this mass arrangement required for a given level of performance are not known, it is

reasonable to expect a system somewhat unforgiving of perturbations away from the preferred initial state. It is a fair summary that all phases of X-pinch evolution contain rather challenging physics to unravel before a proper design is constructed. If all the details can be properly investigated and traded off, there will result a kind of "plasma judo" in which the natural motions of the load are amplified and channeled to the preferred evolution, but exploiting and fine tuning the instability is risky because so much disparate physics must be included in the design model.

Here we will explore the first of these equally promising general design pathways, a mix of magnetic field components. The blend of z and θ pinch field sets (respectively, the TM and TE modes) into a helical magnetic field has been explored extensively in the CTR community. For fusion devices global stability is essentially the only issue and perturbations must be damped on very long timescales compared to th PRS problem. In contrast, for a modern pulseline driver, the stability is needed for 100 ns timescales only and the load can be annular for much of the rundown. Since the annular load has the advantage of avoiding any substantial backpressure, it is (at least marginally) stable until the stagnation and compression phase wherein the timescales are futher reduced to 10 ns. Since the energy coupling efficiency between pulseline and load is improved with a greater dynamic range in load inductance during the rundown, the ability to achieve a stable compression over several centimeters of radius using a screw pinch load would be extremely beneficial to the PRS effort in general.

The screw pinch could therefore be an attractive PRS load if (i) it achieves a reasonable measure of stability against $m=0$ deformations, (ii) it can gain any advantage in power coupling to modern generators, and (iii) these things can be achieved with little or no loss in radiative efficiency. Using a radiatively coupled, 1-d ideal MHD fluid model equipped with an appropriate equation of state, the

global stability of various initial shear profiles can then be explored using modern criteria.

Until recently, the local stability criterion due to Suydam, as generalized to a screw pinch by Hameiri[3], was the most general applicable test. It is now established that global modes can exist in a screw pinch under some conditions, and the assessment of stability on any 1-D set of plasma profiles now rests on several distinct tests, following Bondeson[4,5],et.al.

There is one local criterion (generalizing Hameiri's result), in either the magnetohydrodynamic (MHD) or guiding center plasma (GCP) limit. Bondeson finds in the absence of axial or azimuthal flow that the "modified Suydam" spectrum is stable unless at any r_o

$$-\frac{2p'}{rB_z^2(\frac{\mu'}{\mu})^2} > \frac{1}{4} \quad .$$

Such a local criterion is not sufficient for stablility in the ideal MHD limit for there global modes can arise. These modes are stabilized in the GCP limit but, if one has an MHD profile such that $S(r_o) = (B^2 - \gamma P)\rho\tilde{\omega}^2 - \gamma P(\mathbf{k} \cdot \mathbf{B})^2 = 0$ anywhere, then the "global slow modes" are unstable if

$$D_S(\frac{v_S}{v_A}, S'', B, B', \mathbf{k} \cdot \mathbf{B}, k) > \frac{1}{4} \quad .$$

Alternately, if one has a MHD profile such that $A(r_o) = \rho\tilde{\omega}^2 - (\mathbf{k} \cdot \mathbf{B})^2 = 0$ anywhere, then the "global Alfven modes" are unstable if

$$D_A(\frac{v_S}{v_A}, A'', B, B_z', B_\theta', \mathbf{k} \cdot \mathbf{B}) > \frac{1}{4} \quad .$$

In these expressions $\tilde{\omega}$ is the local Doppler shifted frequency, $\tilde{\omega} = \omega + mv_\theta/r - kv_z$, γ is the adiabatic index, while μ is the winding number (it's derivative is the magnetic shear). It is related to the usual "safety factor" by $qR = \mu^{-1} = B_\theta/rB_z$. The

expressions D_A and D_S are complicated functions of the arguments listed, which we do not need to examine here, and for simplicity the modifications in the Suydam index due to axial and azimuthal flow are suppressed. Those modifications are quite important in the MHD limit, however, and can be included readily as the model develops.

From this discussion it is worth noting that, in the MHD limit, we must deal with spatial derivatives up through second order in assessing the stability. For this reason some care has to be taken in building an accurate solution of the fluid equations so that noisy fluid profiles do not lead to erroneous judgements on the worth or accessibility of any particular load design. A present only one screw pinch load experiment is active, at Maxwell Laboratories, Inc.; we will examine it in some detail later. The range of possible experiments is quite wide, spanning all manner of axial field profiles, and is largely unexplored. The mapping our present model makes possible is intended to help narrow the field of approaches, but to do that one must be able to quantify the global accuracy of the fluid solution in some detail for various problems and timescales. It is for this reason that the benchmarking process has been pursued with tenacity.

We will present below some variations on well-known self-similar MHD flows which admit a very straightforward (0-d) "gas bag" model that in turn allows us to simulate existing screw pinch load schemes in the context of the DNA decade machine. We will discuss the details of the "gas bag" model and examine the energy coupling tradeoffs with increasing external axial magnetic field in the load region.

The Simplest Picture of Energy Coupling

A. The Gas Bag Model

The self-similar implosions can be used as benchmarks, but they also have a second application as generic pinch models. The utility of such models is clearly limited to the identification of trade-offs in load mass, initial position and the like; the caveats associated with their application are numerous. In PRS theory, whenever such a model is used, we are implicitly saying that either (i) the detailed profiles of the 0-d model are really accessible, or (ii) some interior dissipative process acts to make such profiles emerge, or (iii) they represent some radially averaged load state. Here a mix of all these limits is contained in the model.

The profiles which arise are expressed most conveniently in terms of the dimensionles ratio $\xi = r/a = r_o/a_o$; homogeneous compression requires that $r = \alpha(t)r_o$, and $a = \alpha(t)a_o$. Once given the time development of $\alpha(t)$ the profiles are then seen to "breath" in and out in the laboratory frame while they remain frozen to the ξ value in the locally advecting frame defined by $v_r(\xi)$. For the screwpinch, neglecting normalizing factors, one has

$$n(\xi) = exp - \xi^2$$

$$b_z(\xi) = \sqrt{\delta_1(1 - exp - \xi^2) + \delta_2 exp - \xi^2}$$

$$i(\xi) = \xi b_\theta = \sqrt{(1 - (1 + \xi^2)exp - \xi^2)}$$

$$v_r(\xi) = \dot{\alpha}\xi r_o$$

Are these special profiles in any sense accessible to the load? Plasma viscosity could play a role in producing and maintaining self-similar states if it is both

nonlocal (characterized by a mean relaxation time $\bar{\tau}$) and much stronger than classical small angle collisions would predict. Clearly the current programming path to homogeneous compressions is not general enough to be a dominant process, so some dissipative mechanism would be required. A second ingredient of homogeneous compressions is an isothermal temperature profile. In the loosely defined "gray body" limit, viz. sufficient opacity to make the radiative cooling profile peak near the surface, the interior radiative exchange of energy is usually very effective at keeping the temperature constant over the bulk of the pinch. This implies that ohmic heating, if included, can be done in a spatially averaged sense without acconting for the detailed (and nonuniform) current profiles implied by the self-similar motion – only form factors of $\mathcal{O}(1)$ would modify the resistance in that case. The Gaussian density profile is surely not the only one likely to emerge from the closure of an annular PRS load, but it does resemble the density profiles obtained in 1-d calculations.

On the other hand, the resulting ODE for $\dot{U} = \ddot{\alpha}$ possesses the proper scalings with radius (α) for all the separate components of the stress – pressure(ν_S^2), axial magnetic field pushing in or out ($\nu_{B_z}^2$), azimuthal magnetic field ($\nu_{B_\theta}^2$), and viscosity($\bar{\tau}$). If instead of separating the momentum equation and solving for profiles, we had spatially integrated the separate stress components and used the average values to assign a strength to each of the separation constants, the result would have been the same. In other words, profiles in r_o which differ from the special self-similar ones would simply produce slightly different values of the (arbitrary) separation constants if averaged over some spatial domain. The details of such form factors are hopefully less important in the pinch dynamics than the radial scalings of each competing stress component, although certainly these details are not trivial. Only comparisons with full 1-d calculations can resolve the most salient of these

differences but in the spirit of a "coarse grained" examination of screw pinches in modern pulselines one may state the "gas bag" model as follows.

The differential equaiton for the relative radial motion is

$$\ddot{\alpha}(\alpha) = \left(\frac{2\nu_S^2}{\alpha} - \frac{i\nu_{B_z}^2 - ii\nu_{B_z}^2}{\alpha^3} - \frac{\nu_{B_\theta}^2}{\alpha} - \frac{\dot{\alpha}}{\alpha^2}\frac{2}{3}\bar{\tau}\nu_S^2\right)$$

with $\alpha = r(\tau)/r_o$, $\Theta_e = T_e + (\frac{2}{3})\frac{U}{Z}$, and

$$\nu_S = \sqrt{(Z+1)T(\Theta_e)/m_{ion}r_o^2} .$$

The axial magnetic frequencies are split into current dependent, compressing exterior (i) and initially fixed, retarding interior (ii) components; while the azimuthal magnetic frequency is related to a generalized Bennett current, viz.

$$i\nu_{B_z} = \frac{\pi N I(\tau)}{c\sqrt{\Upsilon}} \quad , \quad ii\nu_{B_z} = \sqrt{\frac{ii B_z^2}{4\pi m_{ion}n_o r_o^2}} ,$$

and

$$\nu_{B_\theta} = \frac{I(\tau)}{r_o^2\sqrt{\pi c^2 m_{ion}n_o}} .$$

The inductance and impedance can be shown to be

$$L = 1.8 \cdot 10^{21} l_p/c^2 \left(\ln\frac{r_w}{r} + \frac{1}{2}(r_w^2 - r^2)[2\pi N]^2\right) [nH] ,$$

$$Z = Z_o - \left(\frac{\dot{r}}{r} + [2\pi N]^2\dot{r}r\right) 1.8 \cdot 10^{12} l_p/c^2 [\Omega] ,$$

$$Z_o = 3.257 \cdot 10^{-6}(l_p/\pi r_o^2)\left(\frac{\Lambda}{10}\right)\frac{Z}{\alpha^2 T_e^{\frac{3}{2}}} [\Omega] .$$

Here l_p is the pinch length, N is the return current winding number (per cm), and r_w is the radius of the return current cage. The factors Υ and n_o are the pinch mass

per cm and mean ion density; for a strictly self-similar Gaussian they are related by $\Upsilon = m_{atom} n_o \pi a_o^2$. The heating equation can be written

$$\dot{\Theta}_e = -\frac{4}{3}\frac{\dot{\alpha}}{\alpha}T_e(\Theta) + \frac{8}{9}(\frac{\dot{\alpha}}{\alpha})^2\frac{1+\mathcal{Z}}{\mathcal{Z}}T_e(\Theta)\bar{\tau} + Z_{po}\frac{I^2\mathcal{Z}}{\alpha^2 T_e^{\frac{3}{2}}} - P_{rad} \, ,$$

where $Z_{po} = Z_o(1.0375733 \cdot 10^{-11} A/l_p \Upsilon)$ is the specific impedance (per ion).

Because of the strong radial scaling of the type i axial magnetic compression it is possible for this model to fall into a radiative collapse phase toward the end of an implosion cycle. In contrast to the more common notion of refrigerative collapse however, the compression here is driven from the exterior axial magnetic field and cannot terminate unless either the current is depleted from the pinch due to high terminal impedance or the equation of state changes rapidly to stiffen the radial scaling of the retarding pressure term. Indeed so much increase in density ($\geq 10^{23}$ ions per cm^3) is implied for this class of solution that we will examine its relevance separately and here seek its border in the parameter space mainly to avoid it.

B. A Screw Pinch Load in the Decade Machine Environment

The present experiment at Maxwell Laboratories takes it roots in a scheme due to Colgate[6] for stabilizing a pinch without having to compress the axial field which is providing the stability. By twisting the return current cage in the diode front end some axial magnetic field is produced by the full driver current and the load can be stabilized. This means to a fast PRS load appears to suffer coupling losses if driven by decade class machine models.

The gas bag model above is used in conjunction with the transmission line model of Ref. 1, and the driver is chosen as a model of the Falcon x10 machine. As the windings per centimeter are increased past about 0.125 to a value of 0.25, the energy delivery to the model load falls off by about 10% and will continue to decay

because of the added inductance. The typical implosion scenario of such a screw pinch load in concert with a Falcon type inductive store is shown in Figure 1(a). The typical performance of a screw pinch load as a function of the N value, all other parameters being equal, is shown in Figure 1(b). The use of a high winding number for stability is apparently not a very attractive strategy once N exceeds 0.125 or so. The actual stability requirement is not known for this particular set of field profiles, but will be left to future work.

References

1. R.E. Terry and F.L. Cochran, NRL Memo Rep. 6491, 1989, "Energy Transfer from High Power Pulselines to the Next Generation of PRS Loads"

2. F.L. Cochran and J. Davis, "Evolution of an X-pinch Plasma", submitted to PFB.

3. E. Hameiri, ERDA Report C00-3077-123, MF-85.

4. A. Bondeson, et. al., PF 30(7), 1987, p.2167.

5. A. Bondeson, et. al., PFB 1(7), 1989, p.1431.

6. S.A. Colgate, et. al., Proceedings of the Conference on Peaceful Uses of Atomic Energy, 32, 140 (1958).
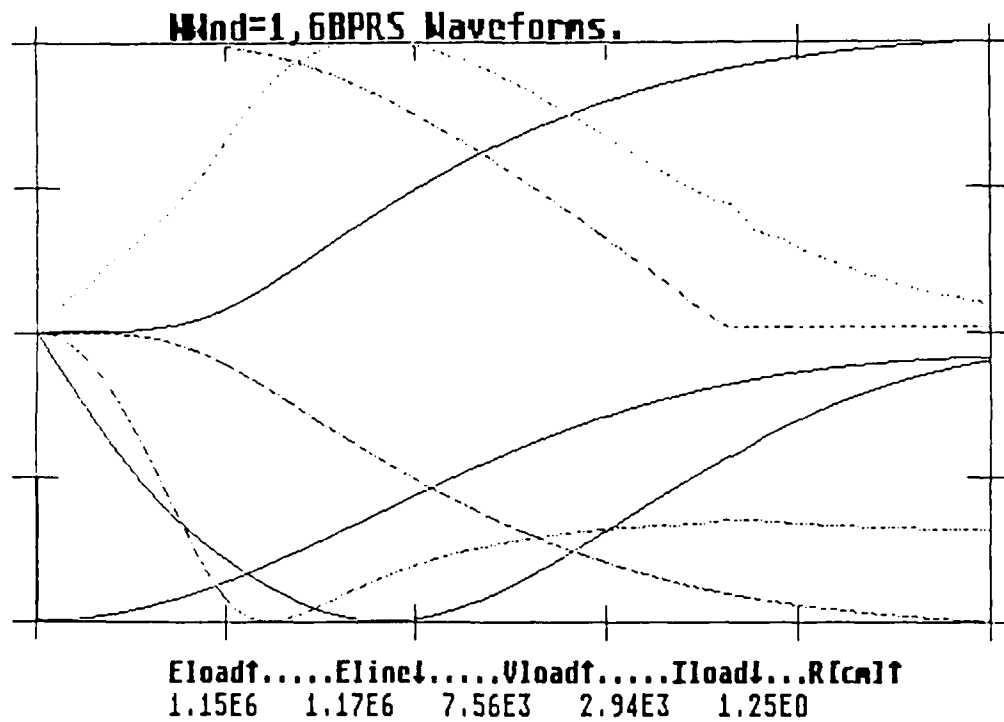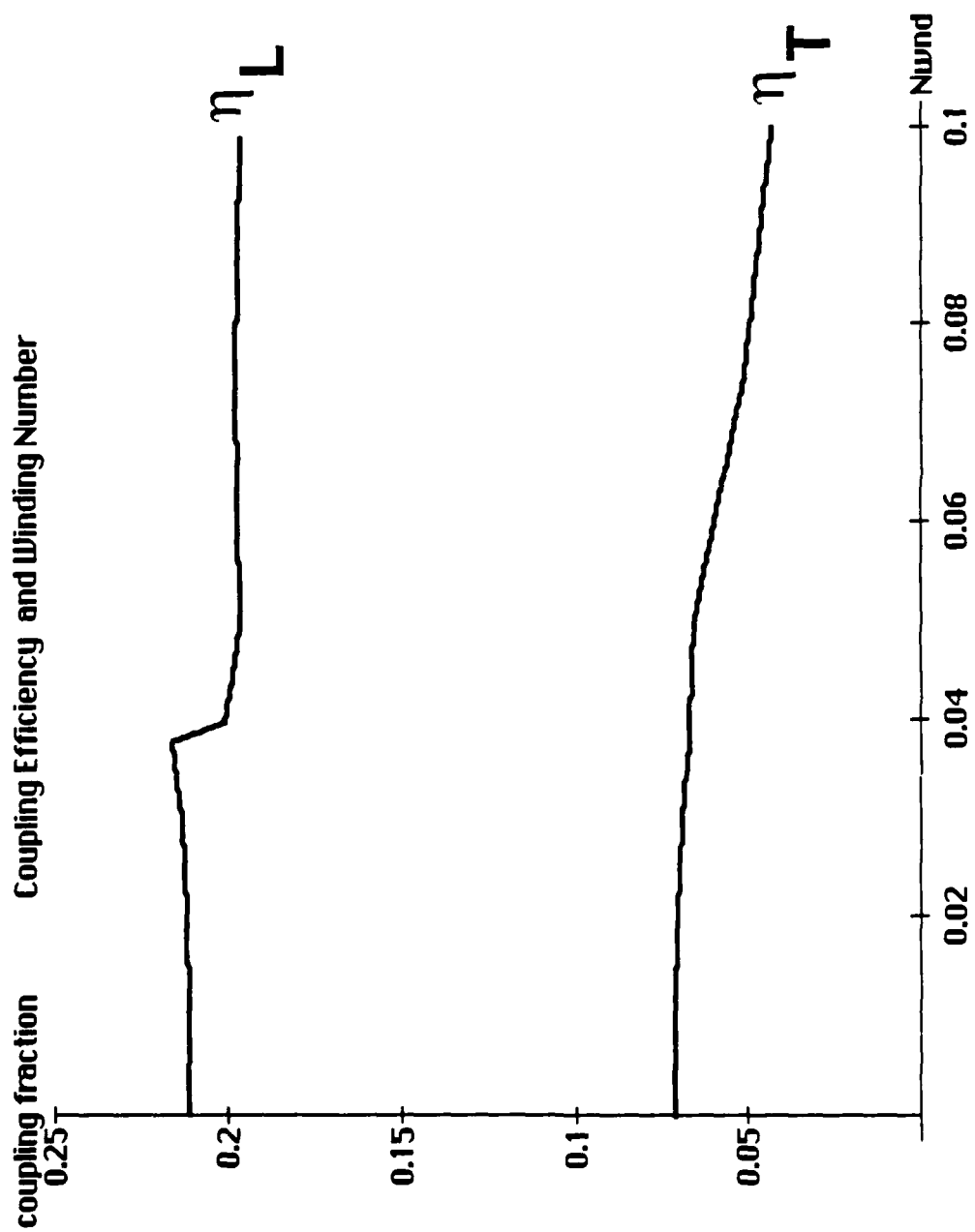
Falcon Driver and Gas Bag PRS Screwpinch

Figure 1(a)

Coupling Efficiency and Winding Number

b) Ring Plasma Stagnation Dynamics

We investigate the radiative properties and dynamics of an argon ring-puff plasma as it collides with and stagnates on a planar iron surface. Hydrogen ring plasmas have been produced experimentally with velocities exceeding 10^8 cm/sec, and should thus be capable of generating a high temperature, high density plasma on impact with a target. Such a plasma would efficiently convert the kinetic energy of the ring plasma into multi-keV radiation. The interaction of the ring puff with the target is simulated with a 1D non-LTE multimaterial radiation hydrodynamics model which self-consistently includes the effects of opacity and line broadening. This study has two principal goals: to determine the importance of wall losses, and to characterize the radiation produced in the stagnation process.

The puff gas was modeled in 1D by a uniform argon plasma moving at uniform velocity u_0 into the iron wall plasma. This is a reasonable approximation for timescales less than D/u_0, where D is the diameter of the ring. Argon was selected as the gas-puff material, since hydrogen (and other low-Z) materials become fully stripped in a high-velocity stagnation, and cease to radiate efficiently. By modeling the interaction in this way, we have emphasized the stagnation and radiation physics, and ignored questions relating to the acceleration of the ring-puff and its stability. However, we view these latter issues as technological, since hydrogen puffs with the appropriate characteristics have already been produced.

A benchmark simulation was first performed, where ionization, radiation and thermal conduction were neglected. This idealized case has an analytic solution: the stagnation results in the formation of a layer of shocked argon (the iron remains cold), with a density ratio of 4:1 for large Mach numbers, and the temperature of the shocked argon is given by $kT = \frac{1}{3} m_i u_0^2$, where m_i is the mass of a gas-puff ion, for the case of no ionization. Thus, for the idealized case (no wall or radiative losses, no ionization, etc.), the stagnation temperature scales as the square of the puff velocity. A schematic of this situation is given in **Figure 1**. The computer simulation reproduced the analytic model fairly accurately; it is a severe test of the code, since the gradients are very large and the computational mesh must be severely stretched to provide adequate resolution in the interface region.

Full radiation-hydrodynamic simulations with detailed atomic models for iron and argon were performed for several puff velocities: $u_0 = 1 \times 10^8$, $u_0 = 2 \times 10^8$ and $u_0 = 3 \times 10^8$ cm/sec. In each of these cases, a hot argon layer is created initially at the interface with the wall plasma, which grows in size with time. A weak shock wave propagates into the wall plasma, and energy transport by radiation and thermal conduction heats the iron plasma and produces an ablation into the argon puff. An energy history for the 2×10^8 cm/sec case is shown in **Figure 2**. Initially, most of the energy in the system is in the kinetic energy of the argon puff. As the stagnation onto the wall proceeds, kinetic energy is converted into thermal energy, and the heated plasma ionizes (ionization energy) and radiates (radiated energy). By about 0.45 nsec, most of the kinetic energy is

thermalized, and the hot plasma begins to expand. In the expansion phase, thermal energy is converted into kinetic, and ionization energy is converted into thermal (and radiation) through recombination. The radiated energy is lost to the system.

In **Figure** 3, the hydrodynamic variables (density [g/cm^3], temperature [eV], pressure [ergs/cm^3 x10^{-12}], velocity [cm/nsec x10^{-2}] and radiative cooling [ergs/cm^3-nsec x10^{-14}]) are plotted versus displacement in centimeters for the 2x10^8 cm/sec case at 0.33 nsec, just before the minimum in kinetic energy. It can be seen that the frontside of the iron plasma is hot (about 2.5 keV), and blowing off into the argon plasma. The radiative cooling peaks just behind this blowoff plasma, where the density and temperature are both moderately high. The temperature in the argon puff is nearly uniform (about 3.0 keV) at this time because of thermal conduction and radiation transport. The emission spectrum at this time is shown in **Figure** 4. This spectrum and the radiation data in the tables described below were post-processed using extended atomic models (more detailed than required for energetics). The spectrum is characteristic of a high density plasma; continuum radiation dominates the line emission. In contrast, wire plasmas and ordinary puff-gas plasmas generally reach lower densities than are achieved in the present configuration, and are less dominated by continuum emission.

For puff-gas velocities substantially smaller than 2x10^8 cm/sec, much of the energy radiated above 2 keV comes from argon K-shell lines (principally from the transitions n=2 to n=1 of Ar XVIII and 1s2p(1P) to 1s^2 of Ar XVII); however, in the present case, most of the multi-keV energy is produced by bound-free processes in the hot,

dense iron plasma (principally recombination into lithium-like states). A breakdown of the instantaneous radiated powers at 0.33 nsec by element and by type (line, recombination and bremsstrahlung) is given in **Table I**. It can be seen that the total radiated power from the iron plasma is almost an order of magnitude higher than that from the argon; this ratio increases with puff velocity. The radiation is broken down into several energy ranges in **Table II**. At 0.33 nsec, the power peaks in the 2-4 keV range; however, there is comparable power radiated in the 1-2 keV, 2-4 keV and >4.0 keV bands. The largest contribution to the power above 1 keV is bound-free radiation from the relatively dense iron plasma, as described above.

A temperature history plot (log_{10} temperature contours versus position and time) is given in **Figure 5** for the 2×10^8 cm/sec case. Each horizontal slice represents a specific time, and the bottom edge corresponds to the init al conditions (7.5eV argon and 0.7eV iron). The void at the right side of the plot corresponds to the outer edge of the ring-puff, which moves inwards until the stagnation is complete at about 0.45 nsec, and then moves outwards in the expansion phase. The peak temperature calculated in the simulation is a little more than 3 keV, whereas the stagnation temperature for an ideal gas ($kT_s = {}^1/_3 m_i u_0{}^2$) is 533.3 keV. Hovever, the argon ionizes to the H and He-like state (16-17 times ionized), and much of the iron ionizes to the Li and Be-like state (22-23 times ionized). Therefore, most of the kinetic energy goes into heating the electrons. Additionally, radiation and thermal conduction carry energy into the dense wall plasma and out into the unshocked puff-gas. Finally, energy is expended in ionizing the plasma and energy

is radiated away.

By about 0.1 nsec the puff gas has become nearly isothermal (about 3 keV). The stagnation phase ends at about 0.45 nsec; at this time, the argon is beginning to cool. The front side of the iron becomes warm and begins to expand into the gas puff by 0.1 nsec. The iron/argon interface is shown in **Figure 6**. The heating and expansion continue throughout the stagnation; when the gas puff begins to expand and cool, the front side of the target also begins to cool. However, energy continues to be transported into the iron plasma, and this energy is radiated away at a rate that maintains the rearside temperature near 100 eV from about 0.3 to beyond 1.2 nsec.

A history plot of the radiated power is given in **Figure 7**. There are two distinct radiating regions: one at the frontside of the iron plasma, and the other in the argon plasma just ahead of the iron/argon interface. Net radiation loss is plotted; there are regions that are net absorbers of radiation. The radiation cooling is the greatest in places where temperature and density are simultaneously large. The cooling peaks at about the same time that the kinetic energy is a minimum, and it declines (maintaining two spatially distinct regions) as the plasma expands and cools.

Some idea of the complexity of the puff-target stagnation can be seen from the history plot of mass density for the 2×10^8 cm/sec case, shown in **Figure 8**. Substantial puff-gas compression occurs initially near the iron interface, but expansion takes place just behind this region as a consequence of local heating (due to radiation transport and thermal conduction). Eventually, the outer edge of the argon

116

plasma becomes rarefied because of energy transport deep into the gas-puff. The ablation of the iron target can also be discerned, as well as alternate compression and rarefaction near the interface as localized "bouncing" occurs. The density in the bulk of the iron plasma monotonically decreases due to heating and subsequent ablation into the gas puff.

Temperature history plots are given in **Figures 9 and 10** for the 1×10^8 cm/sec and 3×10^8 cm/sec cases, respectively. The most obvious trend which can be seen from the temperature histories is the dependence of the "bounce" time on u_0, the initial gas-puff velocity. Another obvious trend is the increase of temperature, both in the puff and in the iron plasma, with increasing u_0. Peak temperatures reach about 1.8, 3.0 and 4.0 kev for the 1.0, 2.0 and 3.0×10^8 cm/sec cases. Finally, it can be seen that transport of energy into the puff becomes more efficient at higher puff velocities. A nearly isothermal puff-gas is produced almost immediately at 3×10^8 cm/sec; it requires about a half a nanosecond for thermal gradients in the puff to be correspondingly reduced at 1×10^8 cm/sec.

It has been confirmed that the stagnation of a high velocity ring-puff plasma on a planar solid density target can generate a high density, high temperature plasma, which can efficiently generate multi-keV radiation. However, several questions remain. These include the importance of 2D effects which were ignored in this study, and the importance of non-fluid behavior at the puff-target interface (high-velocity ring plasma ions may penetrate the target and, in extreme cases, the interaction may resemble a deposition

117

rather than a stagnation if the B-field insulation breaks down). In addition, the adequacy of the atomic models employed in this study should be further investigated. In particular, the adequacy of the structure in the lower ionized states of iron should be scrutinized. Finally, there may be magnetic (or electric) fields produced in the acceleration of the ring puff, or in its interaction with the target, which could affect the dynamics. These complications are currently under investigation.

TABLE I
Instantaneous radiated powers (W/cm^2)
[2x10^8 cm/sec case at 0.33 nsec]

	Iron	Argon	Total
Bound-bound	1.52×10^{13}	2.34×10^{12}	1.75×10^{13}
Bound-free	5.22×10^{13}	5.49×10^{12}	5.77×10^{13}
Free-free	4.38×10^{12}	1.07×10^{12}	5.45×10^{12}
Total	7.18×10^{13}	8.90×10^{12}	8.07×10^{13}

TABLE II
Instantaneous radiated powers (W/cm^2)
[2x10^8 cm/sec case at 0.33 nsec]

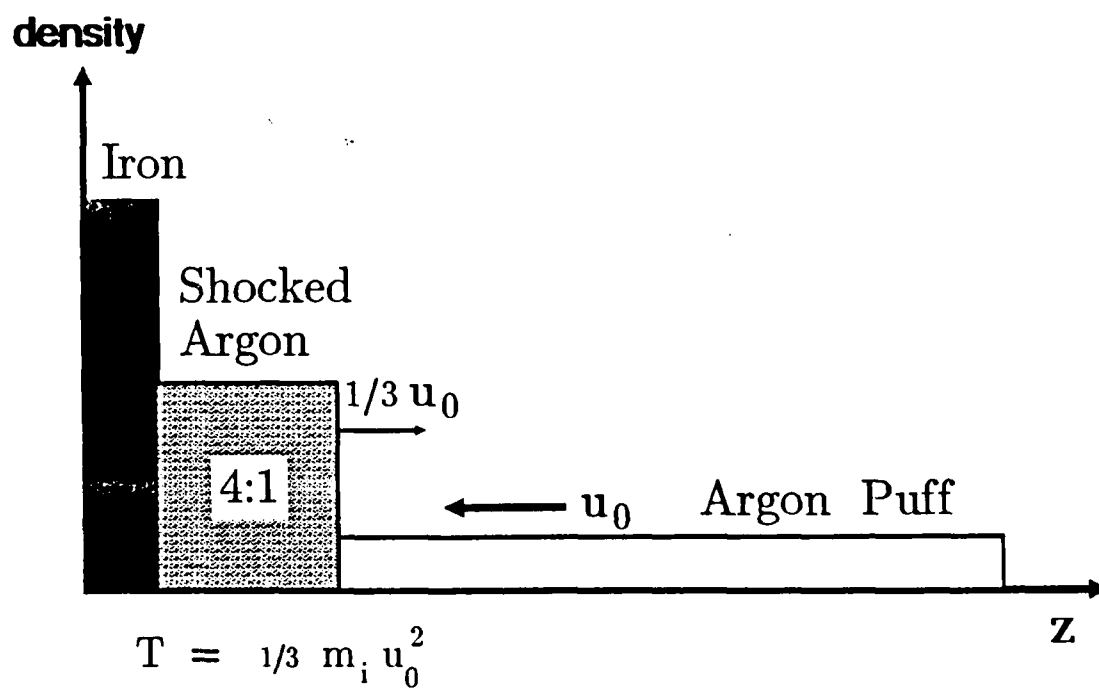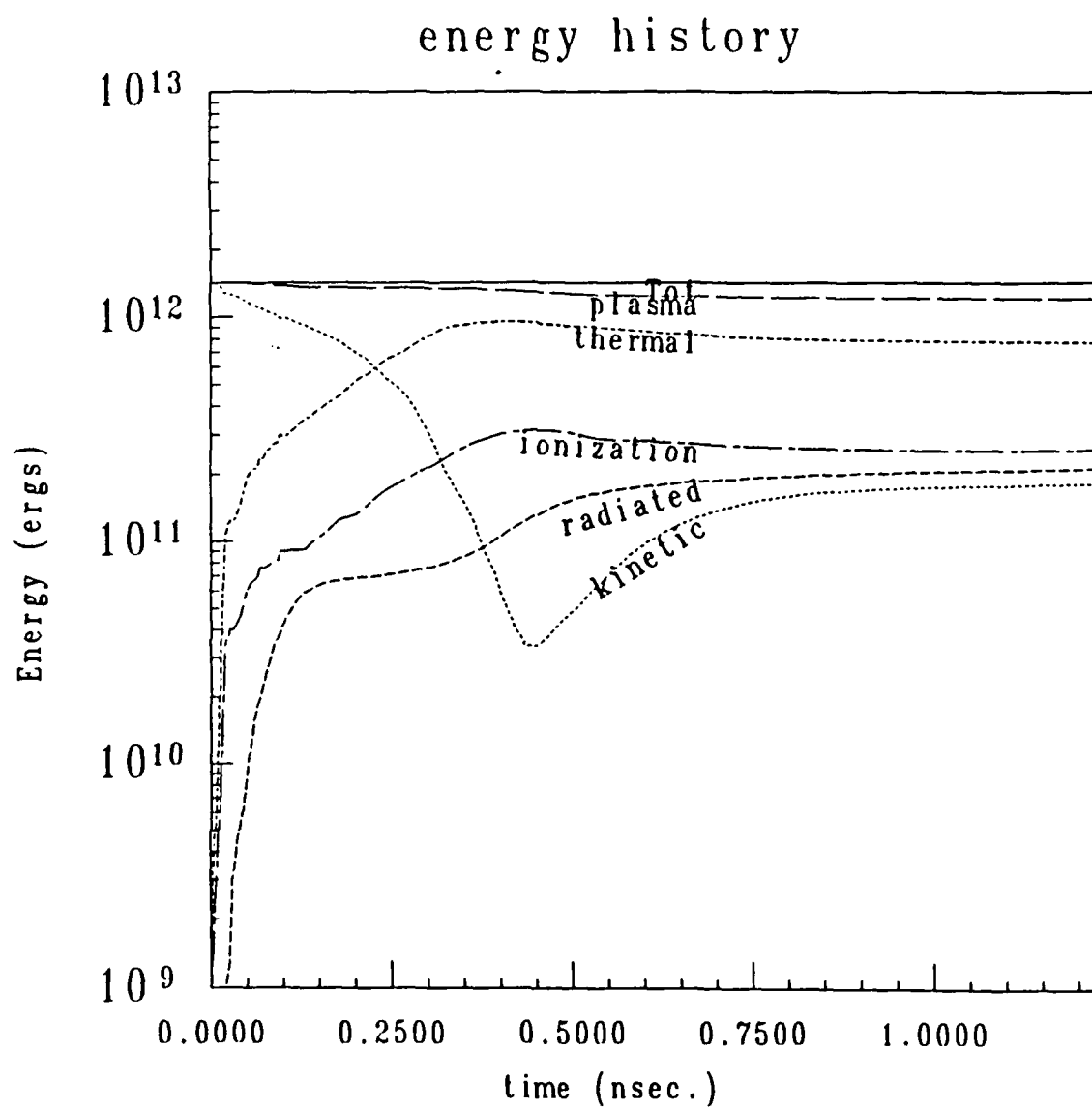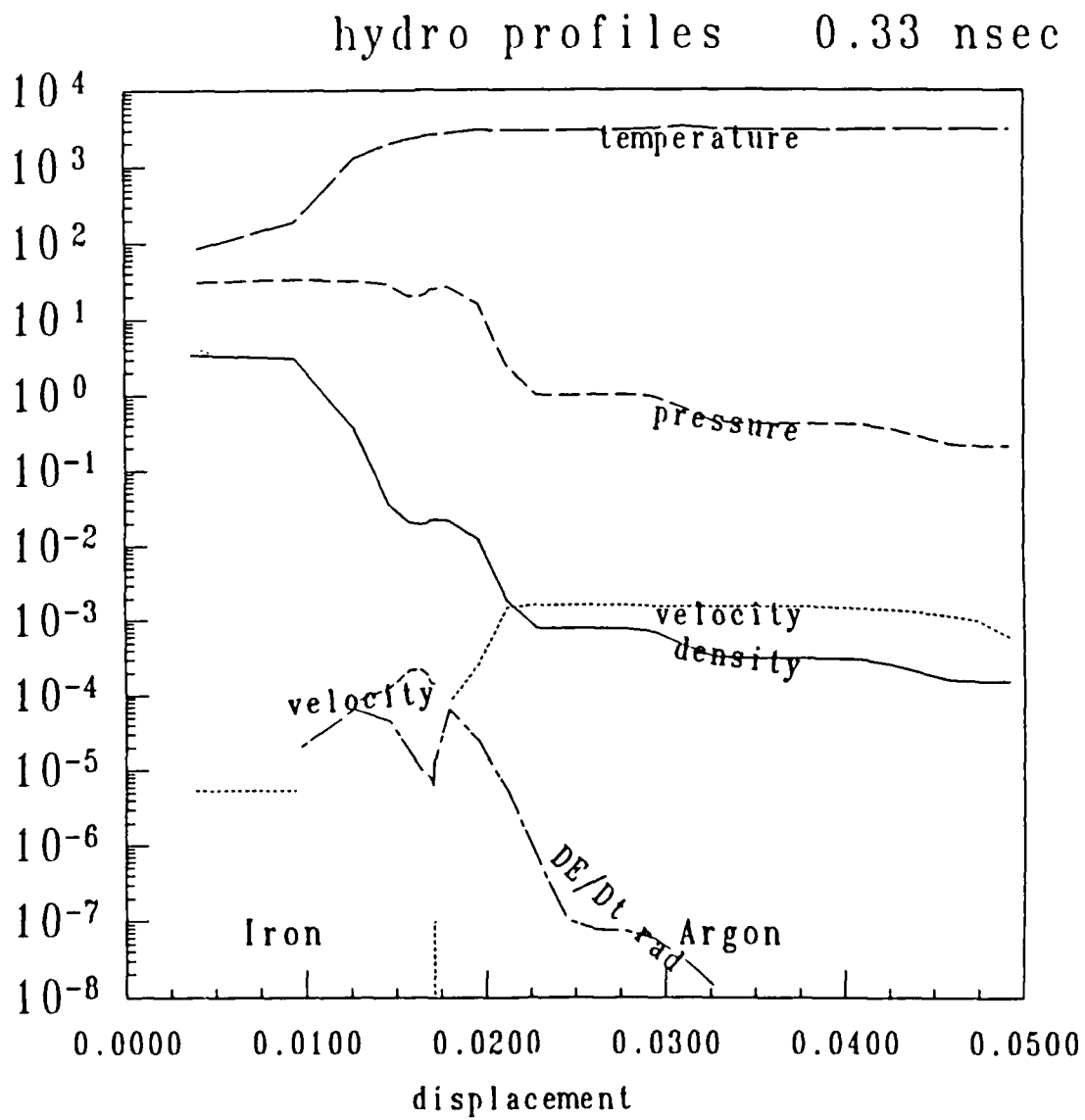|	Bound-Bound	Bound-Free	Free-Free	Total
0.0 - 0.1 keV	2.73×10^{9}	3.92×10^{8}	5.27×10^{11}	5.30×10^{11}
0.1 - 0.2 keV	9.02×10^{10}	3.30×10^{9}	3.85×10^{11}	4.79×10^{11}
0.2 - 0.4 keV	5.57×10^{11}	5.03×10^{11}	5.58×10^{11}	1.62×10^{12}
0.4 - 1.0 keV	8.82×10^{11}	6.39×10^{12}	1.19×10^{12}	8.47×10^{12}
1.0 - 2.0 keV	1.01×10^{13}	1.04×10^{13}	1.21×10^{12}	2.17×10^{13}
2.0 - 4.0 keV	2.13×10^{12}	2.80×10^{13}	1.06×10^{12}	3.12×10^{13}
above 4.0 keV	3.77×10^{12}	1.25×10^{13}	5.16×10^{11}	1.67×10^{13}
Total	1.75×10^{13}	5.77×10^{13}	5.45×10^{12}	8.07×10^{13}

Ideal–Gas Stagnation

density

Iron

Shocked
Argon

$1/3 \, u_0$

4:1

u_0 Argon Puff

z

$T = 1/3 \, m_i \, u_0^2$

Figure 1

energy history

Figure 2

Figure 3

(total) spectrum   ·0.33 nsec

Figure 4

LOG TEMPERATURE VERSUS TIME

$u_0 = 2.0 \times 10^8$ cm/sec

Time (nsec)

Displacement (cm)

4.0E+00
3.7E+00
3.3E+00
3.0E+00
2.6E+00
2.3E+00

1.7E+00
1.4E+00
1.0E+00
7.0E-01
3.5E-01
0.0E+00

Figure 5

Figure 6

log dErad/dt (J/nsec) vs TIME

$u_0 = 2.0 \times 10^8$ cm/sec

Figure 7

LOG DENSITY vs TIME

$u_0 = 2.0 \times 10^8$ cm/sec

Time (nsec)

4.0E+00
3.3E+00
2.6E+00
1.9E+00
1.2E+00
5.2E-01
-5.2E-01
-1.2E+00
-1.9E+00
-2.6E+00
-3.3E+00
-4.0E+00

Displacement (cm)

Figure 8

127

LOG TEMPERATURE VS TIME

Figure 9

LOG TEMPERATURE VS TIME

Time
(nsec)

$u_0 = 3.0 \times 10^8$ cm/sec

	4.0E+00
	3.7E+00
	3.3E+00
	3.0E+00
	2.6E+00
	2.3E+00
	1.7E+00
	1.4E+00
	1.0E+00
	7.0E-01
	3.5E-01
	0.0E+00

Displacement (cm)

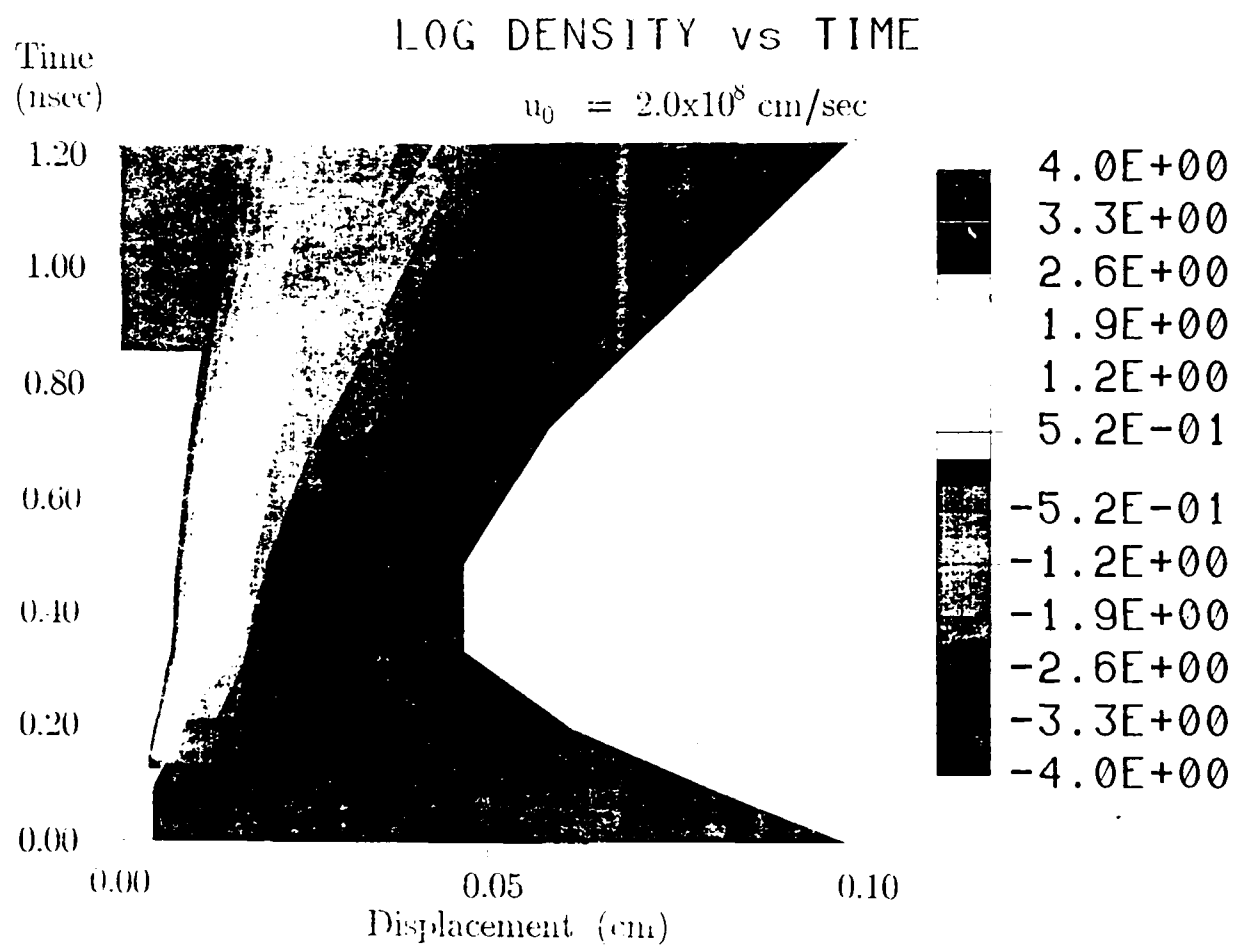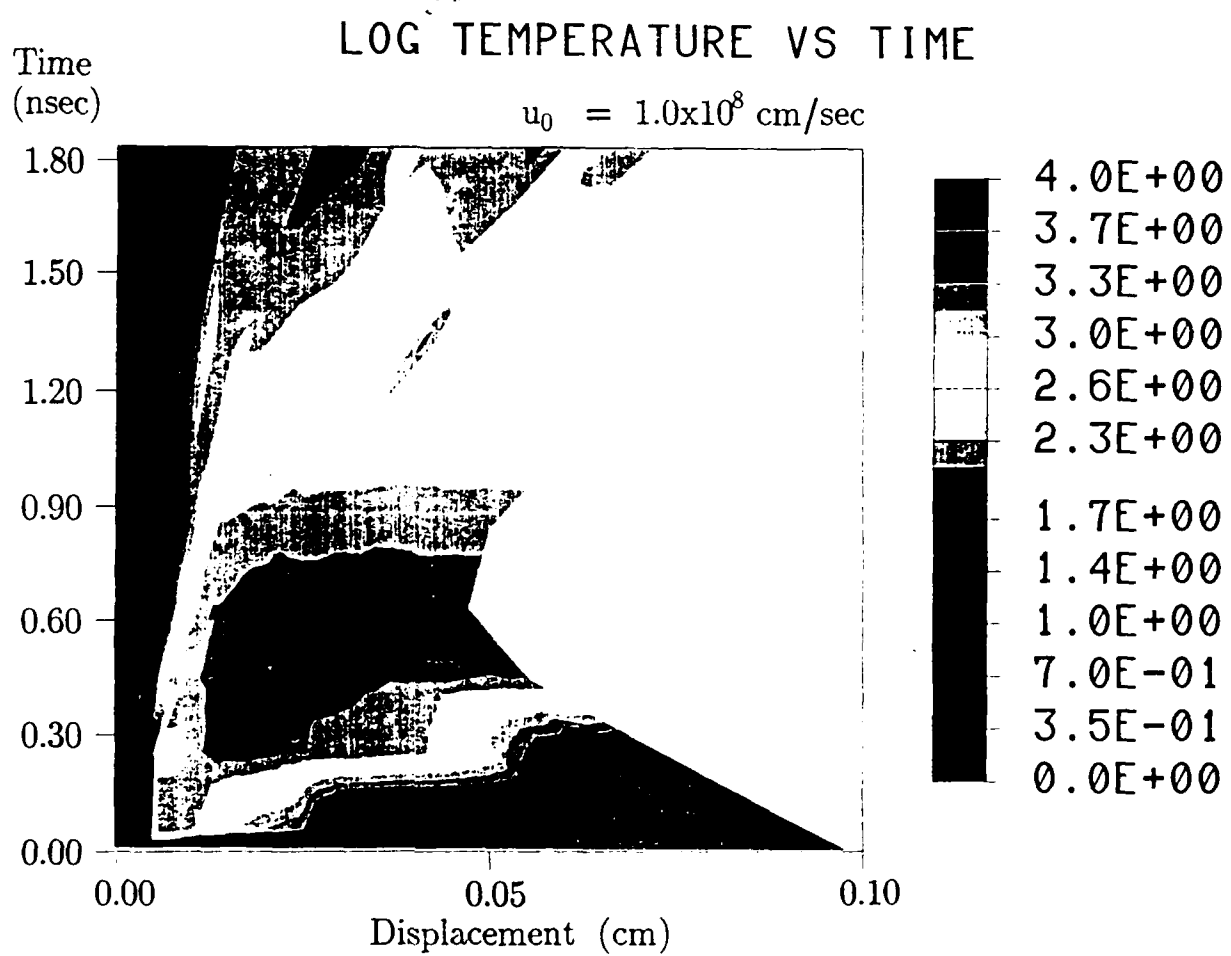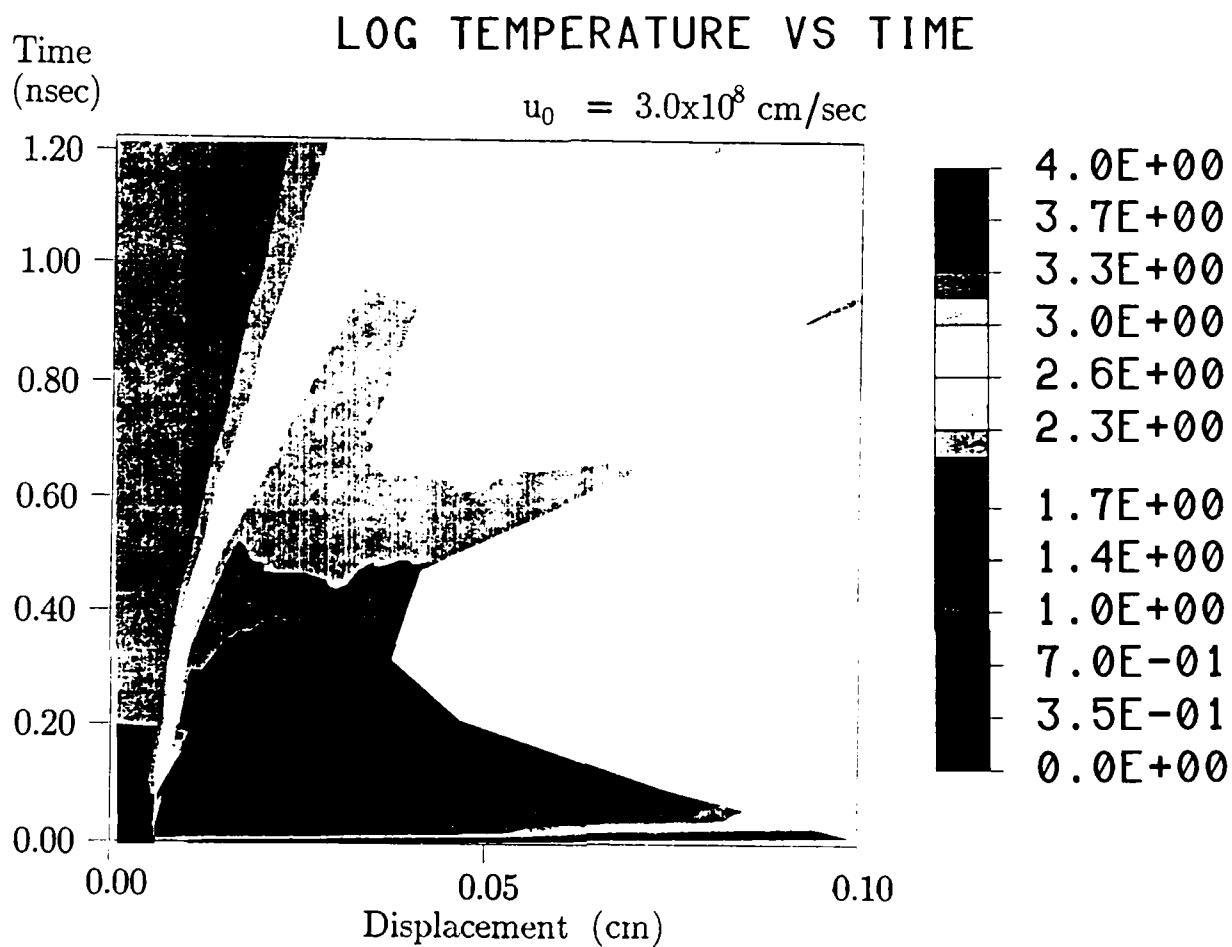**Figure 10**

c) Evolution of An X-Pinch Plasma

I. Introduction

The hot dense plasma that results from the passage of large currents through a Z-pinch plasma has attracted considerable attention in recent years as a radiation source for x-ray laser research, x-ray lithography applications, broadband x-ray flashlamp studies, and spectroscopy experiments[1]. The majority of experiments and theoretical investigations have been performed for the standard or conventional load designs such as single and multiple wires, gas puffs, metal foils, and more recently, metal vapors. With few exceptions almost all these loads exhibit unstable behavior during the implosion on axis. By altering the configuration to include an inner axial magnetic field or an inner cylindrical plasma localized along the axis, the m=0 instability can be inhibited. Both of these schemes tend to stabilize the implosion and have the effect of a stagnation post. However, the K-shell radiative efficiency of such configurations is somewhat reduced from, say, a single wire load even though the radiative cooling rate summed over all atomic shells is virtually the same for identical generator and load conditions[2]. For example, a single aluminum wire upon heating, first expands and subsequently runs-in and assembles on axis giving rise to a series of bright or hot spots. These hot spots are distributed along the axis and radiate intense short bursts of x-rays corresponding to temperatures and densities which are higher than the corresponding values associated with the bulk plasma. The assembled plasma achieves greater compressions leading to higher densities and smaller radii in the pinched regions than do the other types of load configurations such as wire arrays or gas puffs. Since the radiative cooling rate varies roughly as the density squared (for free streaming optically thin plasmas) multiplied by the characteristic radius of the spot squared, the K-shell radiative efficiency is also greater for single wires, all else being equal.

It is this behavior that has attracted our attention to the x-pinch configuration. Since the m=0 sausage instability occurs as a natural consequence of the implosion dynamics for conventional loads producing

130

enhanced temperatures and densities, a logical extension in load design would be to incorporate these features initially in order to take advantage of the higher temperatures and densities and, most importantly, improved radiative efficiency. In fact, the x-pinch configuration has been investigated experimentally for currents at the 100 kiloampere level and was found to behave as anticipated; the pinched region or neck was clearly distinguished in pinhole photographs as a localized spot of bright emission of thermal origin for the most part[3]. The measured size of the spot, based on small pinhole estimates, was about 10 μm. The spectrum revealed K-shell emissions from aluminum and L-shell emissions from nickel. Multiple copper x-pinch loads at higher current levels has also demonstrated K-shell emission[4].

In this paper we investigate the dynamics and radiative properties of an array of thin copper wires which are twisted in the center and configured to form an x-pinch. The dynamics are described by a 2-D non-LTE radiation magneto-hydrodynamics model (PRISM) coupled to an external driving current. The symmetry imposed by the r-z coordinates (i.e., the θ direction is ignored) requires that we model the problem after it has been assumed that the plasmas from the wires have merged and have the form rather like that of a hollow cone. Individual wires in the array, therefore, cannot be modeled as separate entities. The focus of this investigation is on the dynamic evolution and morphology of the plasma rather than the determination of an optimal design configuration for enhanced radiation efficiency or x-ray laser scenarios. It is our intent to gain a better understanding of these plasmas in order to compare and contrast the results in the future with experimental observations.

II. Model

The basic hydrodynamic quantities of mass, momentum, and total energy are transported using a Lagrangian scheme on a two-dimensional mesh. A remap phase using parabolic interpolation is then employed to update the variables on the original mesh. The dynamic evolution of the system is represented as solutions to the following equations:

continuity:

$$\frac{d\rho}{dt} = - \rho \, \underset{\sim}{\nabla} \cdot \underset{\sim}{u}$$

where

$$\frac{d}{dt} = \frac{\partial}{\partial t} + \underset{\sim}{u} \cdot \underset{\sim}{\nabla}$$

momentum:

$$\rho \frac{d\underset{\sim}{u}}{dt} = - \underset{\sim}{\nabla} \, (P_e + P_i + Q_A) + \frac{\underset{\sim}{J} \times \underset{\sim}{B}}{c}$$

Energy:
ion,

$$\frac{d\varepsilon_i}{dt} + (P_i + Q_A) \frac{dV}{dt} = - V \, \underset{\sim}{\nabla} \cdot \underset{\sim}{q}_i + V C_{ei} \cdot (T_e - T_i)$$

electrons,

$$\frac{d\varepsilon_e}{dt} + P_e \frac{dV}{dt} = - V \, \underset{\sim}{\nabla} \cdot \underset{\sim}{q}_e + V \, C_{ei} \, (T_i - T_e) - V \, P_{rad} + V \eta J^2$$

To these equations must be added Maxwell's equations, viz.

$$\underset{\sim}{\nabla} \times \underset{\sim}{B} = \frac{4\pi}{c} \, \underset{\sim}{J}$$

$$\underset{\sim}{\nabla} \times \underset{\sim}{E} = - \frac{1}{c} \, \frac{\partial \underset{\sim}{B}}{\partial t}$$

and Ohm's law,

$$\underset{\sim}{E} = \eta \, \underset{\sim}{J} - \frac{1}{c} \, \underset{\sim}{u} \times \underset{\sim}{B}$$

where $P_{i,e}$ = ion (electron) pressure, C_{ei} is the electron-ion energy exchange term, $\varepsilon_{i,e}$ = ion (electron) specific energy, ρ = density, $V = 1/\rho$, $u = (u_r, u_z)$ = velocity, q = heat flux, $[q = - K_{\|} \nabla T - K_{\perp} \nabla T - K_{\wedge} \, (e_B \times \nabla T)]$, ηJ^2 = ohmic heating, and P_{rad} = radiation power. The resistivity model of Spitzer[5] is used along with the relevant Braginskii transport coefficients[6]. The total current, I, is specified as a function of time and sets the outside boundary condition on the magnetic field according to $B_{\theta} = 2I/rc$. All other symbols have their conventional meaning. The pressure is determined from the equation of state, viz.

$$P = P(\rho, \varepsilon_{int})$$

where

$$\varepsilon_{int} = \varepsilon_{thermal} + \varepsilon_{ionization}$$

For example, in the case of a perfect gas

$$P = \rho \, \varepsilon_{thermal} / (\gamma - 1).$$

In our case (ρ, ε_{int}) are obtained from the above equations and are then used to evaluate P and T.

The atomic level populations in the plasma are determined by a set of rate equations of the form:

$$\frac{df_i}{dt} = \sum_j W_{ji} f_j - \sum_j W_{ij} f_i, \tag{1}$$

where f_i is the fractional population of atomic level i, and W_{ji} is the net reaction rate describing the transition from initial state j to final state i. An equation of this type is constructed for each of the atomic levels included in the model. For sufficiently dense plasmas, the effective populating and depopulating rates are generally fast compared with the hydrodynamic response. Under these circumstances, an equilibrium assumption, which involves dropping the explicit time dependence in Eq. (1), can be justified. The plasma is then said to be in collisional-radiative equilibrium (CRE), allowing the plasma ionization state to respond instantaneously to changes in hydrodynamic quantities.

The rate coefficients that are used to calculate the populating and depopulating rates, W_{ji}, are calculated using various atomic calculational methods. The processes included in this calculation and the methods used in calculating the corresponding rate coefficients are summarized elsewhere[7]. Once the set of rate equations (including the optical pumping from the radiation field) has been solved for the level populations, f_i, the electron density can be calculated.

$$N_e = \Sigma_i \ Z_i \ f_i \ N_I,$$

where Z_i is the ionic charge of level i and N_I is the total ion density.

The ionization and excitation energy can also be calculated by

$$\varepsilon_{Ionization} = \sum_i \ X_i \ f_i \ N_I,$$

where X_i is the energy of level i, measured from the ground state of the neutral atom. The copper model contains all the ground states from the neutral to the fully ionized state. In addition, there is excited state structure in the H-, He-, Li-, and Be-like ionization stages, containing 10 emission lines selected for their energetic and diagnostic value.

The local rate of energy change in zone j, a result of radiative processes, is given by

$$\dot{\varepsilon}_j = - \sum_p F_{pj}$$

where F_{pj} is the rate of energy loss in zone j resulting from a discrete radiative process (or frequency group) P, for each bound-bound, bound-free, and free-free process.

III. Results and Discussion

In the numerical simulations, we have assumed that the wires are vaporized and a plasma has been created which is symmetric around the z-axis with a conical cross-section. With this simplification, the 2-D simulation is carried out in the r-z plane. We have chosen, somewhat arbitrarily, a midplane density which is bounded at 0.075 cm in both r and z. The cone thickness is tapered to a thickness of 0.02 cm at r=0.3 cm and z=1.0 cm. The same conditions exist in the other three quarter planes. The total length in the z-direction (i.e., the

diode length) is then 2 cm. We have examined cases in which either the mass per unit length along z or the density within the cone is taken to be uniform. The latter case can be used to model, for instance, an etched or tapered wire array. In this section we consider only cases with an initial constant density. The density and radius are chosen to correspond to an initial array of copper wires twisted at the center. Outside of this region, the density is set to a floor which is typically less than 1% of the central interior value.

A. Hydrodynamic Simulations

We first examine the phenomenology of an x-pinch implosion with a simulation in which there are no radiative loss terms. Figure 1 shows the initial density contours over the half-plane z=0 to z=1.0 cm. In this example we have chosen an initial uniform density of 4×10^{-2} gm/cm^3 and an initial electron temperature of 30 eV. The initial ion internal energy is chosen to be a factor of ten below the electron internal energy. An external current is applied as a boundary condition on rB_θ and is chosen to rise to 5 MA in 25 nsec. In this simulation we have used the equation of state tables, SESAME, for copper[8]. The mesh resolution is 124 in the z-direction and 74 in the r-direction on the quarter-plane. The values on the opposite quarter plane in the contour plots are determined from symmetry arguments.

Figure 2 shows the density contours at 10, 14, 18, and 26 nsec. The calculation is terminated after 26 nsec when plasma has been pushed up against the top wall which is located at 1 cm. At 10 nsec, the density contours indicate that there is plasma motion up the z-axis as a result of the stagnation of the inside part of the cone on axis. By 14 nsec the peak density has been localized in a spot which is above the r-axis. This spot has moved further up the axis by 18 nsec, and further still at the last frame, 26 nsec. Figure 3 displays logarithmic electron temperature and density curves along the z-axis. The frames are at the same times as shown in Fig. 2. The peak density is seen to move up the z-axis. A cavity or low density region evolves behind the peak density due to material being pushed away from the x-point. The back edge of this spot (as seen in Fig. 2(c)) has reached an electron temperature of 1 keV

while the bulk of the spot has a temperature of approximately 100 eV. This gradient eventually diffuses through the high density region and the entire spot is roughly 200 eV at 18 nsec. In the last frame of this Figure, the temperature has again risen above the keV level in the underdense cavity behind the peak density. This is a result of material being compressed into this region and the plasma attempting to establish equilibrium. A low density foot has arrived at the upper wall at this time and the simulation is subsequently terminated.

B. Radiation Hydrodynamic Simulations

We have investigated different mass loadings or equivalently, wire diameters for the generic design discussed above (i.e., a tapered cone which intersects the r- and z-axis at 0.075 cm, and a 0.02 cm width at r = 0.3 cm and z = 1.0 cm) but with radiation loss terms included. In these simulations, we make use of an atomic model for Copper which contains all the ground states as well as structure for the H-, He-, Li-, and Be-like ionization stages. Ten transitions (lines) within each of these stages, as well as the bound free edges for all excited and ground states are carried. The radiated power which includes the bound-bound, bound-free, and free-free components is then used to calculate a total radiated power for each computational zone. Internal energy is partitioned into ionization and thermal components so that electron temperature and pressure are self-consistently calculated. These quantities are then used instead of those obtained from the SESAME tables as in the previous section. The ions are treated as a fluid with $\gamma=5/3$. The large amount of memory and computational time required for this model dictates that we limit ourselves to a mesh of size 35 x 60. Here, we do not consider radiation transport with the proviso that the maximum power output from a given zone is limited to a fraction of the Blackbody limit. This limiter is usually set to 0.1.

We have considered four different mass densities in the cone: 2×10^{-2}, 4×10^{-2}, 8×10^{-2}, and 12×10^{-2} gm/cm^3. In the following discussion we again concentrate on the case where the initial density is 4×10^{-2} gm/cm^3. Figure 4 shows density contours at 8, 14, 16, and 18 nsec. These plots show qualitatively the same behavior as seen in Fig. 2 with motion of a dense spot along the z-axis. However, multiple spot formation can be seen near the origin

as evidenced by the contours at 16 nsec. In the SESAME hydro only simulation, the dense spot moved up the axis and left a cavity behind. In this case, a dense region reforms near the origin so that by 18 nsec there are two distinct dense regions which can be seen. Other, less dense regions have also formed along the outside of the cone. The foot in front of the dense region also extends further up the z-axis than in the hydro only run and contacts the upper wall shortly after 18 nsec.

The logarithm of the radiated power is shown in Fig. 5 at 8, 14, 16, and 18 nsec. In the first frame, 8 nsec, the highest levels of radiated power occurs near the outside of the pinch plasma in the region of the x-point. Radiation is also coming from material which is being pushed up the axis. The low outside material density combined with the high current density in this region tends to produce ohmic heating levels which initially dominate the radiation. Although current is continuously diffusing towards the axis, the current density remains highest on the outside while the total current is increasing. This contributes substantial ohmic heating and radiative power. As the pinch develops further, at 14 and 16 nsec, the radiated power is maximized on the outside of the dense spots seen in the density contours of Fig. 4. At 18 nsec, the upper and lower dense regions of Fig. 4(d) are seen to be radiating most strongly. The location of the upper region is at approximately the same position as the upper dense region shown in Fig. 2(d) and Fig. 4(d). The bottom region represents a large, radiating hot spot located at the x-point.

The total radiated line energy as a function of initial x-pinch density is shown in Fig. 6. At the two lowest densities, 2×10^{-2} gm/cm^3 and 4×10^{-2} gm/cm^3 (which would correspond to an array of four, 41.5 μm and 83 μm diameter copper wires respectively) the yield is roughly about a kilojoule in all lines and falls to about 150 J at the highest density of 12×10^{-2} gm/cm^3. The yield for the lines above 8 keV in energy (i.e., K-shell lines) are 45 J for the 2×10^{-2} gm/cm^3 and 13 J for the 4×10^{-2} gm/cm^3 case. This drops below 10 J for the higher densities or equivalently, larger wire diameter arrays. In contrast to this, the bound-free continuum contribution (i.e., from all ground states as well as the excited states) to the radiative yield was 32 kJ for the 4×10^{-2} gm/cm^3 simulation. All yield values were calculated up to 18 nsec when the

calculations were terminated because of material interacting with the upper wall. It should also be recognized that the yield values given above and shown in Fig. 6 are approximate since initial starting conditions, x-pinch configuration, mass loadings, etc. can change these values. For instance, lowering the initial ion internal energy by a factor of ten in the 2×10^{-2} gm/cm^3 case produces a slightly harder stagnation and increased the K-shell yield by about 50% although the total yield decreased somewhat.

The radiation power spectrum from the 4×10^{-2} gm/cm^3 x-pinch simulation at 18 nsec is shown in Fig. 7. The energy scale runs from 200 eV to 12 keV. The logarithm of the power runs over six orders of magnitude. Line broadening due to ion thermal motion has been included in this Figure. However, no instrumental broadening has been assumed. The dominant lines below 2 keV are from the Li- and Be-like stages. The weaker higher energy lines from the K-shell (He-α, Ly-α, He-β, and Ly-β) are located around 10 keV.

IV. Conclusion

The evolution of an x-pinch has been studied from the context of a single generic configuration. We concentrated on the dynamics of the x-pinch and not on an optimization study. We have found that an array of wires twisted to form an x-pinch results in the formation of a hot spot or jet which moves up the z-axis. In the case which was presented here, a hot spot was also produced near the x-point. Radiated power was concentrated in the moving spot as well as in the central hot spot. Some Cu K-shell emission (<100 J) was also produced.

A more exhaustive study will have to be conducted in order to determine the importance of changing the current pulse, wire loading (e.g., tapering), wire mass, wire material, and x-point angle to the improvement or degradation of the results reported on here.

References

1. N. R. Pereira and J. Davis, J. Appl. Phys. 64, R1 (1988); and references therein.

2. R. W. Clark, J. Davis, and F. L. Cochran, Phys. Fluids 29, 1971 (1986).

3. S. M. Zakharov, G. V. Iavankov, A. A. Kolomenskii, S. A. Pikuz, and A. I. Samokhin, Sov. J. Plasma Phys. 13, 115 (1987).

4. N. Loter, personal communication (1988).

5. L. Spitzer, Jr., Physics of Fully Ionized Gases (Interscience, New York, 1962).

6. S. I. Braginskii, Reviews of Plasma Physics, Vol. 1 (Consultants Bureau, New York, 1965), p. 205.

7. D. Duston and J. Davis, Phys. Rev. A 24, 1505 (1981).

8. B. I. Bennet, J. D. Johnson, G. I. Kerley, and G. T. Rood, Los Alamos National Laboratory Report No. LA-7130, 1978.

Figure Captions

1. Initial configuration for an initially uniform 4×10^{-2} gm/cm^3 x-pinch.

2. Density contours at various times. Eight equally and linearly spaced contours are shown. (a) 10 nsec and peak density of 8.7×10^{-2} gm/cm^3. (b) 14 nsec and peak density of 3.45×10^{-1} gm/cm^3. (c) 18 nsec and peak density of 1.85×10^{-1} gm/cm^3. (d) 26 nsec and peak density of 3×10^{-1} gm/cm^3.

3. Logarithmic temperature and density curves along the z-axis. (a) 0 nsec, (b) 10 nsec, (c) 14 nsec, (d) 18 nsec, and (e) 26 nsec.

4. Density contours as in Fig. 2 but for an initially uniform 4×10^{-2} gm/cm^3 x-pinch simulation in which radiation loss terms are included. (a) 8 nsec and peak density of 6.25×10^{-2} gm/cm^3. (b) 14 nsec and peak density of 7.4×10^{-2} gm/cm^3. (c) 16 nsec and peak density of 1.7×10^{-1} gm/cm^3. (d) 18 nsec and peak density of 8×10^{-2} gm/cm^3.

5. Logarithmic radiation power (ergs/sec-cm^3) contours for the times shown in Fig. 4. Each plot ranges over 8 contours with 3 contours per decade. The highest possible value in (a) is 4.6×10^{21} ergs/sec-cm^3 and 4.6×10^{22} ergs/sec-cm^3 in (b), (c), and (d).

6. Total line radiation as a function of initial density.

7. Instantaneous radiation power (ergs/sec-keV) spectrum as a function of photon energy at 18 nsec.
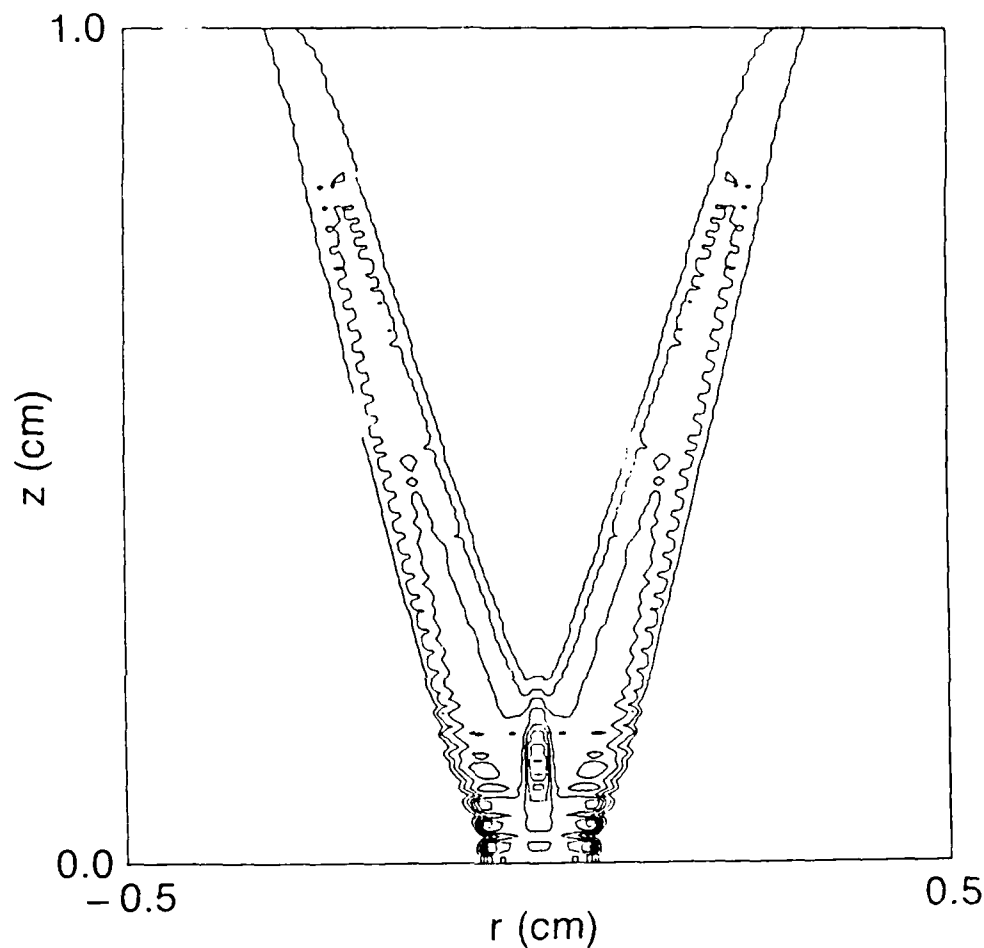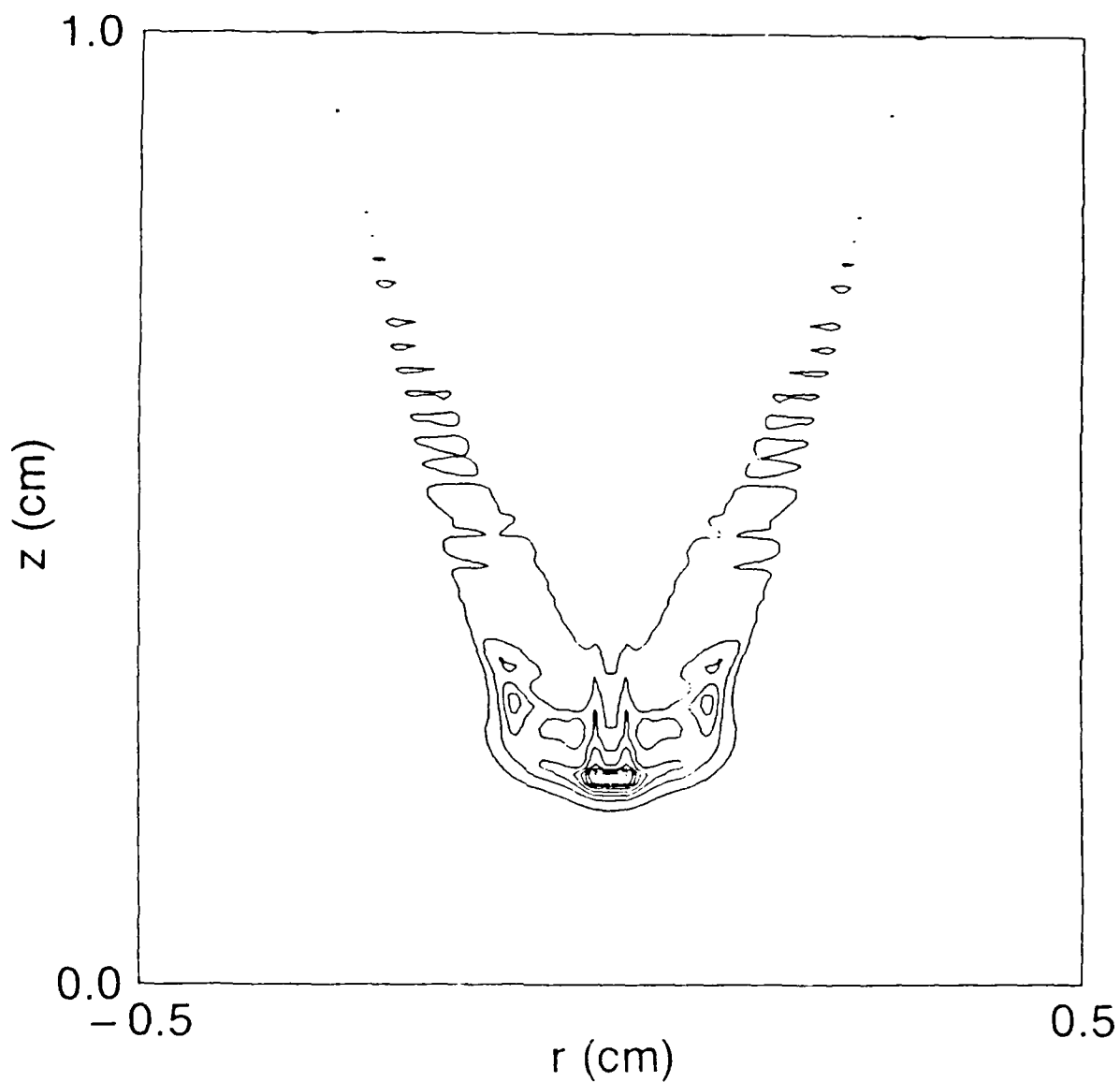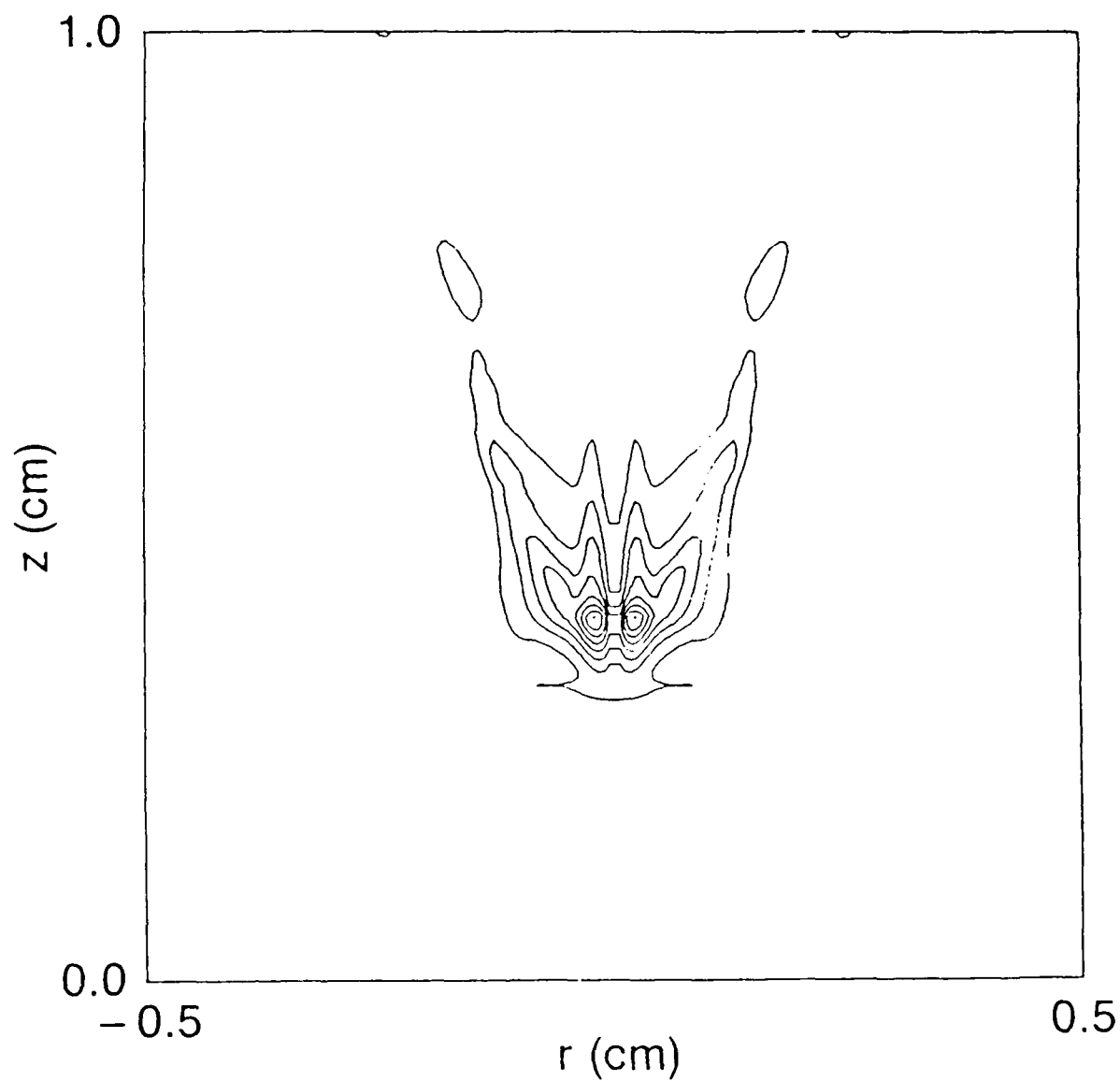
(a)

Fig. 2 — Density contours at various times. Eight equally and linearly spaced contours are shown. (a) 10 nsec and peak density of 8.7×10^{-2} gm/cm^3. (b) 14 nsec and peak density of 3.45×10^{-1} gm/cm^3. (c) 18 nsec and peak density of 1.85×10^{-1} gm/cm^3. (d) 26 nsec and peak density of 3×10^{-1} gm/cm^3.
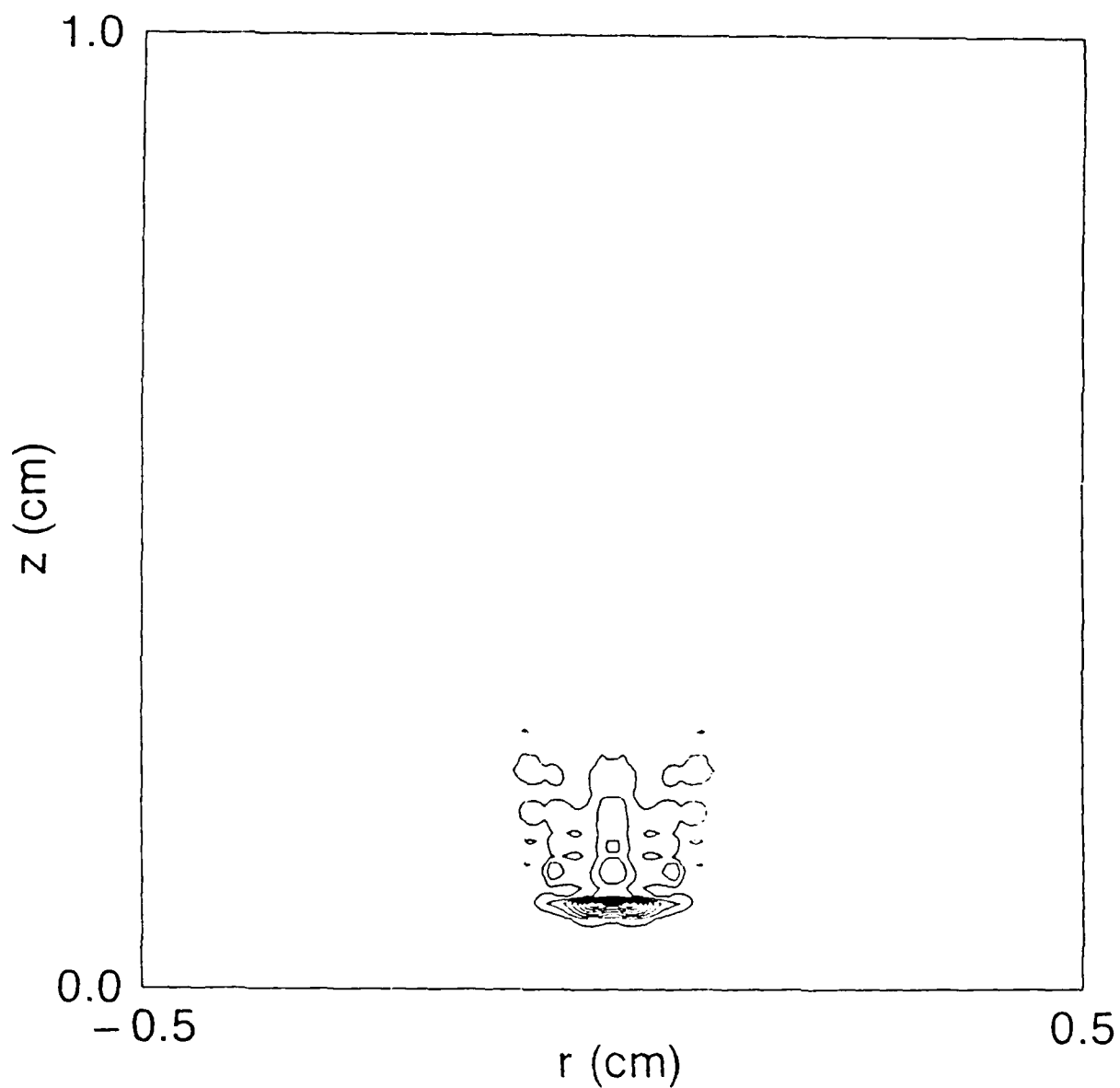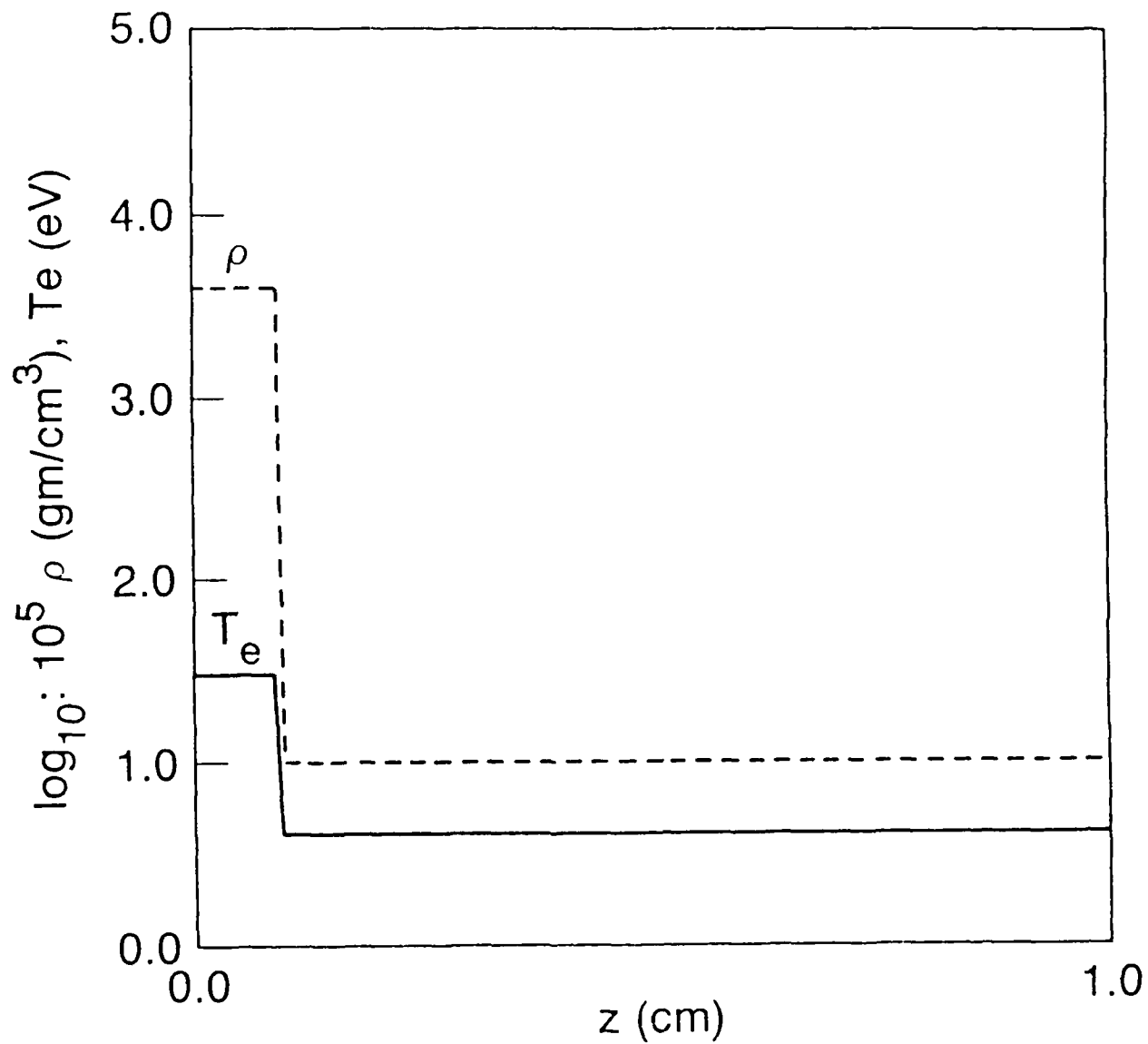
(b)

Fig. 2 (Continued) — Density contours at various times. Eight equally and linearly spaced contours are shown. (a) 10 nsec and peak density of 8.7×10^{-2} gm/cm^3. (b) 14 nsec and peak density of 3.45×10^{-1} gm/cm^3. (c) 18 nsec and peak density of 1.85×10^{-1} gm/cm^3. (d) 26 nsec and peak density of 3×10^{-1} gm/cm^3.

(c)

Fig. 2 (Continued) — Density contours at various times. Eight equally and linearly spaced contours are shown. (a) 10 nsec and peak density of 8.7×10^{-2} gm/cm^3. (b) 14 nsec and peak density of 3.45×10^{-1} gm/cm^3. (c) 18 nsec and peak density of 1.85×10^{-1} gm/cm^3 (d) 26 nsec and peak density of 3×10^{-1} gm/cm^3.

(d)

Fig. 2 (Continued) — Density contours at various times. Eight equally and linearly spaced contours are shown. (a) 10 nsec and peak density of 8.7×10^{-2} gm/cm^3. (b) 14 nsec and peak density of 3.45×10^{-1} gm/cm^3. (c) 18 nsec and peak density of 1.85×10^{-1} gm/cm^3. (d) 26 nsec and peak density of 3×10^{-1} gm/cm^3.

Fig. 3 — Logarithmic temperature and density curves along the z-axis.
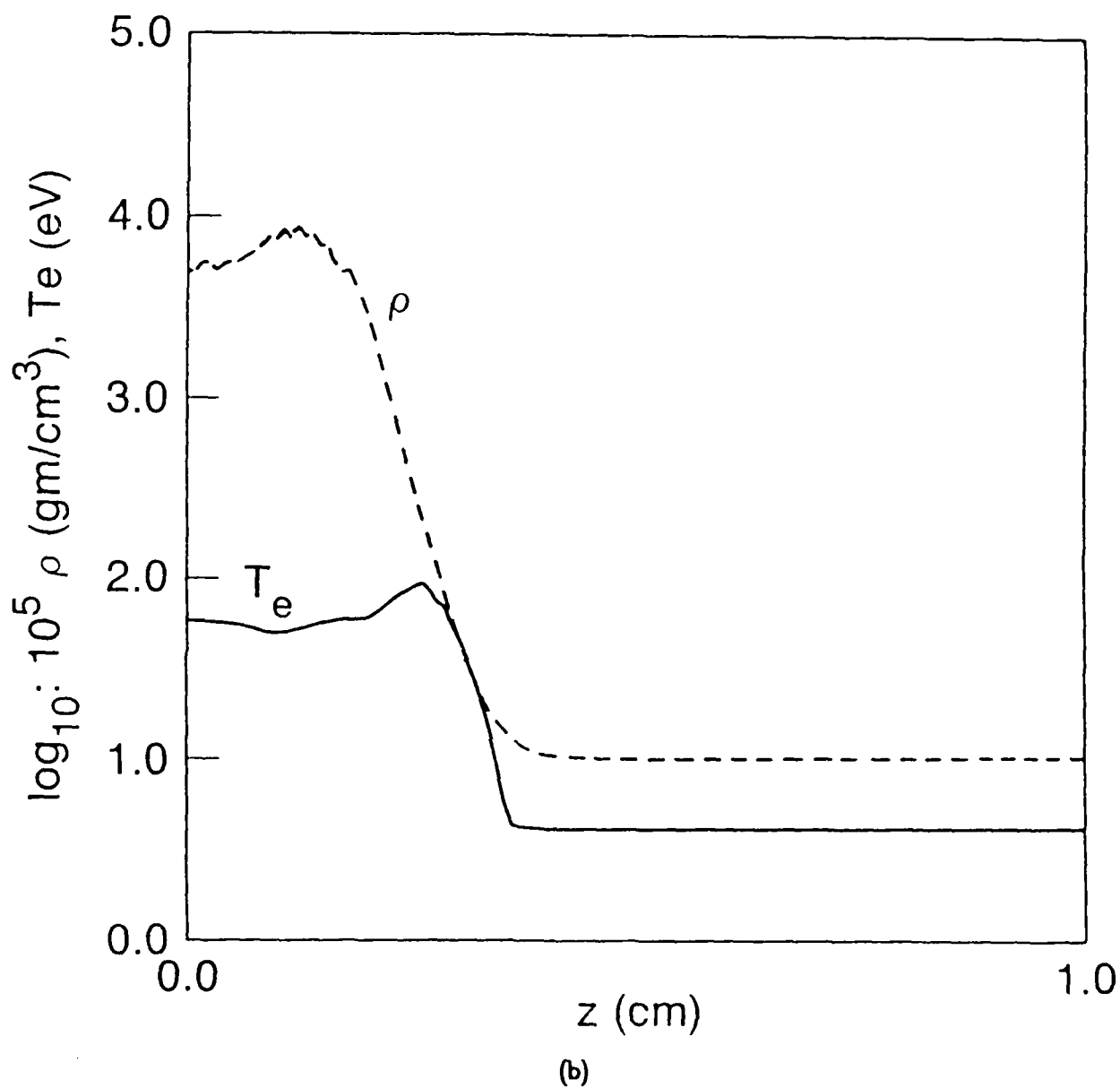(a) 0 nsec, (b) 10 nsec, (c) 14 nsec, (d) 18 nsec, and (e) 26 nsec.

Fig. 3 (Continued) — Logarithmic temperature and density curves along the z-axis.
(a) 0 nsec, (b) 10 nsec, (c) 14 nsec, (d) 18 nsec, and (e) 26 nsec.

146

Fig. 3 (Continued) — Logarithmic temperature and density curves along the z-axis.
(a) 0 nsec, (b) 10 nsec, (c) 14 nsec, (d) 18 nsec, and (e) 26 nsec.

Fig. 3 (Continued) — Logarithmic temperature and density curves along the z-axis.
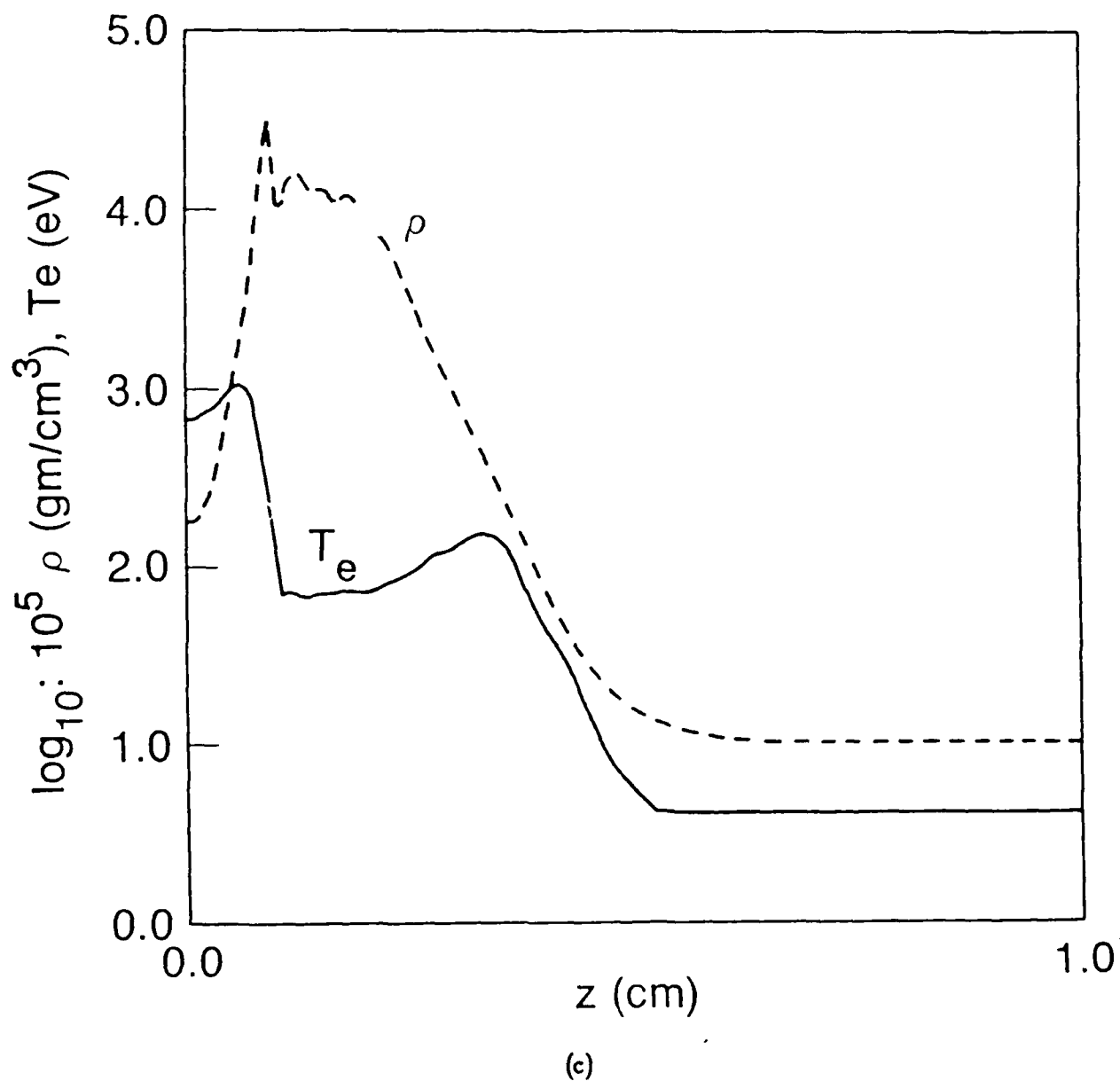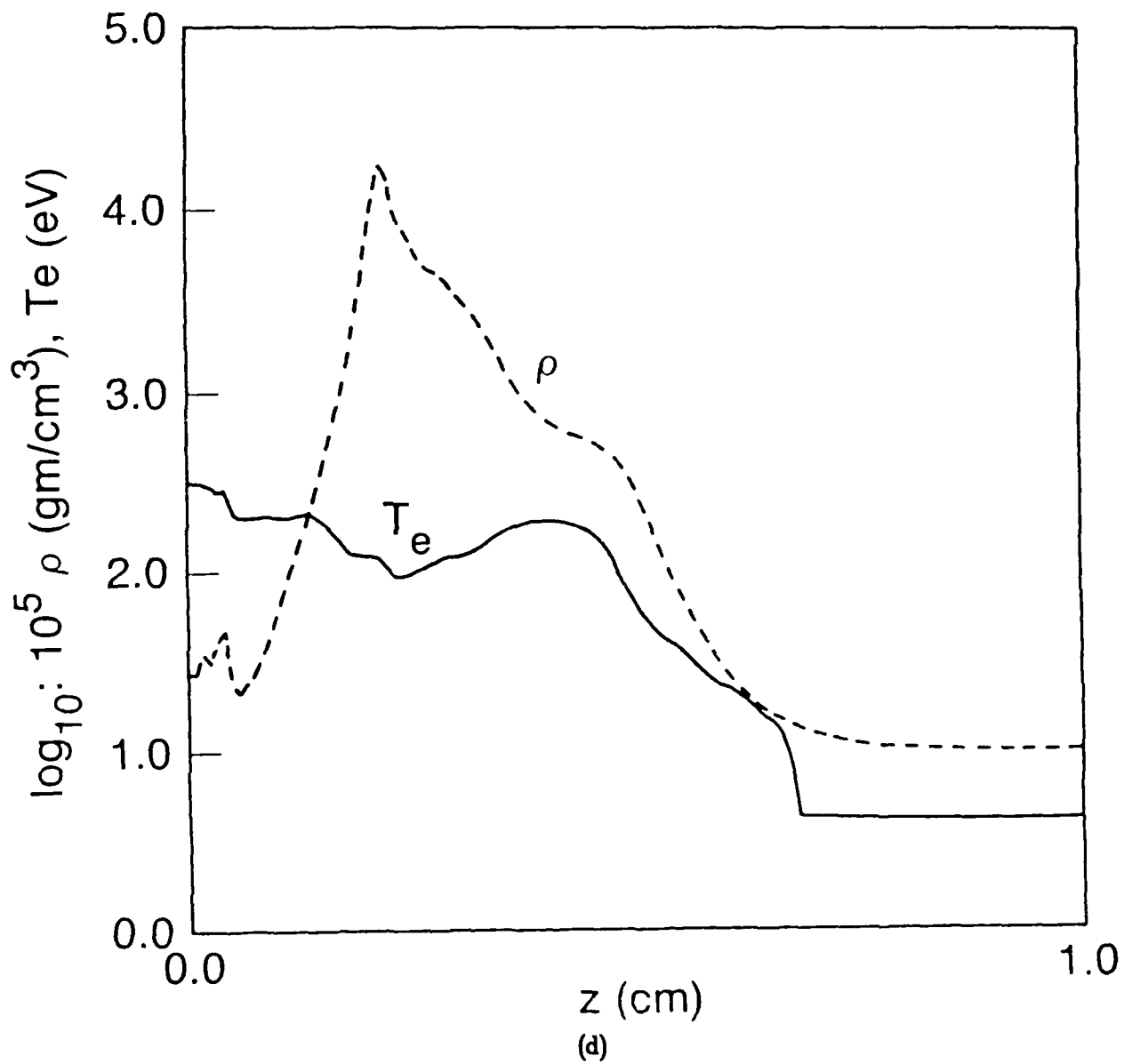(a) 0 nsec, (b) 10 nsec, (c) 14 nsec, (d) 18 nsec, and (e) 26 nsec.

148
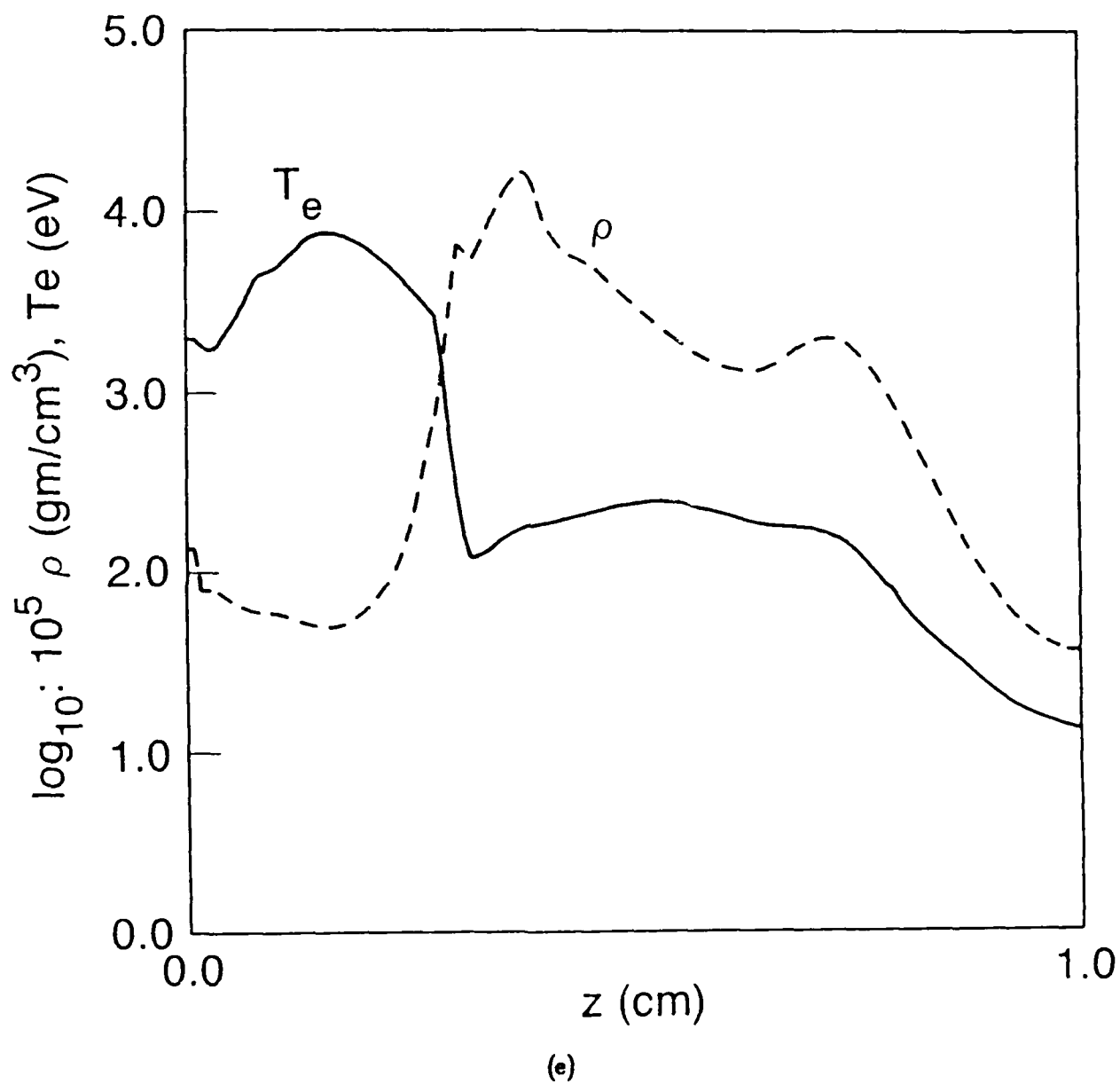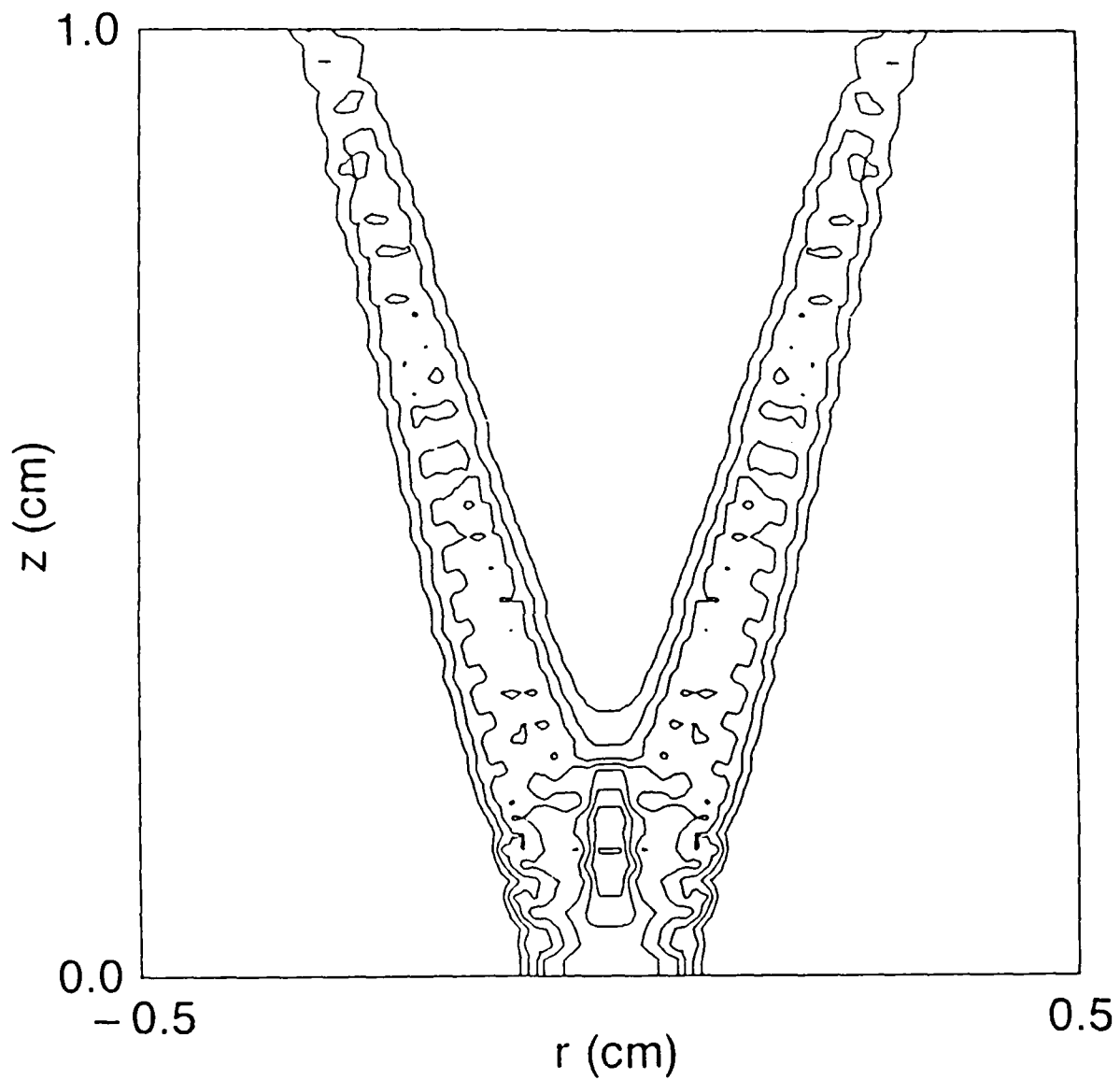
Fig. 3 (Continued) — Logarithmic temperature and density curves along the z-axis.
(a) 0 nsec, (b) 10 nsec, (c) 14 nsec, (d) 18 nsec, and (e) 26 nsec.

(a)

Fig. 4 — Density contours as in Fig. 2 but for an initially uniform 4×10^{-2} gm/cm^3 x-pinch simulation in which radiation loss terms are included. 8 nsec and peak density of 6.25×10^{-2} gm/cm^3. (b) 14 nsec and peak density of 7.4×10^{-2} gm/cm^3. (c) 16 nsec and peak density of 1.7×10^{-1} gm/cm^3. (d) 18 nsec and peak density of 8×10^{-2} gm/cm^3.
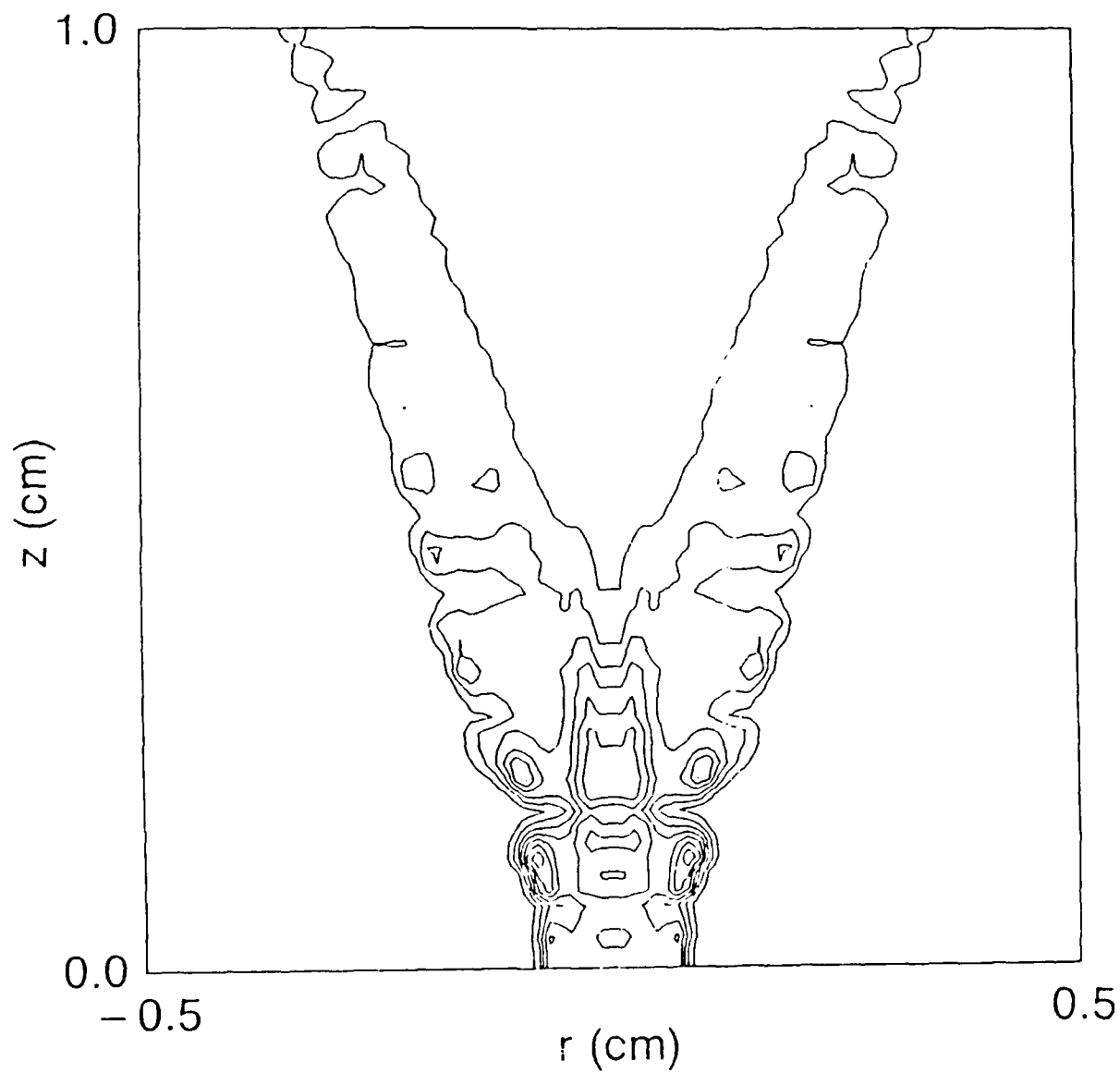
Fig. 4 (Continued) — Density contours as in Fig. 2 but for an initially uniform 4×10^{-2} gm/cm^3 x-pinch simulation in which radiation loss terms are included. 8 nsec and peak density of 6.25×10^{-2} gm/cm^3. (b) 14 nsec and peak density of 7.4×10^{-2} gm/cm^3. (c) 16 nsec and peak density of 1.7×10^{-1} gm/cm^3. (d) 18 nsec and peak density of 8×10^{-2} gm/cm^3.

(c)

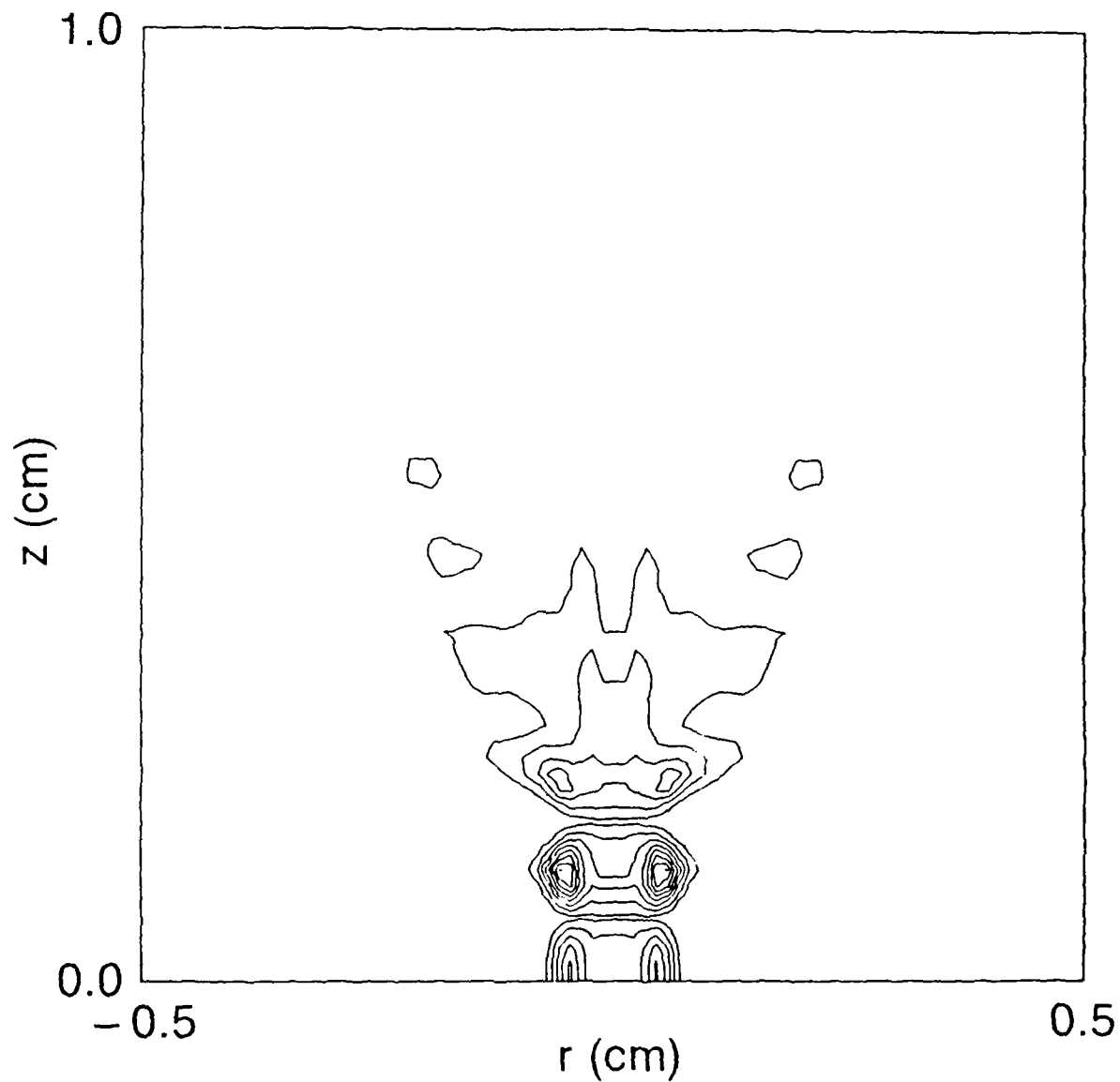Fig. 4 (Continued) — Density contours as in Fig. 2 but for an initially uniform 4×10^{-2} gm/cm^3 x-pinch simulation in which radiation loss terms are included. 8 nsec and peak density of 6.25×10^{-2} gm/cm^3. (b) 14 nsec and peak density of 7.4×10^{-2} gm/cm^3. (c) 16 nsec and peak density of 1.7×10^{-1} gm/cm^3. (d) 18 nsec and peak density of 8×10^{-2} gm/cm^3.
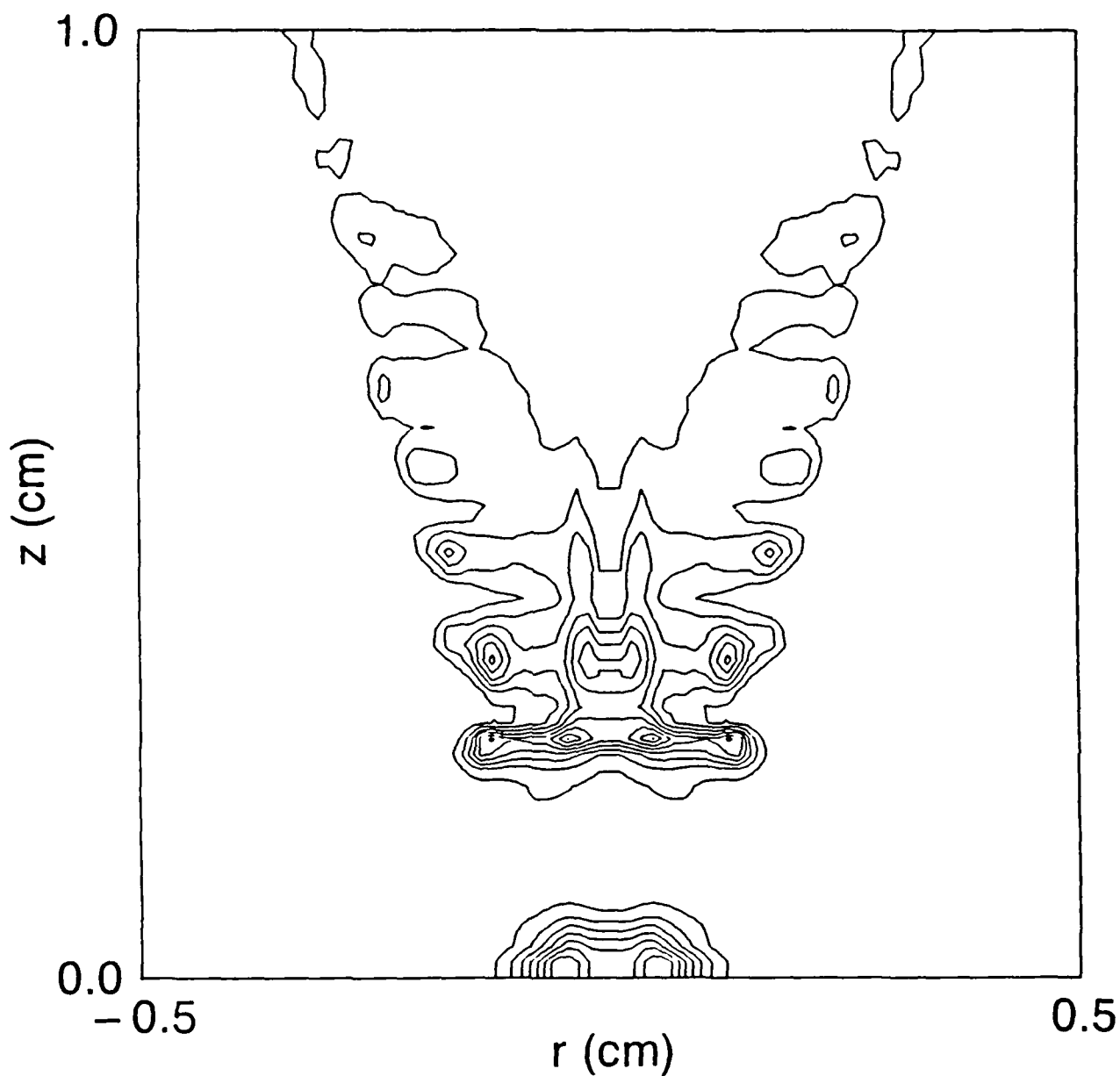
(d)

Fig. 4 (Continued) — Density contours as in Fig. 2 but for an initially uniform 4×10^{-2} gm/cm³ x-pinch simulation in which radiation loss terms are included. 8 nsec and peak density of 6.25×10^{-2} gm/cm³. (b) 14 nsec and peak density of 7.4×10^{-2} gm/cm³. (c) 16 nsec and peak density of 1.7×10^{-1} gm/cm³. (d) 18 nsec and peak density of 8×10^{-2} gm/cm³.

153

Fig. 5 — Logarithmic radiation power (ergs/sec-cm^3) contours for the times shown in Fig. 4. Each plot ranges over 8 contours with 3 contours per decade. The highest possible value in (a) is 4.6 × 10^{21} ergs/sec−cm^3 and 4.6 × 10^{22} ergs/sec−cm^3 in (b), (c), and (d).

1.0

z (cm)

0.0
−0.5   0.5

r (cm)

(b)

Fig. 5 (Continued) — Logarithmic radiation power (ergs/sec-cm^3) contours for the times shown in Fig. 4. Each plot ranges over 8 contours with 3 contours per decade. The highest possible value in (a) is 4.6×10^{21} ergs/sec− cm^3 and 4.6×10^{22} ergs/sec− cm^3 in (b), (c), and (d).

Fig. 5 (Continued) — Logarithmic radiation power (ergs/sec-cm^3) contours for the times shown in Fig. 4. Each plot ranges over 8 contours with 3 contours per decade. The highest possible value in (a) is 4.6×10^{21} ergs/sec−cm^3 and 4.6×10^{22} ergs/sec−cm^3 in (b), (c), and (d).

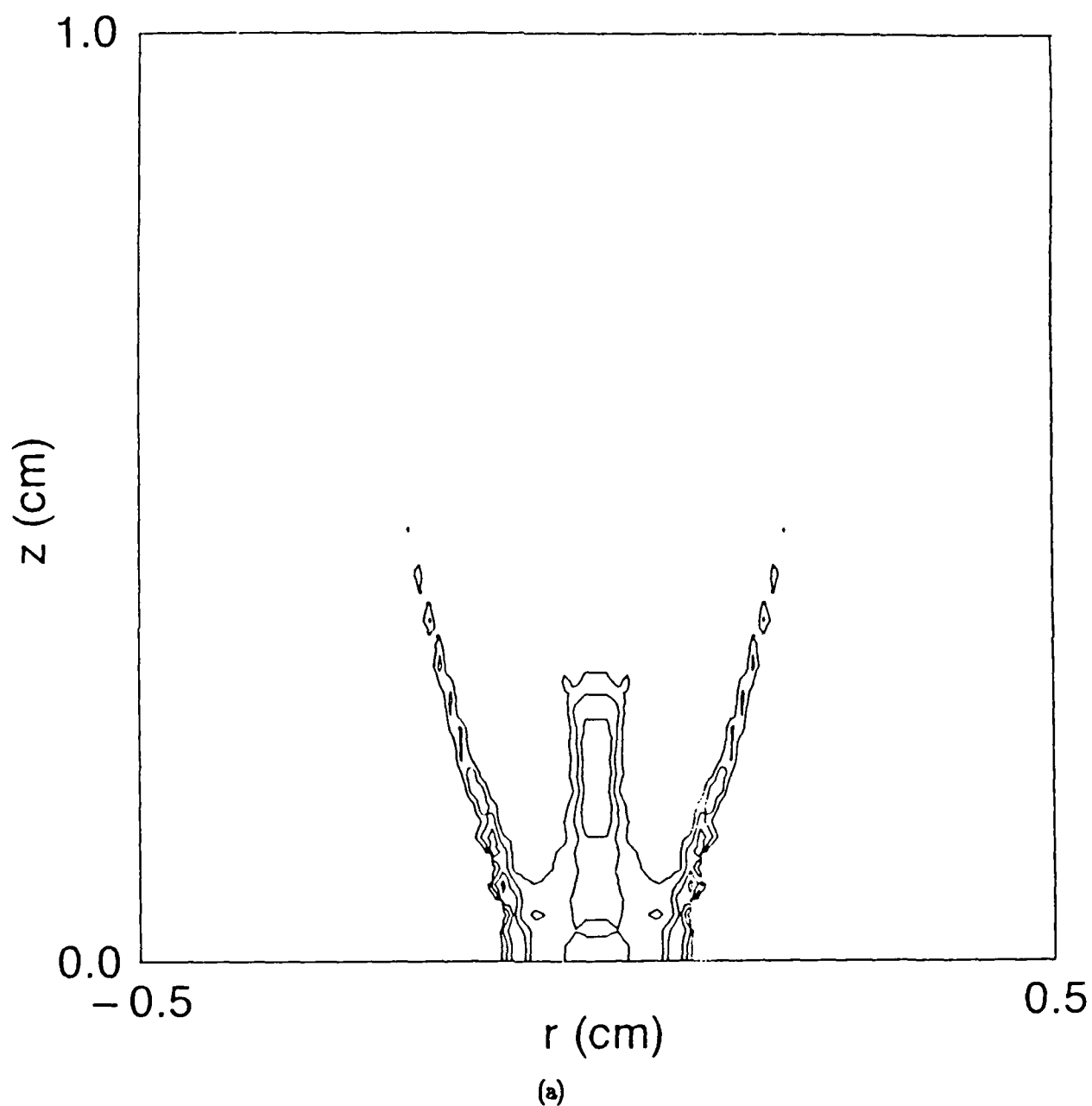Fig. 5 (Continued) — Logarithmic radiation power (ergs/sec-cm^3) contours for the times shown in Fig. 4. Each plot ranges over 8 contours with 3 contours per decade. The highest possible value in (a) is 4.6 × 10^{21} ergs/sec– cm^3 and 4.6 × 10^{22} ergs/sec– cm^3 in (b), (c), and (d).
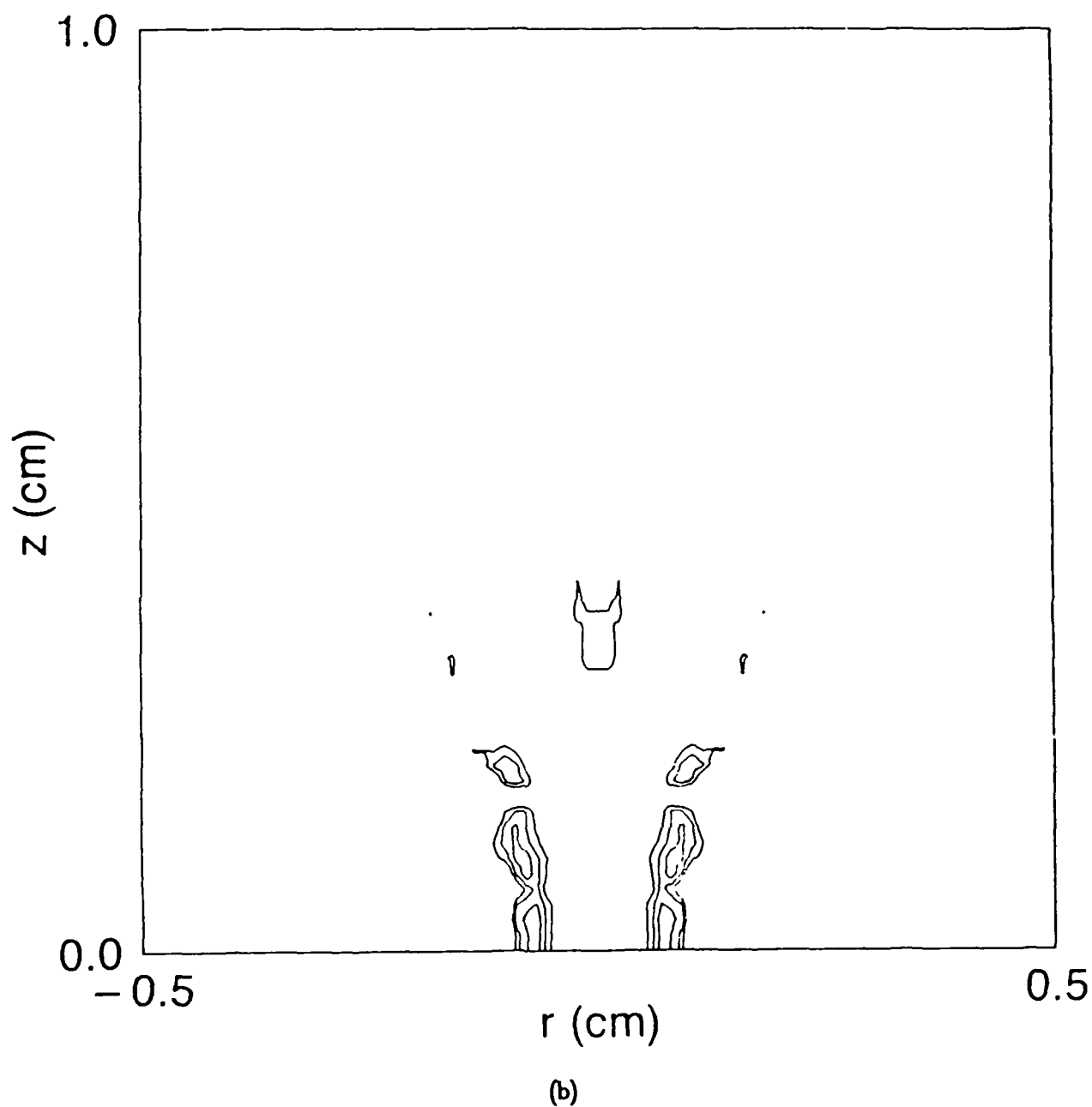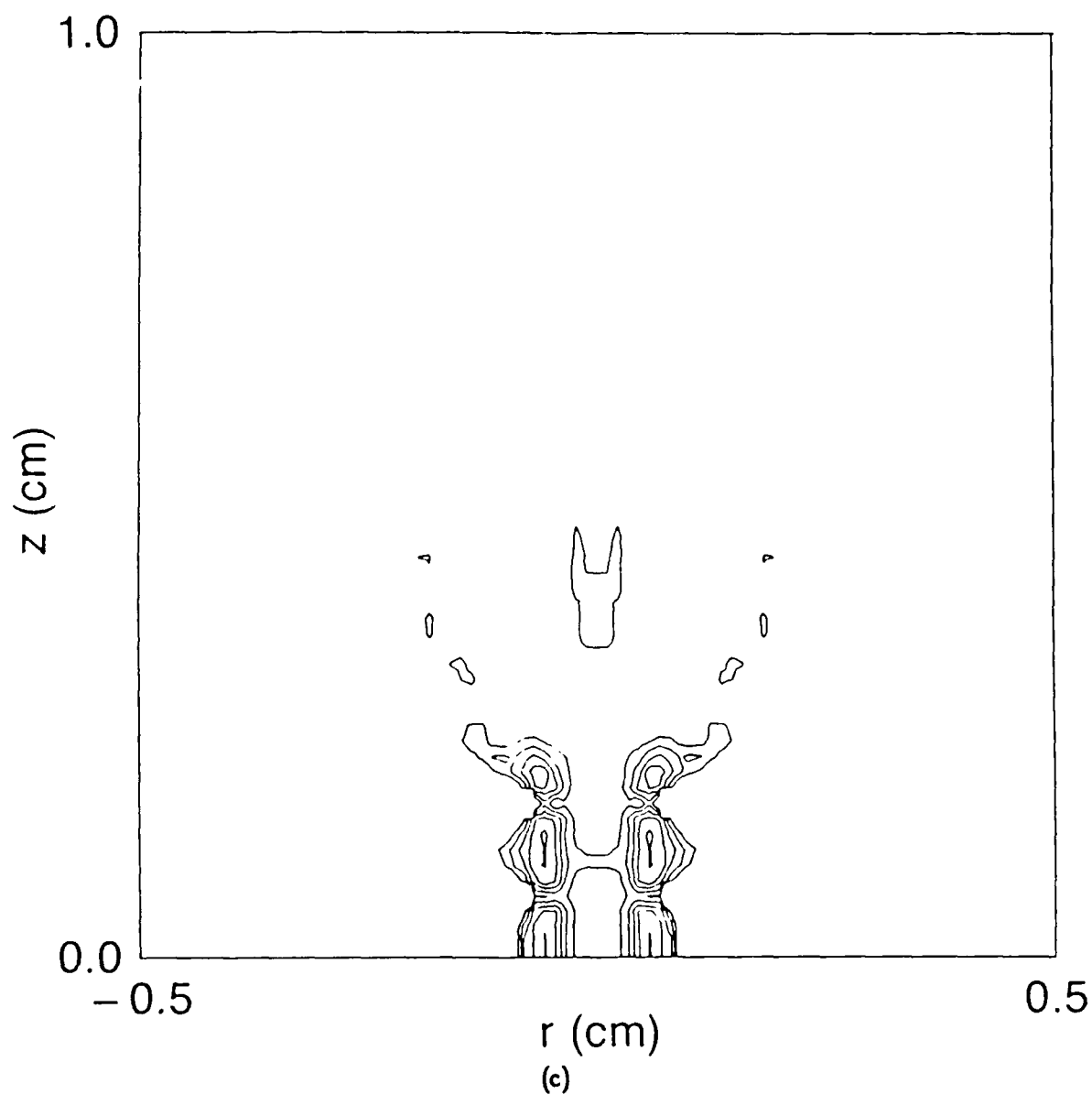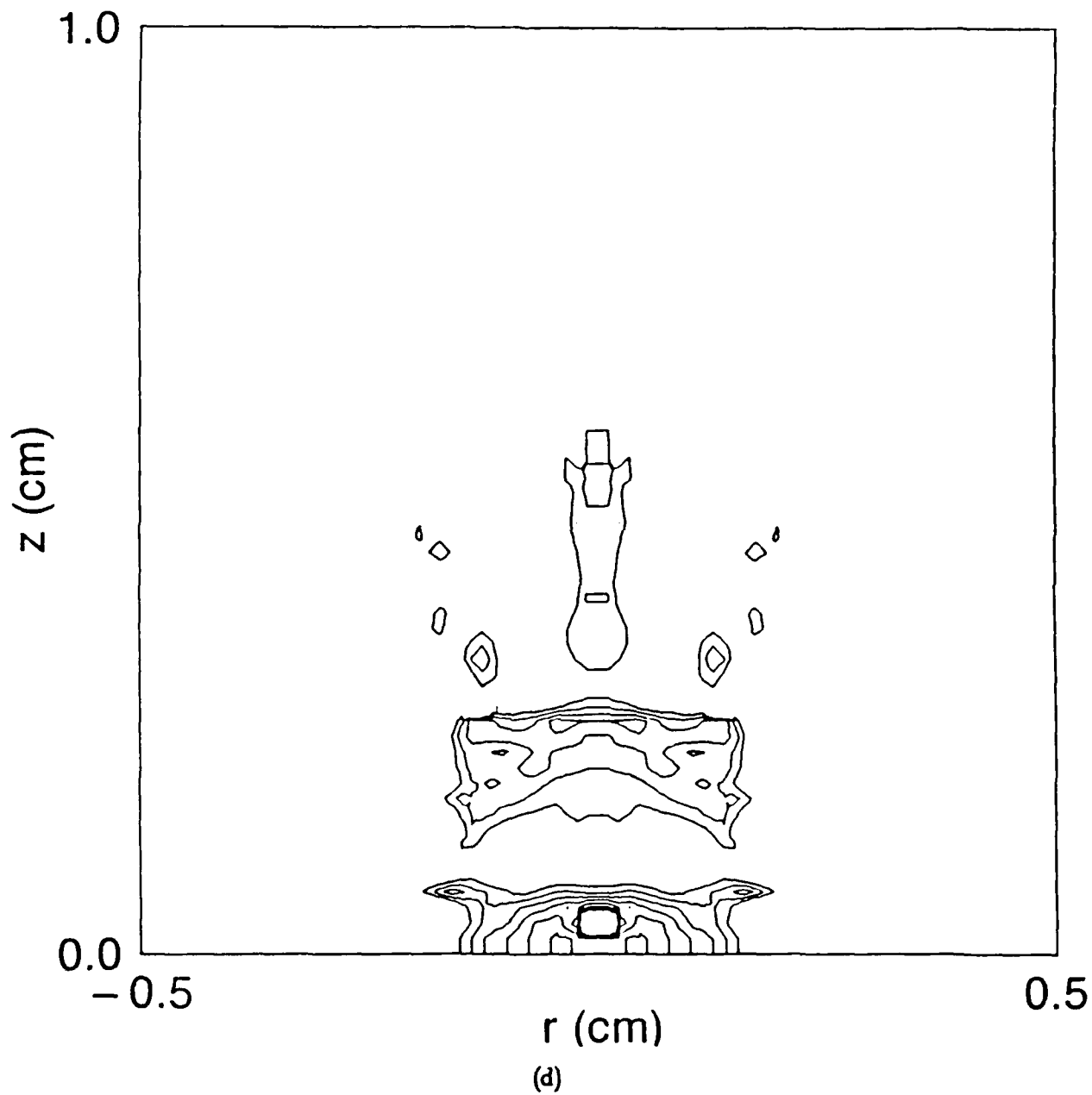
Fig. 6 — Total line radiation as a function of initial density.
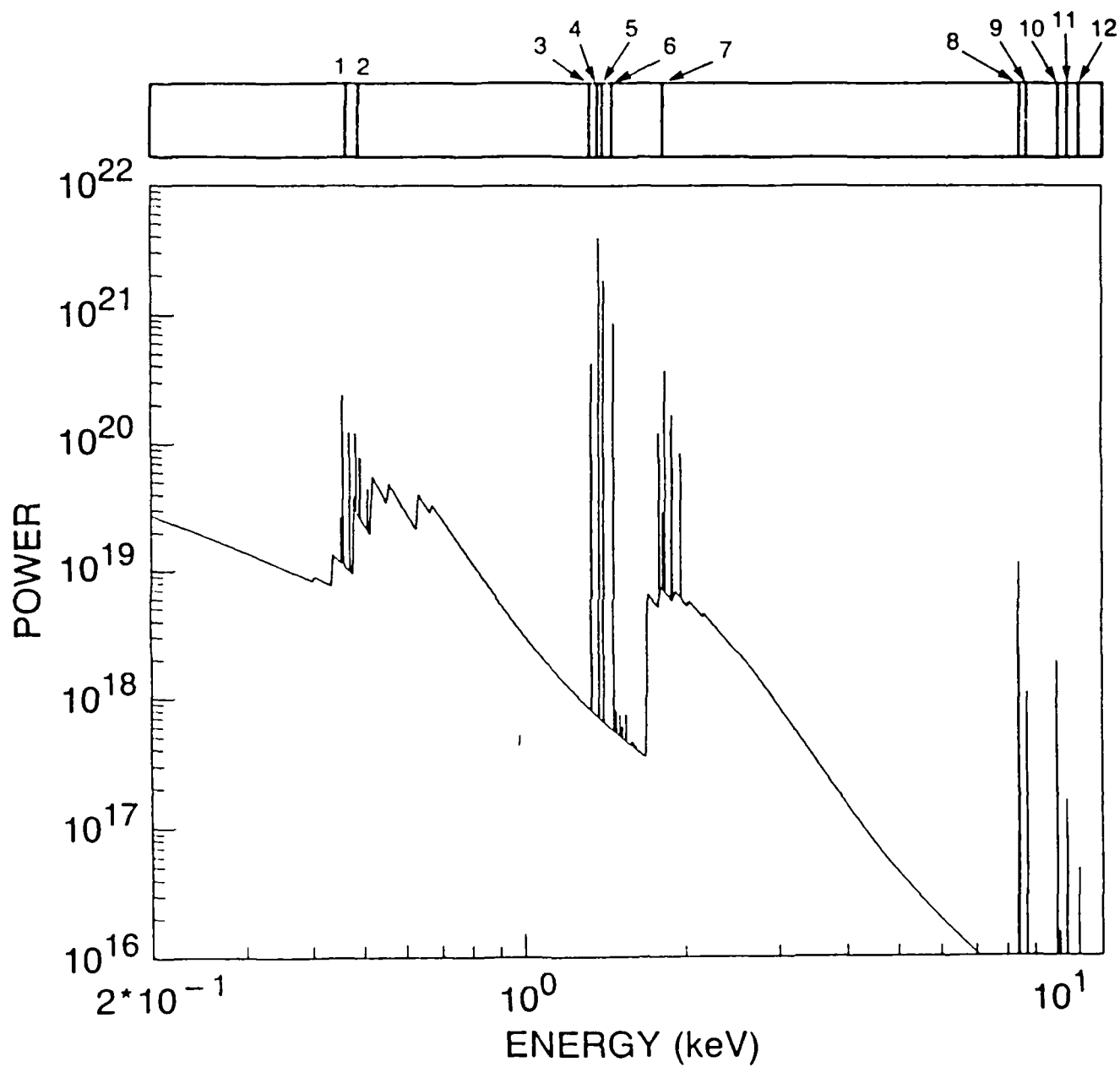
Fig. 7 — Instantaneous radiation power (ergs/sec-keV) spectrum as a function of photon energy at 18 nsec.
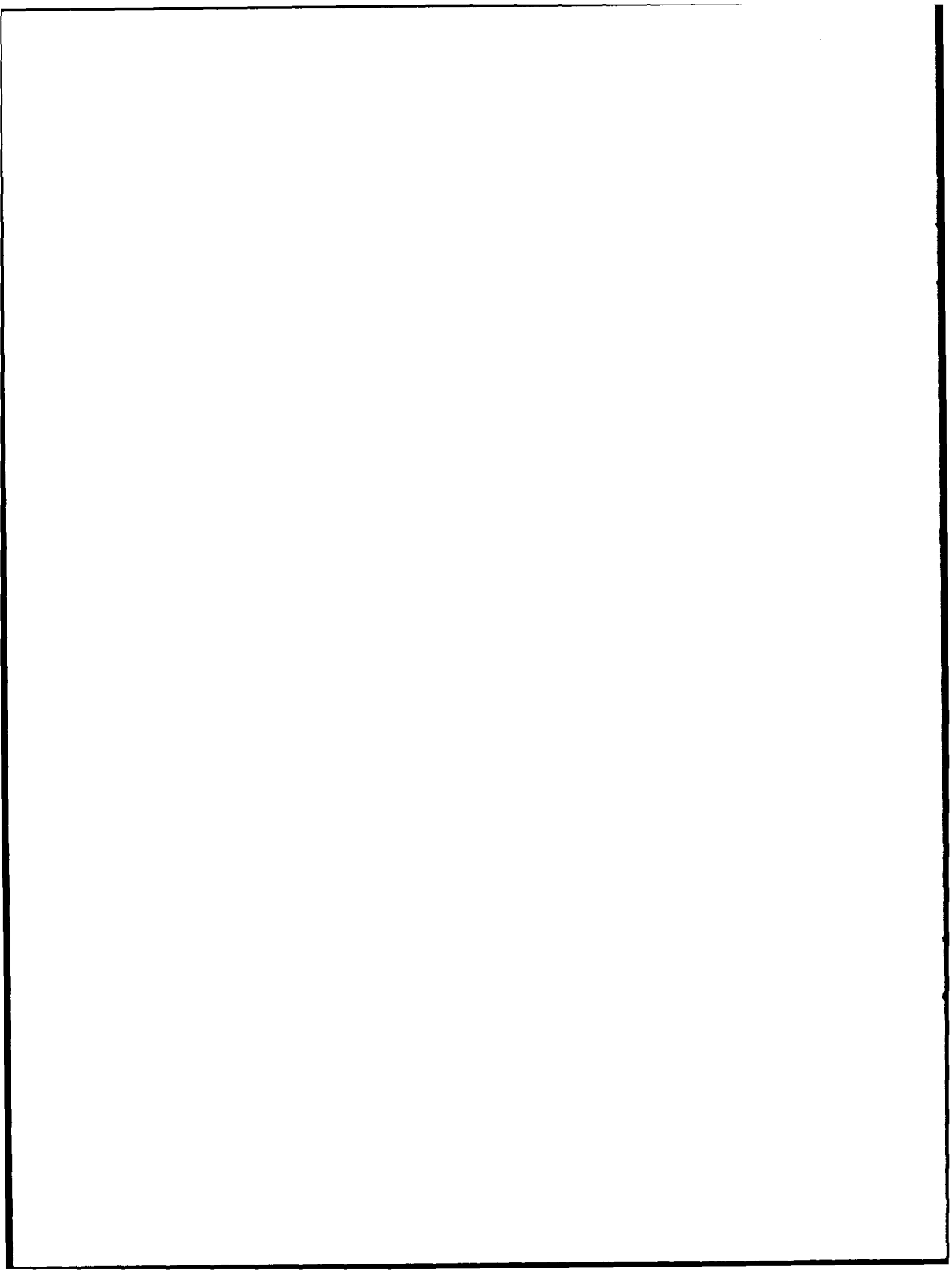
DISTRIBUTION LIST

Assistant to the Secretary of Defense   1 copy
Atomic Energy
Washington, D.C.   20301
Attn: Executive Assistant

Director
Defense Nuclear Agency
Washington, D.C.   20305
Attn: DDST   1 copy
       TITL   4 copies
       RAEV   1 copy
       STVI   1 copy

Commander   1 copy
Field Command
Defense Nuclear Agency
Kirtland AFB, New Mexico   87115
Attn: FCPR

Director   1 copy
Joint Strat TGT Planning Staff
Offutt AFB
Omaha, Nebraska   68113
Attn: JLKS

Undersecretary of Defense   1 copy
for RSCH and ENGRG
Department of Defense
Washington, D.C.   20301
Attn: Strategic and Space Systems (OS)

Deputy Chief of Staff for RSCH DEV and ACQ   1 copy
Department of the Army
Washington, D.C.   20301
Attn: DAMA-CSS-N

Commander   1 copy each
Harry Diamond Laboratories
Department of the Army
2800 Powder Mill Road
Adelphi, Maryland   20783
Attn: DELHD-N-NP
       DELHD-TA-L (Tech. Lib.)

U.S. Army Missile Command   3 copies
Redstone Scientific Information Center
Attn: DRSMI-RPRD(Documents)
Redstone Arsenal, Alabama   35809

Commander   1 copy
U.S. Army Nuclear and Chemical Agency
7500 Backlick Road
Building 2073
Springfield, Virginia   22150
Attn: Library

```
Commander                                        1 copy
Naval Intelligence Support Center
4301 Suitland Road, Bldg. 5
Washington, D.C.   20390
Attn:  NISC-45

Commander                                        1 copy
Naval Weapons Center
China Lake, California  93555
Attn:  Code 233 (Tech. Lib.)

Officer in Charge                                1 copy each
White Oak Laboratory
Naval Surface Weapons Center
Silver Spring, Maryland  20910
Attn:  Code R40
       Code F31

Weapons Laboratory                               1 copy each
Kirtland AFB, New Mexico   87117-6008
Attn:  Dr. William Baker
       SUL
       CA

Deputy Chief of Staff                            1 copy
Research, Development and Accounting
Department of the Air Force
Washington, D.C.   20330
Attn:   AFRDQSM

Commander                                        1 copy
U.S. Army Test and Evaluation Command
Aberdeen Proving Ground, Maryland   21005
Attn:  DRSTE-EL

Auburn University                                1 copy
Department of Physics
Attn: Dr. J. Perez
Auburn, Al    36849

BDM Corporation                                  1 copy
7915 Jones Branch Drive
McLean, Virginia  22101
Attn:  Corporate Library

Berkeley Research Associates                     1 copy
Post Office Box 983
Berkeley, California  94701
Attn:  Dr. Joseph Workman
```

Berkeley Research Associates   1 copy each
Post Office Box 852
5532 Hempstead Way
Springfield, Virginia   22151
Attn: Dr. Joseph Orens

Boeing Company   1 Copy
Post Office Box 3707
Seattle, Washington 98134
Attn: Aerospace Library

General Electric Company - Tempo   1 Copy
Center for Advanced Studies
816 State Street
Post Office Drawer QQ
Santa Barbara, California 93102
Attn: DASIAC

Institute for Defense Analyses   1 copy
1801 N. Beauregard Street
Alexandria, Virginia   22311
Attn: Classified Library

IRT Corporation   1 copy
Post Office Box 81087
San Diego, California   92138
Attn: R. Mertz

JAYCOR   1 copy
1608 Spring Hill Road
Vienna, Virginia   22180
Attn: R. Sullivan

JAYCOR   1 copy
11011 Forreyane Road
Post Office Box 85154
San Diego, California   92138
Attn: E. Wenaas
        F. Felbar

KAMAN Sciences Corporation   1 copy each
Post Office Box 7463
Colorado Springs, Colorado   80933
Attn: Library

Lawrence Livermore National Laboratory   1 copy each
University of California
Post Office Box 808
Livermore, California 94550
Attn: DOC CDN for 94550
       DOC DCN for L-47 L. Wouters
       DOC CDN for Tech. Infor. Dept. Lib.

Lockheed Missiles and Space Company, Inc.   1 copy each
Post Office Box 504
Sunnyvale, California   94086
Attn: S. Taimlty
        J.D. Weisner

Maxwell Laboratory, Inc.   1 copy ea.
9244 Balboa Avenue
San Diego, California   92123
Attn: A. Kolb
        M. Montgomery
        K. Ware

McDonnell Douglas Corporation   1 copy
5301 Bolsa Avenue
Huntington Beach, California   92647
Attn: S. Schneider

Mission Research Corporation   1 copy each
Post Office Drawer 719
Santa Barbara, California   93102
Attn: C. Longmire

Mission Research Corporation-San Diego   1 copy
5434 Ruffin Road
San Diego, California   92123
Attn: Victor J. Van Lint

Northrop Corporation   1 copy
Northrop Research & Technology Center
1 Research Park
Palos Verdes Peninsula, California   90274

Physics International Company   1 copy each
2700 Merced Street
San Leandro, California   94577
Attn: C. Deeney
        T. Nash

R and D Associates   1 copy each
Post Office Box 9695
Marina Del Rey, California   90291
Attn: Library

Science Applications, Inc.   1 copy
10260 Campus Point Drive
Mail Stop 47
San Diego, California   92121
Attn: R. Beyster

Science Research Laboratory
150 Ballena Blvd., Suite 100
Alameda, California 94501
Attn: M. Krishnan

Spectra Technol, Inc.,   1 copy
2755 Northup Way
Bellevue, Washington 98004
Attn: Alan Hoffman

Spire Corporation   1 copy
Post Office Box D
Bedford, Massachusetts 07130
Attn: R. Little

Director   1 copy
Strategic Defense Initiative Organization
Pentagon 20301-7100
Attn: T/IS Dr. Dwight Duston

Texas Tech University   1 copy
Post Office Box 5404
North College Station
Lubbock, Texas 79417
Attn: T. Simpson

TRW Defense and Space Systems Group   1 copy
One Space Park
Redondo Beach, California 90278
Attn: Technical Information Center

Naval Research Laboratory
Radiation Hydrodynamics Branch
Washington, D.C. 20375
Code 4720 - 50 copies
      4700 - 26 copies
      2628 - 22 copies

Naval Research Laboratory
Washington, DC 20375-5000
         Code 1220   Director of Research
                                                U.S. Naval Academy
Do NOT make labels for   Annaplis, MD 21402
Records-----(01 cy)   (2 copies) 1-0

Naval Research Laboratory
Washington, DC 20375-5000
         Code 2630
Timothy Calderwood